Antal Kerpely Doctoral School of Materials Science and Technology

Molecular Design and Electrospinnability of Biopolymer Nanofibers: Mechanisms and Modeling Insights

PhD dissertation

By

Nesreen Alkanakri

Supervisor

Dr. Michael C. Owen

Senior Researcher and Group Leader

Head of the Doctoral School

Prof. Dr. Valéria Mertinger

Institute of Chemistry

Faculty of Materials and Chemical Engineering

University of Miskolc, Hungary

Miskolc, 2026

Antal Kerpely Doctoral School
Graduate School Committee

July 18th, 2026

To Whom It May Concern;

This is to acknowledge that **Ms. Nesreen Alkanakri, M.Sc.** (Syria, Passport No: N 015343789) has been enrolled in the Antal Kerpely Doctoral School at the University of Miskolc (Hungary) since September of 2022 under my supervision. Nesreen has successfully completed her first eight semesters at the Faculty of Materials Science and Engineering.

Nesreen has shown consistent academic progress throughout the program. She has recently published two articles in the *ACS Journal of Physical Chemistry B* as first author, and has another article under review. Moreover, she has given several talks at international scientific symposia. Nesreen has also received her *absolutorium*, certifying the completion of the requirements of the PhD program.

Her work in the development of molecular dynamics protocols for the evaluation of fibers synthesized using electrospinning is both novel and challenging, and I strongly contend that her progress in this area should earn her consideration for a PhD degree.

I therefore fully endorse Nesreen's continuation in the PhD defense procedures.

Thank you for your time and consideration.

Sincerely,

Michael C. Owen, PhD.
Senior Researcher and Group Leader
Institute of Higher Education and Industrial Cooperation
University of Miskolc

ACKNOWLEDGMENT

"And that there is not for man except that for which he strives, and that his effort will be seen. Then he will be recompensed for it with the fullest recompense."

(Qur'an, Surah An-Najm, 53:39-41)

First and foremost, I want to sincerely thank Almighty God, whose endless blessings, guidance, and mercy have made it possible to complete this thesis. All praise and gratitude are due to Him, for with His grace, this journey began, and by His will, it has come to an end.

I would like to express my sincere gratitude to my supervisor, **Dr. Michael C. Owen**, who taught me far more than academic knowledge. His continuous guidance, support, and encouragement helped me grow both professionally and personally. I will always remember his words that the reward is not received in the middle of the journey, but at its end.

I would like to express my sincere thanks to **Dr. Kolos Molnár**, who supported me from the very beginning and believed in my abilities. I am deeply grateful for his support, and I sincerely hope to have the opportunity to continue working with him in the future.

I sincerely thank **Dr. Maria Fyta** for her support and for hosting me for a month through the Erasmus program. Her hospitality, guidance, and academic assistance were greatly appreciated and positively impacted my research experience.

I sincerely thank **Dr. Zsolt Fejes** for his help during my experimental work, **Dr. Babak Minofar** for his kind support, and my reviewer, **Dr. Béla Fiser**, for the valuable comments and constructive advice. I would also like to extend my sincere thanks to all the doctors in the department.

I want to sincerely thank my parents, whose unconditional love, constant support, and endless sacrifices have laid the foundation for my journey. Their encouragement and belief in me have been my greatest sources of strength throughout this work.

I am sincerely thankful to my siblings, Reham, Amena, Shaimaa, Yara, and Ahmad, whose presence and support have meant more to me than words can express.

I also want to sincerely thank my friends Dr. Hadeer, Buthaina, Imene, Bushra, and Julie, whom I met while studying abroad. They were more than just friends; they became a second family, offering support, understanding, and warmth during both difficult and happy times.

I would also like to extend my sincere thanks to my longtime friends Dr. Ghandi, Alaa, and Nour, who have always been there for me, offering support despite the distance.

Finally, to my persistent companion, Multiple Sclerosis, thank you for every obstacle that became a lesson, every setback that revealed new strength, and every difficult day that made this achievement even more meaningful. You were never the story I would have chosen, but you became part of the story that brought me here.

The research reported here was carried out as part of the EFOP-3.6.1-16-2016-00011 “Younger and Renewing University – Innovative Knowledge City – Institutional development of the University of Miskolc aiming at intelligent specialization” project implemented in the framework of the Szechenyi 2020 program. The research reported was supported by the National Research, Development and Innovation Office (FK 138501). The realization of this project is supported by the European Union and co-financed by the European Social Fund. The authors gratefully acknowledge the use of the Komondor supercomputer at the Governmental Agency for IT Development (KIFÜ) in Debrecen, Hungary, which provided the high-performance computing resources necessary to carry out the molecular dynamics simulations in this project study.

Declaration

During the preparation of the thesis, I did not use the services of artificial intelligence, except for grammatical and stylistic corrections.

Nesreen Alkanakri

Contents

List of Figures

List of Tables

Chapter 1: Introduction

1.1 Summary

Nanotechnology has become one of the most dynamic and influential fields in modern science, combining principles from physics, chemistry, biology, and engineering to develop materials with innovative properties. Among these, nanofibers are a unique type of one-dimensional nanomaterial known for their large surface area, porosity, and flexibility. Their remarkable properties have led to numerous applications, especially in biomedicine, energy, and environmental engineering. Electrospinning, considered the most versatile and efficient method for producing continuous nanofibers, enables precise control over fiber structure and shape. This chapter covers fundamental concepts, classifications, and fabrication techniques of nanofibers, with a focus on electrospinning and its key parameters. It also emphasizes their role in biomedicine, particularly with natural polymers such as collagen and chitosan, which, despite their high biocompatibility, pose significant challenges during electrospinning due to their complex molecular structures and solubility issues. The chapter concludes by outlining the main research objectives.

1.2 Definition and Concept of Nanofibers

Nanotechnology is one of the most transformative scientific and technological fields of the 21st century. It combines materials science, physics, chemistry, biology, and engineering. Nanomaterials, which are the core of nanotechnology, exhibit unique physical, chemical, and biological properties and offer great promise for various applications in energy, the environment, electronics, and medicine [1].

Within this broad category of materials, nanofibers stand out as a unique and highly versatile group. Nanofibers are one-dimensional (1D) nanoengineered fibers, typically made from natural or synthetic polymers, with diameters usually less than 1 micron and lengths that can extend well beyond their width [2]. Their distinctive shape provides a high surface area to volume ratio, porosity, and mechanical flexibility [3]. These features give nanofibers significant potential across many fields, including water and air filtration, energy storage (such as batteries and fuel cells), gas sensing, photocatalysis [4], and biomedical applications like tissue engineering, wound healing, and drug delivery [5].

Structurally, nanofibers differ from other nanomaterials because of their continuous, elongated shape. While nanoparticles are zero-dimensional and roughly spherical, and

nanorods are short, solid, rod-like structures, nanofibers have long, continuous one-dimensional forms that can be aligned or layered into complex mats and scaffolds [6]. This unique arrangement not only provides specific mechanical properties but also enables the formation of fibrous networks that closely mimic natural extracellular matrices, which is especially important in biomedical applications [7].

1.2.1 Classification of Nanofibers

Nanofibers can be classified according to their raw material composition and structural configuration.

1.2.1.1 By Material Composition

According to their material composition, nanofibers are commonly categorized into three main groups:

Natural polymers: The focus on nanofibers from natural polymers has recently increased. Some of these polymers include silk, collagen, gelatin, chitosan, and chitin [8].

Synthetic polymers: A wide range of synthetic polymers are frequently used to produce nanofibers, including poly(L-lactide) (PLLA), poly(glycolic acid) (PGA), and polycaprolactone (PCL) [9].

Copolymers/hybrids: To address certain limitations of synthetic and natural biopolymers, researchers have developed copolymers and hybrid blends to produce nanofibers. By combining their unique and beneficial properties, examples include collagen/PCL [10] and gelatin/PCL [11].

1.2.1.2 By Internal Structure or Configuration

Based on their internal structure or configuration, nanofibers are commonly categorized into three main groups:

Core-shell nanofibers: Core–shell nanofibers are coaxial structures where one material forms the core and another forms the outer shell. This design enables the encapsulation of functional molecules, drugs, or nanoparticles within a protective outer layer, allowing for controlled release [12].

Porous nanofibers: possess interconnected micro or nanopores, significantly increasing their surface area and permeability. This could enable a wide range of applications in tissue engineering, sensing, filtration, separation, and catalysis [13].

Aligned nanofibers: Uniaxially oriented nanofibers demonstrate considerably enhanced mechanical properties compared to traditional fibers, indicating potential applications in catalysis, biomedicine, microelectronics, and optics [14].

Gradient nanofibers: These nanofibers are designed to exhibit hierarchical, gradually varying structures across their cross-section or along their length [15]. This graded architecture provides improved fracture toughness and enhanced mechanical performance, making it ideal for load-bearing biomedical applications such as musculoskeletal tissue scaffolds (tendons and ligaments), skin regeneration matrices, and wound dressings, where materials must balance elasticity and strength [16].

1.2.2 Nanofiber Fabrication

Nanofibers can be produced using various fabrication methods, each offering specific advantages in fiber structure, shape, and potential applications. The most common methods include template synthesis, phase separation, self-assembly, and electrospinning.

Template synthesis: A technique that uses pre-made templates to guide the formation of nanostructured materials, enabling the creation of unique structures and shapes. It includes various methods, such as physical and chemical templating, to achieve specific nanofiber properties [17].

Phase separation: Phase separation involves creating two separate phases within a uniform polymer–solvent mixture. A standard method is thermal-induced phase separation (TIPS). When the polymer solution cools, two phases form: a polymer-rich phase and a polymer-lean phase. Over time, gelation occurs, forming a network structure in the polymer-rich phase as the solvent is removed through extraction or evaporation [18].

Self-assembly: Self-assembly is a complex process in which individual molecules or macromolecules spontaneously organize into ordered nanostructures through noncovalent interactions such as hydrogen bonding, hydrophobic interactions, and electrostatic forces. Polymeric nanofibers can form via polymer chain annealing, crosslinking, dissolution, and selective cleaving, allowing precise control over molecular arrangement and functionality [19].

Electrospinning: Electrospinning is one of the most versatile, simple, and effective technologies available. It is also the only method suitable for producing continuous nanofibers on an industrial scale. During electrospinning, a high-voltage electric field is applied to a

polymer solution or melt, producing an electrically charged jet. As the jet is stretched and the solvent evaporates, ultrafine fibers are deposited onto a collector [20].

1.2.3 Applications of Nanofibers

The unique structural and functional features of nanofibers allow their use in a wide range of scientific and industrial fields. Major applications include biomedicine, environmental engineering, energy and electronics, catalysis, and coatings.

Biomedical applications: Nanofibers are widely used in biomedical engineering due to their close resemblance to the natural extracellular matrix (ECM) and their ability to promote cell adhesion, growth, and differentiation. They are vital components of advanced wound dressings, maintaining a moist healing environment and enabling controlled release of therapeutic agents. Nanofibrous drug delivery systems can encapsulate bioactive molecules for sustained or stimuli-responsive release. In tissue engineering, electrospun nanofibers act as scaffolds for regenerating skin, cartilage, bone, and nerve tissue, offering mechanical support and bioactive surfaces that direct cell growth [5].

Environmental applications: The high porosity and large specific surface area of nanofiber mats make them excellent for filtration and separation processes. They are used in water and air filtration, including the removal of fine particulates, heavy metals, and microorganisms. Nanofibers also play a key role in oil–water separation and oil spill cleanup, as well as in membranes for pollutant capture, helping advance sustainable environmental management [21].

Energy and electronics: Nanofibers are vital in the energy and electronics industries. Their interconnected networks and high electrolyte permeability make them perfect for use as battery separators, supercapacitor electrodes, and proton-conducting membranes for fuel cells. Nanofibers are sensors and energy-harvesting components in flexible and wearable electronics, allowing their integration into smart textiles, self-powered sensors, and wireless communication devices [22].

Catalysis and coatings: Nanofibers are efficient catalyst supports and nanoreactors that enhance reaction rates and selectivity in chemical and electrochemical processes. They are also used as protective and functional coatings, including self-cleaning and anti-fouling surfaces, where their roughness and chemical tunability offer water-repellent or antimicrobial properties [23].

1.2.4 Challenges and Future Outlooks

Despite their remarkable potential, nanofiber technologies face significant limitations that restrict their large-scale use. Major technical challenges include production scalability, where maintaining high throughput while ensuring uniform fiber structure remains difficult. Consistently achieving uniform fiber diameter and structural consistency across industrial batches is a persistent problem, as small changes in processing can lead to performance variations. Additionally, material choices are often constrained by the spinnability of polymers and their compatibility with solvents or processing conditions [4]. In addition to fabrication issues, biological and environmental safety also pose major challenges. Some nanofiber materials, solvents, or additives may be toxic to cells or cause unintended biological effects, raising concerns about long-term compatibility with living organisms. Environmental risks can also arise from the release of waste solvents and micro- and nanoplastics into ecosystems. These issues underscore the need for greener manufacturing techniques and the use of biodegradable or naturally sourced polymers to lessen ecological impact [24].

The future of nanofiber technology is heading toward smart, multifunctional, and sustainable materials that fulfill both technological and societal needs. A key focus is on developing stimuli-responsive (smart) nanofibers that can react to pH, temperature, electrical, or biochemical cues, enabling on-demand drug release, adaptive tissue scaffolds, and responsive sensors [25]. Multi-material and hybrid nanofibers, which combine natural and synthetic components or incorporate nanoparticles, are anticipated to provide tailored mechanical, electrical, and biological properties for advanced biomedical, environmental, and energy applications [26].

Emerging fabrication strategies, such as three-dimensional (3D) printing, will enable the creation of hierarchically organized, complex scaffolds that more closely resemble native tissues [27]. Simultaneously, green and sustainable manufacturing approaches, including using biodegradable and biocompatible polymers, align with global sustainable development goals, reducing environmental impact and enhancing clinical safety [28].

1.3 Electrospinning

1.3.1 Process

Electrospinning uses a strong electric field to create nanofibers from polymer solutions. The minimal setup includes a pump connected to a syringe filled with the polymer solution [29], as shown in ***Figure 1***. This solution is subjected to a high-voltage electric field between the syringe needle (the spinneret) and a grounded collector plate on which the

nanofibers form [30]. The polymer solution is first pumped through the capillary needle, where the solution's surface tension causes droplets to form at the spinneret, with an induced charge on the droplet surface. When the electrostatic force equals the surface tension of the solution, the droplet changes from a hemispherical shape to a cone shape. When the electrostatic force exceeds the surface tension, the solution can overcome it and form jets. While reaching the collection device, the electrostatic force stretches the jets and causes the solvent to evaporate, leaving only solid fibers [31]. The formation of a liquid polymer jet in electrospinning relies on a delicate balance between electrical force and surface tension of the solution [32]. While this balance typically results in nanofiber production, other outcomes, like droplet spraying, can occur [33].

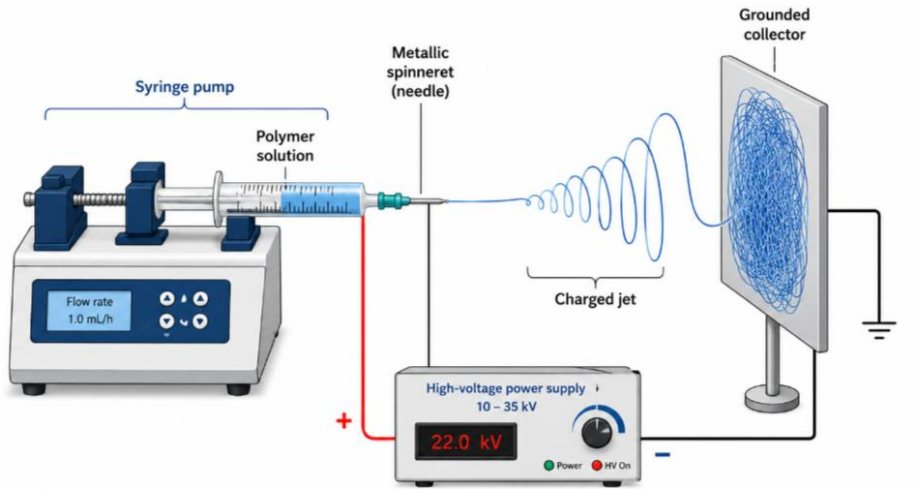

Figure 1. Schematic illustration of the electrospinning setup showing the main components: syringe pump, polymer-solution syringe, metallic spinneret (needle), high-voltage power supply (10 to 35 kV), and grounded collector.

Different types of nanofibers made from polymers and blends have been successfully created through electrospinning, with diameters ranging from a few nanometers to hundreds of microns [34]. Additionally, if the same polymer is dissolved in different solvents, the morphology of the resulting nanofibers will differ [35].

1.3.2 Parameters

In addition to the advantages of a simple process and a wide range of raw materials, electrospinning can control the morphology, orientation, and pore size of nanofibers by adjusting parameters [36]. Many parameters influence electrospinning and can be categorized into solution, processing, and ambient parameters [37]. Solution parameters include concentration, viscosity, molecular weight, conductivity, surface tension, and solvent type. Processing parameters encompass applied voltage, flow rate, and needle-to-collector distance. Ambient parameters involve temperature and humidity.

1.3.2.1 Solution Parameters

The properties of the polymer solution play a crucial role in determining the characteristics of the resulting nanofibers. The main solution parameters are discussed below:

Concentration: The solution concentration is critical for forming nanofibers. There is a minimum spinnability concentration. When the solution concentration drops below this level, the low concentration and high surface tension cause the interaction between the electric field force and surface tension to separate the polymer before it reaches the collection device. This results in many beads instead of fibers [38]. As the concentration increases, the polymer's entanglement concentration rises while surface tension decreases, leading to more fiber formation. Ultimately, this process produces uniform and smooth nanofibers without beads [39]. As shown in ***Figure 2***, the nanofibers become coarser with increasing concentration [40].

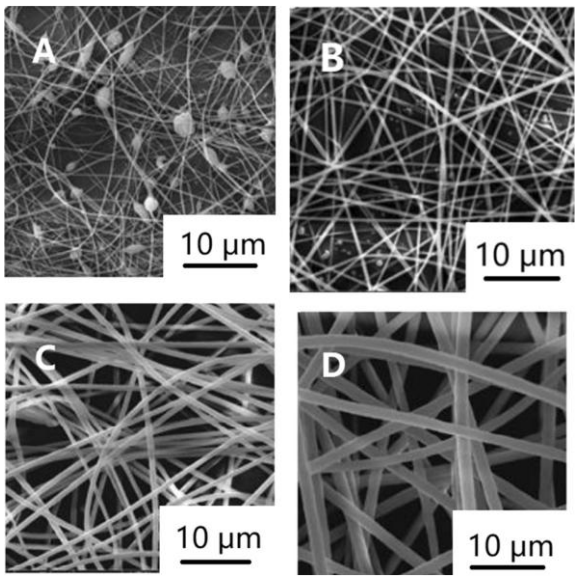

Figure 2. Scanning Electron Microscope (SEM) images of electrospun polyimide nanofibers showing improved fiber quality and increased fiber diameter as solution concentration increases: (A) 10%, (B) 15%, (C) 20%, and (D) 25%. All scale bars represent 10 µm (Kohse et *al*., Current Directions in Biomedical Engineering, 2017).

Viscosity: The viscosity of the solution is closely related to concentration and molecular weight, which are key factors affecting the diameter and shape of nanofibers [41]. When viscosity is too low, it indicates low polymer entanglement and dominant surface tension, which prevent droplets from merging into fibers and forming a spray [42]. As viscosity increases, the polymer's stress-relaxation time increases, supporting the formation of nanofibers with larger, more uniform diameters. However, if viscosity becomes too high, it becomes difficult for jets to form fibers [43].

Molecular weight: Similar to the effects of viscosity and concentration, polymers with low molecular weight lack sufficient entanglement, have short chain lengths, low molecular

friction, and are difficult to resist unstable whipping, leading to interrupted jets and challenges in fiber formation [44]. Typically, nanofiber diameter also increases with molecular weight.

Conductivity: Charged particles in the polymer greatly influence jet formation. When the solution's conductivity is too low, beads form, hindering the production of uniform nanofibers. Conversely, high conductivity can lead to uneven diameters [45].

Surface tension: Surface tension is affected by many factors, including molecular weight, solution concentration, solvent type, and temperature. When surface tension is low, there are fewer beads, and the nanofibers become finer and smoother. Some researchers think that surface tension has little impact on fiber diameter [46]. However, if surface tension is too low, the jet becomes unstable, which can cause an uneven distribution of nanofiber diameters or even lead to bead formation [47].

Solvent: There is no doubt that selecting the right solvent is crucial. The properties of the solvent, including surface tension, dielectric constant, boiling point, density, and interactions between the solvent and solute, will influence electrospinning, as shown in ***Figure 3*** [40]. Due to the toxicity of many organic solvents, if they cannot be completely removed, they are not suitable for use in biological and food applications [48]. The effect of different solvents on electrospinning is complex, and there is no clear theory that determines whether electrospinning can be successfully performed with a specific solvent [49].

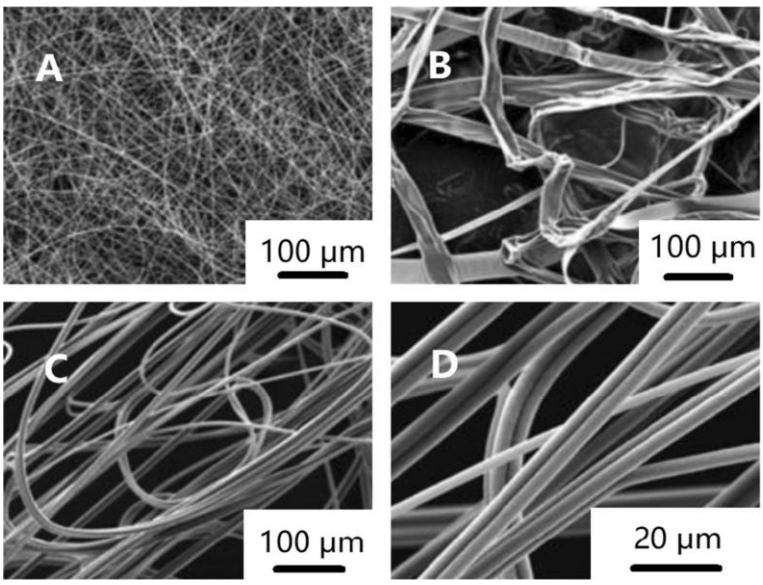

Figure 3. Scanning Electron Microscope (SEM) images of electrospun polyimide nanofibers showing the effect of different solvents on fiber morphology: A) *N*, *N*-dimethylformamide (DMF), B) 1,1,1,3,3,3-hexafluoro-2-propanol (HFIP), c) and D) dimethyl sulfoxide (DMSO) (Kohse et *al*., Current Directions in Biomedical Engineering, 2017)

1.3.2.2 Processing Parameters

The key processing parameters are outlined below:

Applied voltage: A crucial factor in electrospinning. Only when the voltage exceeds the critical point can the droplet be ejected and reach the collection device. The voltage also influences nanofiber morphology and diameter. If the applied voltage is too high or too low, it can cause bead formation [50]. The diameter of nanofibers decreases with increasing applied voltage because the stronger electrostatic force stretches the droplets more.

Flow rate: It also affects the diameter and shape of nanofibers. The nanofiber diameter typically increases with increasing flow rate. If the flow rate becomes too high, the solvent may not fully evaporate before reaching the collection device, leading to bead formation [51]. Therefore, the solution remains more stable at moderate flow rates, facilitating the production of smooth, uniform nanofibers.

Needle-to-collector distance: The distance from the needle to the collector must be sufficiently large to allow the solvent to evaporate. If the distance is too small, beads will form [52]. However, the distance should not be too large. If it is too large, the jet may become unstable, leading to bead formation.

1.3.2.3 Ambient Parameters

Ambient parameters also play an important role in the electrospinning process. The main parameters are discussed below:

Temperature: Generally, as temperature rises, viscosity and surface tension decrease, while solubility increases. An increase in temperature causes the nanofibers' diameter to decrease and results in a smoother surface [53].

Humidity: The effect of environmental humidity on electrospinning is also complex. When humidity is low, the solvent evaporates more quickly, leading to larger nanofiber diameters. Conversely, at excessively high humidity, the nanofiber diameter distribution becomes more uneven, the surface rougher, and there are fewer pores or fibers [54].

1.3.3 Models and Simulation

Simulating electrospinning with computers is essential. Because many experimental results are difficult to explain, theoretical models and simulations help improve our understanding of various issues. Although electrospinning technology has attracted significant attention, few studies have focused on simulation. By establishing an accurate mathematical and physical model for electrospinning simulation, the morphology and properties of nanofibers can be well predicted, thereby enhancing researchers' efficiency and expanding the application of electrospinning technology.

1.3.3.1 Physical Models

The primary physical models include the following:

Models of Electric Field

Taylor [55] first studied the jet's initial stage. In principle, when the electric field force and surface tension are equal, the viscous droplet will form a cone with a half-vertex angle of 49.3 degrees. Interestingly, Yarin et *al*. [56] confirmed theoretically and experimentally that the half-angle of the Taylor cone should be 33.5 degrees instead of 49.3. This difference may be due to the existence of non-self-similar solutions for hyperboloid shapes in equilibrium with their own electric fields under the action of surface tension. The typical structure of the Taylor cone is illustrated in ***Figure 4*** [57].

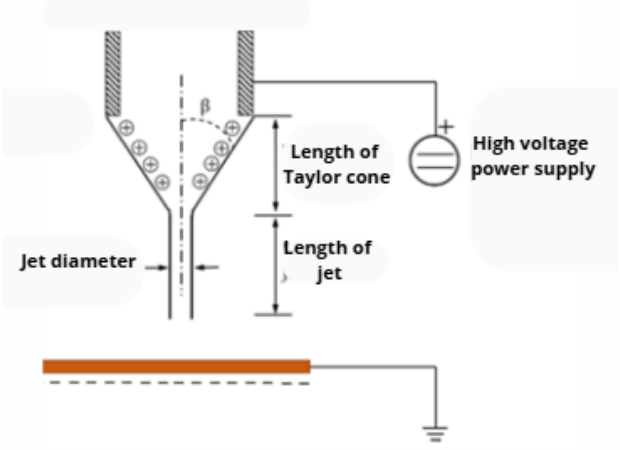

Figure 4. Schematic diagram of Taylor cone and jet formation during electrospinning, illustrating key geometric parameters including the cone with a half-vertex angle (β), the length of the Taylor cone, the length of the jet, and the jet diameter under a high-voltage power supply (Wang et *al*., Experimental Thermal and Fluid Science, 2021).

.

Models of Jet

When the applied voltage exceeds the critical voltage, and the electric force exceeds the surface tension, the jet first enters a stable stage, then an unstable stage.

Stable stage: In this stage, the polymer jet undergoes uniaxial stretching, and its shape remains constant over time. During this phase, the jet radius is a major focus of research because it directly affects nanofiber diameter.

Unstable Stage: The unstable stage is more complex than the stable stage, and researchers have invested significant effort in it. The instability results from charge repulsion within the jet. There are three types of instability during the unstable stage of electrospinning [58]: the classical Rayleigh mode (axisymmetric) instability, electric field-induced axisymmetric conducting mode (bending) instability, and whipping conducting mode instabilities. These

instabilities vary with the applied voltage, the distance from the jet device to the collector, and solution parameters, which influence nanofiber morphology and distribution [59].

1.3.3.2 Molecular Simulation

Molecular simulation technology includes the Monte Carlo and molecular dynamics methods [60]. The Monte Carlo method is based on statistics and is suitable for equilibrium systems. The molecular dynamics method is a deterministic approach based on classical mechanics, which can solve the equations of motion for all particles in the system.

In electrospinning, molecular dynamics is frequently used to study how composite materials interact and how nanofiber products interact with drugs or proteins. For example, Jirsa´k et *al*. [33] employed Monte Carlo and molecular dynamics methods to simulate the early stages of the jet, as shown in ***Figure 5***. The results from both methods are consistent with experimental findings and indicate that the balance between ion concentration and field strength affects bead formation in nanofibers.

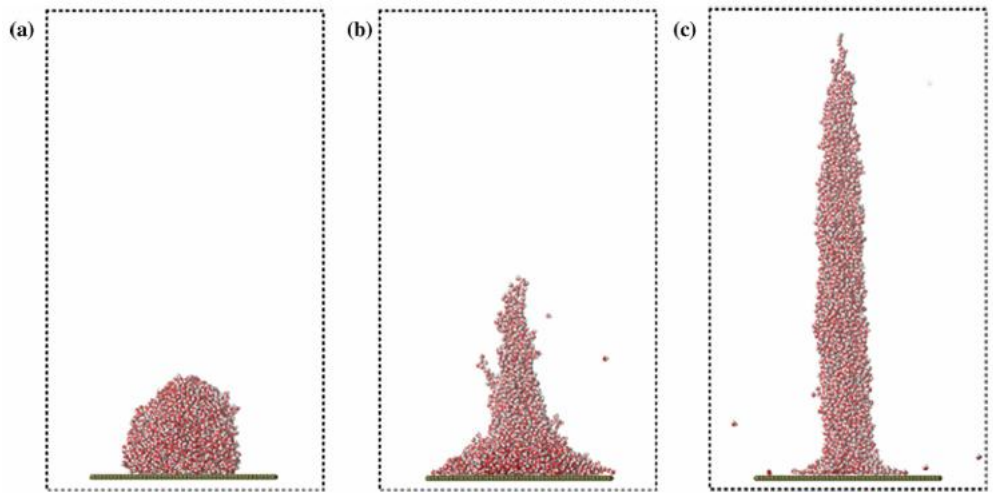

Figure 5. Displays a series of snapshots showing the transformation of a droplet on the wall, representing the apex of the Taylor cone, into a jet. a) The system before the field was applied, b) the moment shortly after the field was applied, and c) when the droplet has transformed into the jet. Colored spheres depict atoms and ions as follows: red–oxygen, white–hydrogen, blue–sodium cation, and cyan–chloride anion (Jirsák et *al*., Industrial & Engineering Chemistry Research, 2014).

Researchers, including Danwanichaku et *al*. [61], used Monte Carlo methods to simulate nanofiber deposition, revealing a positive correlation between concentration and pore size, and tested the filtration performance of polystyrene particles, which matched experimental results. Sarmadi et *al*. [62] used molecular dynamics methods to simulate the protein adsorption capacity of electrospun PCL/ polyvinyl alcohol (PVA) nanofibers, with results that aligned with experimental findings. Vao-soongnern [63] also analyzed how molecular weight and polymer chain conformation affect the structure and properties of electrospun nanofibers using Monte Carlo methods. Steffens et *al*. [64] employed quantum-

mechanical calculations and molecular dynamics simulations to investigate the interaction between PVA nanofibers and drug-loaded dacarbazine, providing insight into the principles of controlled drug release.

1.3.3.3 Neural Network

Neural networks have recently become a popular machine learning algorithm, but their application in electrospinning remains limited. Sarkar et *al*. [65] used a neural network algorithm, taking concentration, conductivity, flow rate, and electric field strength as input variables. It can effectively predict changes in fiber diameter but only considers four variables, making it less suitable for the complex electrospinning process.

1.3.4 Challenges and Future Outlooks

Electrospinning faces several critical challenges that hinder its broader industrial adoption and practical applications. The process is hindered by slow nanofiber production, low yield, and high operational costs, making scaling difficult. Additionally, reliance on toxic and flammable solvents, along with limited solvent choices, raises safety, hygiene, and environmental concerns. Other technical challenges include safety risks from high voltages, dependence on solution electrical properties, material compatibility issues, and the need for polymers with appropriate molecular weight and chain entanglement to produce continuous fibers. Moreover, clogging of the spinneret, especially when working with biopolymers, can halt production and reduce efficiency [66]. Also, determining the blending ratio between polymers has largely relied on trial and error, often yielding inconsistent results and high material consumption.

Future trends in electrospinning are increasingly focused on green, sustainable manufacturing, emphasizing environmentally friendly, toxin-free processes that use water-based or bio-derived solvents and energy-efficient methods to reduce environmental impact, especially for applications in biomedicine, filtration, pharmaceuticals, and cosmetics [67]. To address the low production rate of traditional electrospinning, advanced techniques such as needleless, multi-jet, and centrifugal electrospinning are gaining popularity, with some methods reaching outputs of up to 450 g/h, facilitating industrial-scale nanofiber production [68]. Another important trend is the integration of electrospinning with 3D printing and additive manufacturing, enabling the creation of complex, multifunctional materials for cutting-edge applications such as tissue engineering, smart sensors, and high-performance filtration systems. Simultaneously, research is increasingly focused on developing bio-based,

recyclable polymers and hybrid composites, expanding the material palette and promoting circular, eco-friendly production.

1.3.5 Materials Used in Electrospinning

Almost any soluble polymer with a sufficiently high molecular weight can be electrospun, including synthetic and natural polymers. Early electrospinning studies mainly focused on synthetic polymers such as polyethylene oxide (PEO), nylon, polyimide, polyaramid, and polyaniline [42]. However, it was quickly recognized that this technique could also produce nanofibers from some naturally occurring polymers. Chaparro et *al*. first attempted to create DNA fibers in the lab [69]. In less than ten years, hundreds of publications have emerged in this field, with various polymers successfully electrospun into nanofibers. With growing interest in biomedical applications, many biopolymers, such as collagen, silk fibroin, chitosan, cellulose, and fibrinogen, are being electrospun into nanofibers. Compared with synthetic polymers such as poly(lactic acid) (PLA), PGA, and PVA, naturally occurring polymers often offer better biocompatibility but poorer processability. Many functional biopolymers are unsuitable for direct electrospinning due to their low molecular weight or limited solubility. A common effective strategy to address this challenge is to blend them with polymers that are more compatible with electrospinning [70].

In the following section, the natural polymers collagen and chitosan are discussed in detail.

1.4 Collagen

Collagen is an essential extracellular matrix protein that provides structural and mechanical support to tissues like tendons, skin, and cartilage. It is the most abundant protein in humans and other mammals, making up more than 30% of total protein [71]. Collagen plays a key role in cell adhesion, cell migration, and tissue repair. A systematic understanding of collagen's structure can enhance our knowledge of its biological functions and provide theoretical guidance for its use as a natural protein material.

1.4.1 Structure of Collagen

Collagen is a highly organized coiled aggregate of singular tropocollagen strands, each of which is a triple helix comprised of three individual polypeptide chains [72]. These chains form an extended polyproline II-like helix coiled around a common axis [73]. Each polyproline II triple helix consists of repeated sequences of three amino acids (Gly-Xxx-Yyy), with proline (Pro) and 4-hydroxyproline (Hyp) commonly found in the Xxx and Yyy

positions [74]. This sequence is widely observed in collagen and has been extensively examined due to its remarkable stability, structure, and dynamics.

In the triple helix, every third amino acid residue is positioned around the central axis, where the space along the α chains is narrowest. Therefore, glycine residues are ideal for the third position because of their small volume. The stability of the conformation and the achievement of biomechanical and physiological functions mainly depend on secondary interactions, such as hydrogen bonds between the N–H group of glycine residues and nearby carbonyl (C=O) groups. Proline and lysine can form hydroxyproline and hydroxylysine through hydroxylation by hydroxylase in the collagen α-polypeptide chain. These amino acids contribute to collagen stability through hydrogen bonding and van der Waals interactions between polypeptide chains. Hydroxyproline is found only in collagen, and its content exceeds that of other amino acids by more than 50%, providing binding sites for water molecules and playing a critical role in hydrogen bond formation and the stability of the triple-helical structure [75]. ***Figure 6*** shows the Chemical structures of glycine, proline, and hydroxyproline.

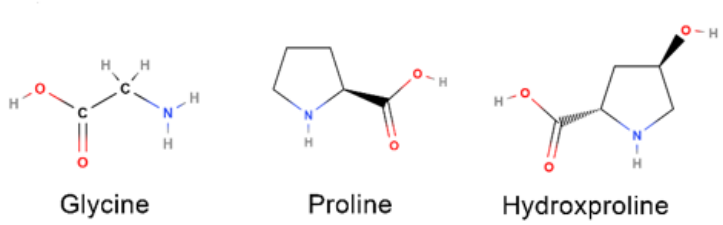

Figure 6. Chemical structures of glycine, proline, and hydroxyproline.

Tropocollagens are aligned end-to-end in a line and arranged parallel to each other to form stable microfibrils. These microfibrils then assemble into collagen fibrils with a crystallographic structure, which aggregate and organize into bundles to form collagen fibers [76]. Ultimately, collagen fiber bundles interpenetrate and intertwine to form the organism's basic structural framework, a three-dimensional network. ***Figure 7*** illustrates the hierarchical levels of the collagen structure.

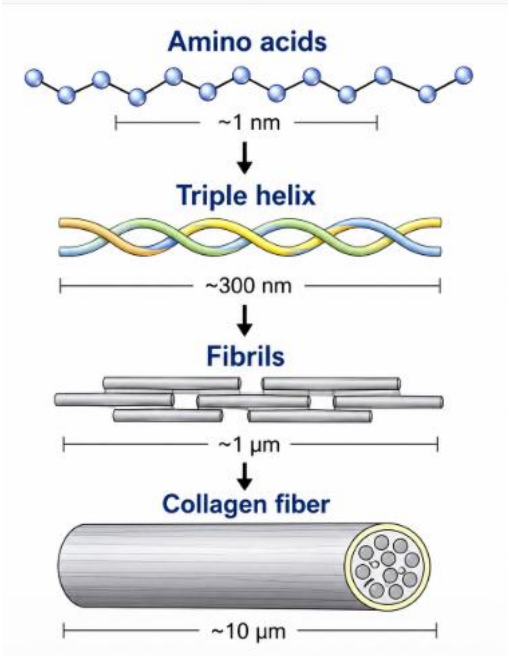

Figure 7. Hierarchical organization of collagen. Individual amino acids (~1 nm) assemble into a right-handed triple helix (tropocollagen, ~300 nm). Tropocollagen molecules align end-to-end and staggered to form fibrils (~1 µm), which bundle together into collagen fibers (~10 µm).

1.4.2 Collagen Types

There are approximately 29 types of collagen, classified by various factors. These include their protein's primary structure, the length of the triple-helical domain, the charge profile of the helix, interruptions within the triple helix, and the size and shape of the terminal domain [77]. These structural differences are crucial in determining the specific functional properties of each collagen type.

For example, fibril-forming collagens such as types I, II, III, V, and XI are elongated, rod-like molecules about 300 nm long. Among these collagen types, I, II, and III are the most common, accounting for 80–90% of total body collagen [78]. Collagen type I is a heterotrimer with two α1 (I) chains and one α2 (I) chain, featuring a triple helix structure. It is the main component in tendons, skin, ligaments, cornea, and many other interstitial tissues, accounting for 25% of the dry protein mass and over 90% of the organic matrix of bone [79]. Collagen type II is a homotrimer comprising three α1 (II) chains. It and its associated minor collagens tend to be more glycosylated than type I–rich fibrils. Collagen type II is found almost exclusively in cartilage, where additional minor collagens and noncollagenous glycoproteins are vital for modulating fibril diameter, surface properties, and interfibrillar interactions [80]. Collagen type III is a homotrimer consisting of three α1 (III) chains. In extensible tissues like skin, vessel walls, and the reticular fibers of lungs, liver, and spleen, collagen type III often coexists with collagen type I in collagenous fibrils [81].

Conversely, collagen types IV, VIII, and X form complex networks, with type IV collagen molecules approximately 400 nm long. Types VIII and X, known as "short-chain" collagens, create networks essential for building the structural framework within tissues [82]. Additionally, some collagens do not form homotypic fibers or networks. For instance, type IX collagen coats the surface of type II collagen fibers, illustrating a unique structural interaction [83].

1.4.3 Relationships Between Mechanical Properties and Collagen-Rich Tissues

The excellent mechanical properties of tissues that depend on fibrillar collagen result from their highly organized structure across many hierarchical levels. The interaction between structures, from the molecular level to fibrils and interfibrillar components, is essential for the overall mechanical behavior. When tissue is stretched, two primary mechanisms occur: molecular elongation and shear within a fibril, and shear deformation of the proteoglycan-rich matrix between fibrils. Proper supramolecular arrangement and cross-linking within each fibril are therefore crucial. The tissue's response to stress depends strongly on the strain rate. High strain rates cause collagen molecules to elongate and induce shearing within a fibril, while slow shear rates lead to shear of the matrix between fibrils, resulting in creep [84].

At small strains, kinks are straightened in the collagen structure, first at the fibrillar level and then at the molecular level. Higher strains are believed to induce molecular gliding within fibrils, eventually disrupting fibril structure. Preliminary attempts to quantify these distortions by analyzing changes in the collagen axial structure were only partially successful. In similar studies, three basic models for molecular elongation and rearrangement of collagen within a fibril were proposed. The first model suggests that molecular elongation results from a change in the helical pitch. The second model indicates an increase in the length of the gap region. The third model shows that a relative slippage occurs between laterally adjoining molecules [85].

It has also been observed that the strain within collagen fibrils is always significantly less than in the entire tendon. This phenomenon remains poorly understood but suggests the presence of additional gliding processes occurring at the interfibrillar level [86]. Once again, this indicates that fibril surface and interfibrillar interactions play a more important role than usually recognized. Consequently, this area warrants more attention than it currently receives.

1.4.4 Electrospinning of Collagen

In 2002, the electrospinning of collagen using HFIP as a solvent was first reported [87]. Since then, numerous studies on electrospinning and the characterization of collagen fibers have shown that this method can produce fibers that closely mimic the structural and biological features of natural collagen ECMs. Electrospun fibers of type I, II, and III collagen dissolved in HFIP exhibited a linear relationship between polymer concentration and average fiber diameter. Later, a gentler solvent, acetic acid, was used for electrospinning type I collagen. Compared to HFIP, acetic acid is less toxic, more cost-effective, and better maintains the ultrastructural integrity of collagen.

Recent studies have shown that collagen undergoes conformational changes during electrospinning, and the electrospun collagen fibers do not maintain their native structure [88]. Consequently, electrospun collagen lacks mechanical and structural stability when hydrated. Crosslinking is often necessary to enhance the stability of electrospun collagen. Crosslinking stabilizes the fibers by targeting the intramolecular covalent bonds. This is accomplished through the reaction of functional groups on the surface of the collagen fibers, enabling them to connect and form a water-stable network [89]. This process, called crosslinking, can control the biodegradation rate, creating collagen networks that degrade at a specific rate into bioresorbable components such as amino acids.

Various crosslinking methods have been shown to effectively enhance the stability and mechanical properties of collagen-based nanofibers. These techniques can be classified into chemical, physical, biophysical, and photochemical crosslinking. Each crosslinking approach has exhibited different levels of structural and mechanical stability, mainly due to variations in the mechanisms, concentrations, and reaction times involved.

Chemical crosslinking with glutaraldehyde vapor has been studied the most, but this method is cytotoxic [90]. Physical crosslinking achieved by heat and dehydrothermal treatment (DHT) has also been used; however, this method compromises collagen stability due to thermal degradation [91]. Photochemical crosslinking offers an attractive alternative to these methods. Both ultraviolet light with riboflavin as a photoinitiator and green light with Rose Bengal have been proposed to stabilize collagen-based materials and improve their mechanical properties [92].

1.5 Chitosan

Along with collagen, chitin and chitosan are vital natural polymer materials. Chitin, after cellulose, is the second-most-common biopolymer on Earth. It is typically found in the exoskeletons of arthropods, shells of crustaceans, and insect cuticles [93]. Chitosan, a deacetylated form of chitin, is one of the few natural polymers that contain free amine groups in its backbone, endowing it with the properties of a polymeric hydrogel due to its high water-absorption capacity. It is also known for its biodegradability, antimicrobial activity, and low toxicity. Because of these qualities, chitosan has been used in a wide range of biomedical applications in recent years.

1.5.1 Chitosan Structure

Chitosan, produced by deacetylation of chitin, is a linear polysaccharide composed of β-(1→4)-linked *D*-glucosamine and *N*-acetyl-*D*-glucosamine, as shown in ***Figure 8***. The deacetylation process of chitin allows control over the degree of deacetylation (DD) and can modify the average molecular weight of chitosan. Chitin's average molecular weight (Mw) typically ranges from 1.03 to 2.5×10^6 g/mole. Meanwhile, the deacetylation process usually reduces the Mw of chitosan to a range of 1 to 5×10^5 g/mol. Despite the decrease in the polymer's molecular weight, the main reason for producing chitosan is the poor solubility of chitin [94].

Initially, because chitin's chemical structure closely resembles that of cellulose, research on chitin solvents has progressed alongside developments in cellulose research. Chitin is a long-chain polysaccharide, similar to cellulose. The inter- and intra-molecular hydrogen bonds, resulting from the presence of acetylamino and hydroxyl groups, make chitin highly aggregated and insoluble in most organic solvents. In contrast, chitosan dissolves easily in dilute acid solutions and contains amino and primary and secondary hydroxyl groups for further chemical modifications [95].

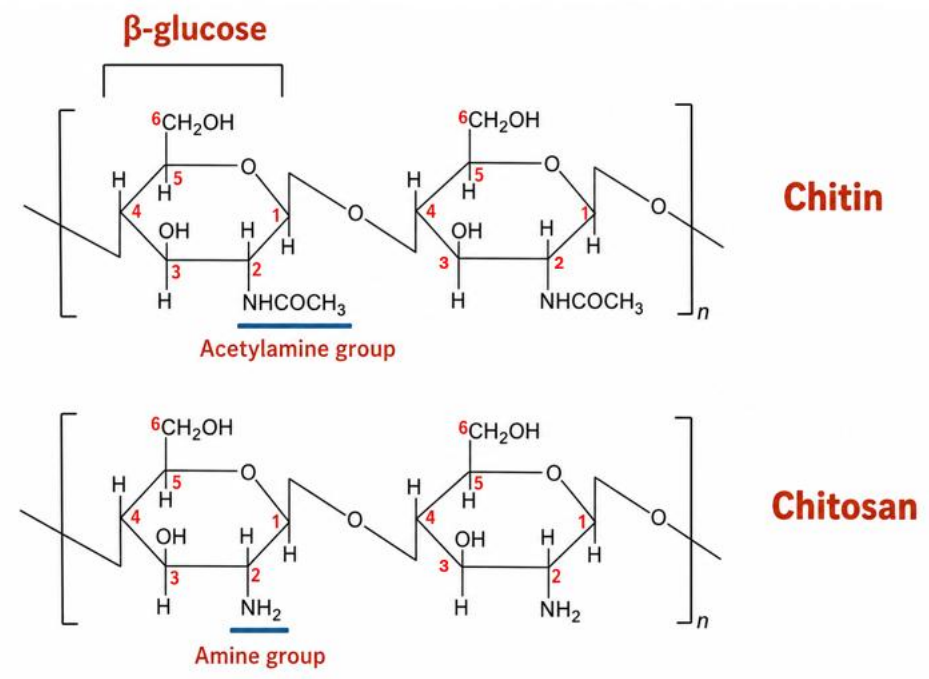

Figure 8. Chemical Structure of chitin and chitosan. Chitin consists of repeating β-(1→4)-linked *N*-acetyl-*D*-glucosamine units. Chitosan is produced by partial or full deacetylation of chitin and primarily contains β-(1→4)-linked *D*-glucosamine units, which are characterized by free amine (–NH_2) groups.

Because the deacetylated unit (*D*-glucosamine) and the acetylated unit (*N*-acetyl-*D*-glucosamine) are randomly distributed in chitosan, and because their composition depends entirely on the deacetylation process, the nomenclature of chitosan remains controversial. A group of deacetylated chitin with *D*-glucosamine residues exceeding 50% (or 60%) is often called chitosan; however, there is no clear boundary in the nomenclature distinguishing chitin from chitosan [96]. This confusion is likely caused by the fact that the percentage of DD in commercial chitosan ranges from 60 to 99%. As mentioned earlier, an important factor in naming something 'chitin' or 'chitosan' is its solubility in dilute aqueous acid solutions. Regardless of the DD percentage, if a deacetylated chitin is insoluble, it cannot be classified as chitosan. In addition to DD, the Mw of chitosan is another important characterization parameter because the application field of chitosan can vary widely with the distribution of Mw [97].

From a chemical perspective, acids and alkalis can be used to deacetylate chitin; however, alkaline deacetylation is preferred because glycosidic bonds are highly susceptible to acid hydrolysis. In the alkaline deacetylation process of chitin, both heterogeneous and homogeneous hydrolysis methods have been utilized. Heterogeneous hydrolysis involves harsh conditions: a hot, concentrated NaOH solution for several hours. This method can produce deacetylated chitin with a degree of deacetylation (DD) of up to 80%, but it remains

insoluble. Conversely, homogeneous hydrolysis employs very mild conditions at a deacetylation temperature of 25 °C, yielding soluble chitosan with a DD between 48 and 55 [98]. The deacetylation reaction under heterogeneous conditions results in an uneven distribution of *N*-acetyld-glucosamine and *D*-glucosamine residues, with some block-like distribution of acetyl groups along the polymer chains. Consequently, the solubility and aggregation behavior of chitosan in water can vary, influencing its native properties. For example, the physicochemical properties of such chitosans may differ from those of randomly acetylated chitosans produced under homogeneous conditions [99].

1.5.2 Chitosan Properties

Chitosan exhibits various physical, chemical, and biological properties. Its main characteristics are its cationic nature and unique behavior in solution. At low pH levels, usually below about 6.3, chitosan's amine groups are protonated, giving the polymer polycationic properties. These amine groups become deprotonated and reactive at higher pH levels (above 6.3). Typically, chitosan becomes soluble in all aqueous acidic media when the average degree of acetylation is less than 50%. It is soluble in dilute inorganic acids such as HCl, HBr, HNO_3, and $HClO_4$, as well as in concentrated H_2SO_4, organic acids like acetic, citric, formic, and lactic acid, and organic solvents such as tetrahydrofuran, ethyl acetate, and 1,2-dichloroethane [100]. Acetic and formic acids are the most commonly used solvents for chitosan solubilization. However, solubility is a complex parameter to control because it depends on factors like the degree of acetylation, ionic concentration, pH of the solution, the nature of the acid used for protonation, and also the distribution of acetyl groups along the macromolecular chain, which depends on the production conditions of chitosan [101].

The protonation reaction is interesting because, after dissolution, chitosan can be precipitated into films and membranes, spun into fibers or nanofibers, and also crosslinked to produce fibers or sponges. Processing chitosan is easier than processing chitin. However, the products' stability is lower due to their greater hydrophilicity and pH sensitivity. For better stability, chitosan may be crosslinked using epoxides or glutaraldehyde. Composites and blends are also produced by leveraging the polycationic properties of chitosan under acidic conditions [102].

The presence of amino groups explains most of chitosan's biological properties. Red blood cell membranes, which are negatively charged, can interact with the positively charged chitosan chains. Additionally, chitin exhibits less effective hemostatic activity than chitosan,

supporting this explanation. It is widely regarded as a non-toxic, biologically compatible, and environmentally friendly product [103]. Chitosan has attracted significant interest because of its diverse bioactive effects. Its polycationic nature primarily accounts for its interactions with proteins, lipids, genetic material, anionic molecules, and other biological compounds. A broad range of biological activities of chitosan has been documented, including its ability to induce resistance mechanisms and promote growth in plants; antiviral, antifungal, and antibacterial effects; and various biomedical applications (hypocholesterolemic effect, genetic material transfection, wound healing promotion) [104].

1.5.3 Chitosan Derivatives

Chitosan dissolves in acidic aqueous solutions and is easily modified under controlled conditions. In addition to the primary amino group, chemical modifications can be achieved through reactions involving the primary and secondary hydroxyl groups at C2, C3, and C6. To improve the solubility of chitosan in physiological fluids, enhance its biocompatibility, mucoadhesiveness, and adsorption properties, and add new functionalities, many chitosan derivatives have been synthesized or formulated over the past decades, while retaining their overall beneficial qualities in physiological environments. Here, some chemical strategies for modifying chitosan are reviewed.

1.5.3.1 Hydrophobic Modifications

Several hydrophobic modifications have been developed to tailor the properties of chitosan for specific applications. The most important of these are presented in the following section:

***N*/O-Acyl Chitosans:** Acylation of chitosan enables the attachment of hydrophobic side groups to amino and/or alcohol groups, providing great flexibility for chemical modification. *N*-Acylation can be easily achieved by reacting chitosan with anhydrides or acyl halides in various aqueous and organic solvents, or through coupling reactions. These methods can be precisely controlled due to the different reactivities of amino and hydroxyl groups. As a result, many chitosan derivatives with amphiphilic properties have been developed. Attaching hydrophobic side groups significantly changes the physicochemical properties of the polymers. This modification results in the formation of various chitosan-based macromolecular assemblies, including hydrogels, membranes, films, and fibers, which are used in biomedical and technical applications across the chemical and pharmaceutical industries [105].

***N*-Alkyl Chitosans:** *N*-alkylation targets the primary amino group of chitosan, which reacts with aldehydes and ketones to produce an intermediate reaction product, such as a carbinolamine. This intermediate dehydrates to form Schiff bases (aldimines and ketimines), which are then converted into N-alkyl derivatives upon treatment with suitable reducing agents, such as sodium cyanoborohydride, enabling selective reduction of imines. *N*-alkylation of chitosans may enhance blood clotting. Wang et *al*. [106] synthesized *N*-alkylated chitosans with different carbon chain lengths and used these materials to create nanofiber membranes via electrospinning. Various tests assessing biocompatibility and blood coagulation properties showed that membranes made from *N*-alkylated chitosan nanofibers were non-cytotoxic and demonstrated effective blood clotting abilities by activating coagulation factors and platelets.

1.5.3.2 Hydrophilic Modifications

Hydrophilic modifications are another important strategy used to improve the properties of chitosan. These modifications are presented in the following section:

***N*/O-Carboxyalkyl Chitosans:** Carboxyalkyl chitosans have been developed in various forms and extensively researched for potential applications in medicine and industry. Most are derivatives of carboxymethyl chitosan (CMCS), which can be synthesized as N-, O-, N,O-, or *N*,*N*-CMCS, depending on reaction conditions and reagents used [107].

Quaternized Chitosan Derivatives: Chitosan to greatly increase its solubility. One effective method is quaternization of chitosan or its derivatives, which converts the primary amino groups into quaternary ammonium ions and adds positive charges to the polymer. In addition to improving solubility, quaternized chitosans exhibit increased antimicrobial activity and have enhanced mucoadhesiveness, epithelial absorption, and drug/DNA delivery capabilities compared to unmodified chitosan [108].

1.5.4 Electrospinning of Chitosan

It’s difficult to produce nanofibers via electrospinning because its polycationic nature, arising from the many amino groups in its structure, increases the solution's surface tension. [109].

A study reports the optimal conditions for electrospinning chitosan with different molecular weights using various acid solutions, including acetic, hydrochloric, formic, and lactic acids. It was found that only solutions containing 80%, 85%, and 90% acetic acid

produced uniform fibers, with the best conditions being 3 wt% chitosan in a 90% acetic acid solution [110].

Three distinct molecular weight chitosan samples were dissolved in TFA. The fibers from low-Mw chitosan exhibit branching, whereas those from medium- and high-Mw chitosan form uniform fibers with nanofiber diameters ranging from 70 to 108 nm [111]. The spinnability of chitosan was reportedly improved by alkaline hydrolysis over various durations (0.75-48 hours). The molecular weight decreased from 1095 to 416 kDa at 24 hours and to 294 kDa after 48 hours of hydrolysis. It was observed that reducing the molecular weight made spinnability easier and resulted in more uniform fiber formation, especially for fibers derived from hydrolyzed chitosan (48 hours) [112]. Additionally, fibers could be produced at lower acetic acid concentrations (70 vol%) from solutions containing hydrolyzed chitosan at up to 7.5 wt%.

1.6 Molecular Dynamics Simulation (MD)

Understanding the structures of biomolecules under various conditions is essential for grasping their interactions and functions. However, directly measuring the real-time, time-dependent behavior of biological molecules across all conditions is challenging. Therefore, developing a thorough understanding of complex, dynamic biological processes, including protein stability and folding, conformational changes, ion transport, and enzymatic reactions, is vital to progress in fields such as pharmaceutical research. Simulations help address this challenge by using computational techniques. They also help reduce long-term time and cost issues. Experimental biological samples are expensive, and if a trial fails, researchers incur significant time and financial losses.

Molecular Dynamics (MD) simulation is a computational technique that uses Newton's equations of motion to model the motion of atoms and molecules over time, revealing dynamic behaviors and conformational changes in biomacromolecules. Several software programs are available for conducting molecular dynamics simulations of biomolecules, including GROMACS, VMD, and UCSF Chimera. GROMACS is a highly valuable, fast, free, user-friendly, and high-performance molecular dynamics software package developed at the University of Groningen in the Netherlands. [113].

1.6.1 Steps for Running a GROMACS MD Simulation

Running an effective simulation typically involves a series of sequential steps, as shown in ***Figure 9***.

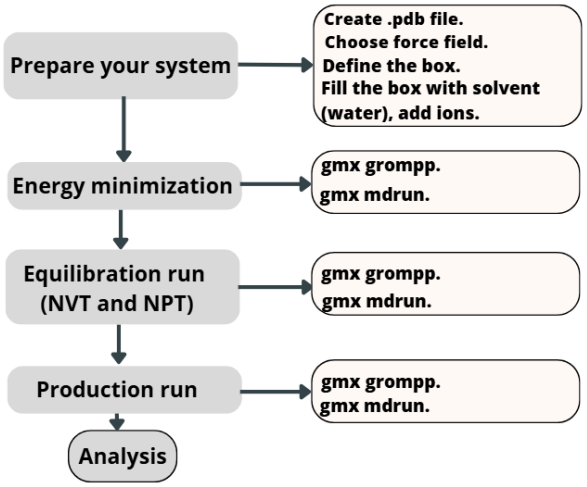

Figure 9. General steps to run a GROMACS MD simulation. The workflow begins with system preparation, including generating the initial structure file, selecting an appropriate force field, defining the simulation box, performing water solvation, and adding ions. This is followed by energy minimization using gmx grompp and gmx mdrun to remove unfavorable contacts. Equilibration is then performed under NVT and NPT ensembles to stabilize the system. A production MD run is subsequently carried out to generate trajectories for the system of interest. Finally, the resulting simulation data are analyzed to extract structural, dynamical, and thermodynamic properties.

The simulation setup begins with Model Selection: a system of interest must be chosen. In many cases, complete structural models are readily available for direct use. However, when suitable models are unavailable, researchers may construct an initial structure from scratch using computational tools such as CHARMM-GUI before proceeding with the simulation setup. The next step is to select and apply a suitable force field. Examples of force fields supported by GROMACS include AMBER, CHARMM, GROMOS, and OPLS. The choice of force field for a specific simulation primarily depends on the molecular system and the desired level of complexity. These can be classified into two groups: bonded and nonbonded. The terms representing bonded interactions account for bond stretching, valence angle bending, and dihedral rotation. The terms representing nonbonded interactions aim to capture electrostatics, dispersion, and Pauli exclusion. For example, the Amber ff14sb force field includes bonded terms (bonds, angles, dihedrals) representing intra-molecular interactions and nonbonded terms (van der Waals, electrostatics) capturing inter-molecular forces, providing a comprehensive description of molecular behavior in simulations [114].

After completing the force-field specification, a simulation cell is created by applying periodic boundary conditions. This step ensures that the simulation is not influenced by interactions with the surrounding environment, typically a vacuum. The created simulation box helps to reduce edge effects between the two different domains [113]. Next, the final step in the setup stage is to solvate the target molecule and add ions. During this step, molecules in the simulation box are surrounded by water and salt ions, which are added either to neutralize

the system's overall charge or to impose a net positive charge. The common, straightforward water models TIP3P and SPCE are most frequently used in MD simulations because they are computationally economical [115].

After selecting a force field and water model and configuring an appropriate simulation box, the GROMACS simulation begins. This phase starts with energy minimization, which aims to eliminate steric clashes and poor geometric features in the molecule's structure under study. [116]. The next step involves NPT and NVT equilibration, after which the system is designated as an isobaric–isothermal ensemble and a canonical ensemble, respectively. NVT ensures that a constant number of atoms N, a fixed volume V, and a fixed temperature T are maintained throughout the simulation. Conversely, NPT guarantees that a constant number of atoms N, as well as a constant pressure P and temperature T, are preserved during the simulation. Calibrating the system this way helps ensure that temperature, pressure, or volume fluctuations are minimal during analysis of the modeling results. It also allows for a more direct comparison to real-world processes, which are typically performed at relatively constant temperature and pressure [116].

After completing all these previous steps, the MD simulation can finally be executed. The length of the simulation will ultimately depend on the complexity of the model built during the earlier steps.

1.6.2 Applications

MD simulations have a wide range of applications not only in the biological sciences but also in physics, chemistry, and meteorology. We will focus on the applications of MD simulations in biological complexes.

- Determination of structures and movements of biomolecules: Structures identified through experimental methods such as X-Ray Crystallography or NMR studies provide only an average estimate of what the actual structure might be. However, computational simulation techniques enable a more accurate assessment of the structural fluctuations that molecules undergo. By analyzing these simulations, one can measure the movements of different regions of the molecule at equilibrium and the types of structural fluctuations that occur [117]. These simulations can also reveal the dynamic behavior of water molecules and salt ions, which are often essential for the proper function of proteins and ligand binding.
- Analyzing MD simulation results of various systems helps answer questions about the roles of structure, flexibility, and interactions among different biomolecules that are difficult to study experimentally.

- Provides insights into molecular interactions over time: Molecular dynamics simulation generates detailed views of atomic-level changes in biomolecular systems. Using the temporal scale of MD simulations enables us to predict various cellular interactions and behaviors, allowing modifications to existing structures to be observed. It is highly useful for studying the properties of samples that could serve as effective drugs.
- Docking is the process by which two or more molecular structures align themselves to bind and form a stable complex. MD simulation is commonly used to examine interactions such as protein-ligand, protein-protein, DNA-protein, and DNA-ligand. Researchers are eager to investigate the effects of new molecular interactions. Therefore, docking is performed first, followed by MD simulation to observe how interactions evolve over time [118].

1.7 Literature Review

Electrospinning natural polymers like chitosan and collagen poses significant challenges due to their limited solubility, high molecular weight, polycationic nature, and complex hydrogen-bonding networks [119].

Collagen is especially difficult to electrospin because of its intricate hierarchical structure and triple-helical organization, which provide stability but poor solubility. Many studies have highlighted that collagen's limited solubility is a major obstacle to electrospinning and that this challenge is closely related to its unique molecular architecture.

Visser et *al*. [120] reported that challenges in electrospinning collagen nanofibers extend beyond solvent choice: even with non-fluorinated solvents such as acetic acid and ethanol, these solvents can disrupt the triple-helical structure, thereby affecting the nanofibers' mechanical and biological properties. To address this, Anaya Mauricio et *al*. [121] successfully applied a bicomponent solvent system of glacial acetic acid and ultrapure water (1:1), thereby preserving the triple helix of Type I collagen. Similarly, Bürck et *al*. [122] provided a detailed analysis of structural changes during electrospinning, showing that collagen almost completely unfolds in fluorinated solvents but partially retains its folded structure in HAc/EtOH, a mixed solvent of acetic acid (HAc) and ethanol (EtOH). Interestingly, their work showed that the electrospinning process itself induces partial refolding, thereby increasing the abundance of polyproline II (PP-II) helices. However, this refolding remains limited, with the PP-II fraction not exceeding 42% across all initial solvent systems. These findings emphasize that both solvent composition and the spinning process are crucial in determining the final secondary structure of electrospun collagen nanofibers.

Collagen's hierarchical structure and extensive crosslinking add complexity, requiring controlled solubilization conditions that depend on the collagen source and intended use [123]. Supporting this, a study comparing acetic acid (HAc), hydrochloric acid (HCl), and phosphoric acid (H_3PO_4) at pH ≈ 3.0 found that collagen largely kept its triple-helical structure in all three solvents. The authors attributed this to the high proton concentration at low pH, which maintains a favorable surface charge on collagen, allowing slight loosening of the helix and better dispersion without losing structural integrity [124].

In addition to solvent effects, hydration is the key environmental factor affecting collagen stability. Interchain hydrogen bonds maintain the triple helix and are mostly unaffected by temperature and pressure, but water content directly influences mechanical properties and structural integrity. At low hydration, tightly bound water enhances intermolecular interactions and stabilizes fibrils, while at high hydration (>130%), water acts as a lubricant, enabling molecular sliding and partial disassembly [125]. These hydration-driven changes regulate collagen's stiffness.

At the molecular level, specific amino acids and their spatial arrangements within tropocollagen also play crucial roles. Glycine, proline, and hydroxyproline are especially important because they promote triple-helix formation and provide thermal stability. Gautieri et *al*. [126] demonstrated that these amino acids, along with surrounding water molecules, are vital for maintaining thermal stability, while other studies show that bond ruptures under tensile stress tend to occur at specific residues, notably proline in the X-position, indicating weak points in the structure. Research by Lees et *al*. [127] revealed that water content and intermolecular cross-link density influence fibril packing and organization, leading to quasi-hexagonal or rectangular arrangements that vary across tissues.

Overall, this research demonstrates that collagen's limited solubility and electrospinning behavior are affected not only by solvent chemistry but also by its complex hierarchical structure. This hierarchical organization is crucial to collagen's stability and functional properties, so many studies focus on understanding the physicochemical basis of triple-helix stability and its influence on fibril formation. Different collagen types and sources have unique structural and functional characteristics. For example, bovine collagen is abundant and widely used in biomedical applications, yet it often shows heterogeneity and partial loss of structural integrity during extraction and processing. Researchers are

increasingly exploring recombinant or synthetic collagen as a more consistent and controllable alternative to address these issues.

However, producing collagen outside its natural environment is very challenging. It requires specific post-translational modifications, most importantly the hydroxylation of proline residues, and controlled conditions to mimic the natural self-assembly process that forms ordered fibrils. Doing both steps is technically difficult. Additionally, even in native collagen, tropocollagen molecules assemble into supramolecular fibrils in a partially random way, resulting in areas of tightly packed and loosely packed molecules. The ways in which this natural heterogeneity affects collagen's structural organization, mechanical properties, and biological functions remain poorly understood. Because these mechanisms are not yet fully known in nature, predicting or controlling how collagen produced through recombinant or synthetic methods will assemble remains very difficult, making this an important area for further research.

The same issue applies to chitosan. Electrospinning chitosan is difficult mainly because of its limited solubility, which is strongly influenced by the degree and pattern of *N*-acetylation. The *N*-acetyl groups control intramolecular hydrogen bonding and electrostatic interactions; higher degrees of acetylation make the chains more rigid and less soluble, mainly when the acetyl groups are unevenly distributed [128]. Other studies indicate that disrupting chitosan's crystallinity through chemical or physical methods can significantly improve its solubility across a broader pH range, highlighting crystallinity as a significant structural barrier to dissolution [129].

To understand these mechanisms at the molecular level, researchers have used molecular dynamics simulations to explore how acetylation and self-assembly influence chitosan's properties. One study examined the self-assembly of chitosan with various degrees and patterns of acetylation and found that 10-mer chitosan chains with 50% acetylation, whether arranged in blocks or in alternating patterns, spontaneously formed ordered nanofibrils composed mainly of antiparallel chains, consistent with fiber diffraction data for deacetylated chitosan. Regardless of the acetylation pattern, fibril sheet formation was stabilized by similar intermolecular hydrogen bonds, with water-mediated interactions supporting the stacking of these sheets. Notably, acetylated units participated directly in forming strong hydrogen bonds ($NH–O_6$ and $O_6H–O_7$), providing a molecular explanation for the experimental observation that higher acetylation reduces solubility [130].

Complementary MD studies explored water absorption and structural changes in chitosan nanohydrogels, highlighting the effects of protonation, cross-linking, and pH. These studies confirmed that chitosan nanohydrogels can absorb water and swell regardless of the degree of cross-linking, but swelling relies heavily on pH, aligning with chitosan's known solubility below pH 6.5 and insolubility above it. At the molecular level, increased protonation reduces intramolecular hydrogen bonding, thereby affecting solubility and the nanohydrogels' structural behavior [131]. Additional MD simulations compared chitin and chitosan nanoparticles to investigate how chain arrangement influences conformation and solubility in water. The results showed that the spatial arrangement of polymer chains is a critical factor affecting structural properties and water interactions, ultimately determining solubility [132].

In response to these challenges, two main strategies have been developed to improve the electrospinnability of chitosan and collagen. First, dissolving the polymers in concentrated acidic solutions such as acetic acid or trifluoroacetic acid enhances solubility and reduces surface tension without significantly increasing solution viscosity; however, this approach may affect the biocompatibility of the final nanofibers [133]. Second, mixing these natural polymers with synthetic copolymers, such as polyvinyl alcohol (PVA) (***Figure 10***), has proven highly effective [134]. PVA forms strong hydrogen bonds with chitosan and collagen, stabilizing the spinning solution, lowering surface tension, and aiding in the production of uniform, continuous nanofibers, while also providing biodegradability, strength, and flexibility useful for biomedical applications [135].

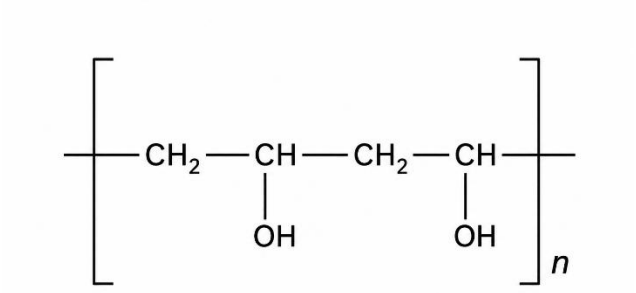

Figure 10. Chemical structure of polyvinyl alcohol (PVA).

Despite these advances, a significant gap remains. It is still unclear how the molecular structure of natural polymers affects their solubility in water and, consequently, their ability to form stable nanofibers. Understanding these relationships is essential for improving polymer solubility, ensuring solution uniformity, and refining electrospinning methods to reliably produce high-quality nanofibers.

1.8 Research Aim

1.8.1 Tropocollagen Architecture

To understand how variations in tropocollagen packing influence collagen fibril structure and stability, this study will utilize molecular dynamics (MD) simulations to compare tightly packed (hexameric) and loosely packed (heptameric) assemblies enriched with proline or hydroxyproline residues. The aim is to uncover how these different packing arrangements govern supramolecular organization and the long-term stability of collagen fibrils.

1.8.2 Solution Properties in Electrospinning: Insights from Molecular Modeling and Experiments

To investigate how polymer–solvent interactions influence solubility and nanofiber formation during electrospinning, this study combines electrospinning experiments with MD simulations on polyvinyl alcohol (PVA), chitosan, and collagen. The experimental work will evaluate nanofiber formation and morphology, while simulations will analyze hydrogen bonding, solvation, and intra- and inter-chain interactions that affect electrospinnability. The aim is to identify key molecular factors that restrict the electrospinning of natural polymers.

1.8.3 Computational and Experimental Study of PVA-Biopolymer Blends

This study combines experimental and computational methods to investigate how blending PVA with natural polymers improves solubility and spinnability and how molecular interactions within these blends affect nanofiber formation. The experimental part will electrospin chitosan–PVA and collagen–PVA blends to analyze fiber formation and morphology. At the same time, MD simulations will examine solubility and key molecular interactions, including hydrogen bonding, within these blends. The goal is to understand how PVA blending stabilizes the spinning solution and enables the production of uniform, high-quality nanofibers.

Chapter 2: Tropocollagen Architecture

2.1 Summary

Collagen is the most prevalent protein in living organisms, playing diverse roles across multiple tissues. Its hierarchical structure relies on the assembly of tropocollagen, the fundamental building block of collagen fibrils. This assembly occurs in a predominantly random manner, allowing for variations in packing. This randomness can lead to regions of both tight and non-tight packing within the fibrils. The mechanisms by which these regions influence collagen's packing configurations, structural organization, and functional properties remain poorly understood. Previous studies have shown that synthetic collagen peptides designed using computational models can form fibers that mimic the hierarchical structure of native collagen. These fibers exhibit mechanical and structural properties similar to those of natural collagen [136], highlighting the practical applications of simulation-driven design. Using molecular dynamics simulations, this chapter provides a focused comparison of tightly packed (hexameric) and less tightly packed (heptameric) tropocollagen configurations enriched in proline or hydroxyproline residues.

2.2 Methods

2.2.1 Simulation Systems

In this study, molecular dynamics (MD) simulations were employed to model the behavior of hexameric and heptameric tropocollagen strands in water. These simulations provide critical insights into the roles of tropocollagen assembly and the impact of proline and hydroxyproline on the structural stability and dynamic properties of collagen fibrils. Each system was simulated in water without added ions to create the controlled environment of the synthetic laboratory. This method differs from how collagen forms in living organisms. In those situations, various biomolecules, such as enzymes, and factors, such as ion concentration, temperature, and pH, add complexity to the process. Adding ions could alter collagen's structural integrity, diffusion dynamics, and fibril formation. Ions can also influence hydration shells and molecular charge distributions, leading to artificially induced conformational changes that may not accurately reflect the intrinsic behavior of tropocollagen in isolation. Therefore, eliminating ions ensures that the observed structural and dynamic properties are influenced solely by the molecular composition of tropocollagen rather than

external ionic effects. The simulations were carried out in a cubic box, and the number of molecules in each system is detailed in ***Table 1***.

Table 1. The molecular composition of the four systems (hydroxyproline-rich hexamer, proline-rich hexamer, hydroxyproline-rich heptamer, and proline-rich heptamer) includes the number of protein atoms, protein chains, total atoms, water molecules, and simulation box volume (nm^3).

Tropocollagen Systems	Protein Atoms	Protein Chains	Total Atoms	Water Molecules	Box Volume (nm^3)
hydroxyproline-rich hexamer	6390	18	171510	55040	1749.6
proline-rich hexamer	6228	18	173250	55674	1773.5
hydroxyproline-rich heptamer	7455	21	171510	54685	1749.6
proline-rich heptamer	7266	21	173241	55325	1773.5

2.2.2 Force Field

The force field parameters for all molecules used in this study are compatible with Amber99sb, a version designed to accurately predict the secondary structure of peptides, including α-helices and β-hairpins [137]. The TIP3P model was employed for water [138].

2.2.3 Model Systems

In our study, model tropocollagen structures were employed either glycine-proline-hydroxyproline (Gly-Pro-Hyp) triplets in the hydroxyproline-rich hexamer and heptamer systems or glycine-proline-proline (Gly-Pro-Pro) triplets in the proline-rich hexameric and heptameric tropocollagen systems.

2.2.4 Simulation Protocol

The molecular dynamics simulation employed the LINCS algorithm to constrain bond lengths, utilizing a time step of 2 fs [139]. A constant pressure of 1 bar was maintained using the Parrinello-Rahman barostat to scale the box volume isotropically [140]. The simulation temperature was set to 300 K and controlled using the V-rescale thermostat, which independently regulates polymer and solvent groups [141]. Non-bonded atom pairs were updated every ten simulation steps (nstlist = 10), and Lennard-Jones interactions were truncated at 1.0 nm (rvdw = 1.0), with energy and pressure dispersion corrections applied to mitigate cutoff length effects and ensure compatibility with the Amber99sb force field. Periodic boundary conditions were enforced in all dimensions (xyz). Electrostatic interactions were computed using particle-mesh Ewald (PME) summation [142], employing an interpolation order of 6, a direct sum tolerance of 10^{-5}, and a real-space cutoff of 1.0 nm. These simulations were conducted using the GROMACS 2020 software package [143].

2.2.5 Analysis

VMD software was used to render the primary structures of the hexamer and heptamer tropocollagen, as shown in ***Figure 11***.

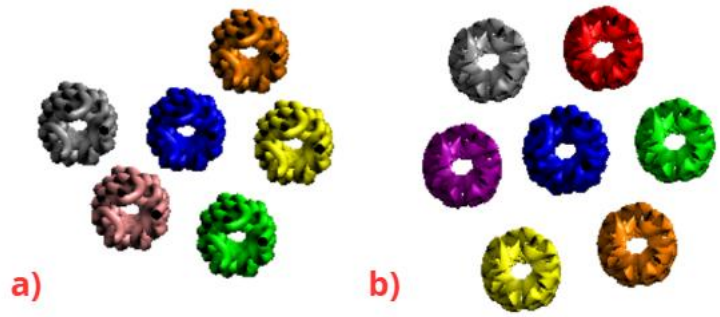

Figure 11. Configurations of tropocollagen: (A) Hexamer composed of six tropocollagen strands; (B) Heptamer composed of seven tropocollagen strands.

The study commenced with a preliminary 100 ns simulation. Initial configurations were generated using the g_cluster program with the grooms method. This method is the most widely used clustering algorithm in GROMACS for clustering trajectories by RMSD [144]. In this approach, the protein backbone atoms of all structure pairs (extracted from the simulation frames) were calculated and grouped according to a 1.0 nm cutoff. The structure with the highest number of atoms was designated as the central structure, and all structures within this cutoff distance were assigned to the same cluster. The algorithm removed this cluster from the remaining structures and repeated the clustering process to generate groups of non-overlapping clusters, each with a central structure. Following this selection, each system underwent a 2000 ns production run using the configuration of the central structure from the largest cluster. Consequently, four systems were analyzed: hydroxyproline-rich hexamer, proline-rich hexamer, hydroxyproline-rich heptamer, and proline-rich heptamer. Data from these 2000 ns runs were analyzed and are presented.

2.2.6 Tropocollagen Interactions

To understand interactions among tropocollagen strands, the *gmx mindist* tool was used to count contacts between each triple helix and the other helices in the system. In our case, contacts are defined by a distance cutoff of 0.6 nm. The propensity for hydrogen bonding was determined by counting the occurrences of hydrogen-bond formation between atoms that donate and accept hydrogen bonds within (intramolecular) and between (intermolecular) triple helices. A hydrogen bond was recorded when the angle between the hydrogen bond donor, the hydrogen-bonded hydrogen, and the hydrogen bond acceptor was between 150° and 180°, and the distance between the donor and acceptor atoms was less than 0.35 nm [145]**.** The *plot_hbmap* script was used to calculate the percentage of hydrogen bonds

over the simulation time (2000 ns) [146]. The *gmx sasa* program calculated the solvent-accessible surface area (SASA), enabling us to explore how amino acid composition affects collagen's interaction with water molecules. The analysis categorized atoms into two groups: "Hydrophobic," including those in the system with charges ranging from -0.2 to 0.2, and "Hydrophilic," comprising those outside this range. These, along with the total solvent-accessible surface area, are presented for each system. The *gmx rmsf* tool calculates the root-mean-square fluctuation (RMSF) of the protein group for each system. This helps us understand how the fluctuations of individual amino acids, such as proline and hydroxyproline, influence the system's stability [147]. The *gmx msd* program was used to calculate the mean-squared displacement (MSD) of each helix, providing insight into the dynamic behavior of collagen over time. The Einstein relation was employed to calculate the diffusion coefficient. The *gmx energy* program was used to calculate the Coulombic and Lennard-Jones interaction energies between each triple helix and the remaining helices in the system. This analysis reveals the comparative roles of electrostatic and van der Waals forces in stabilizing the collagen triple helices.

2.3 Results and Discussion

The collagen models used in this study are denoted as $[(Gly\text{-}Pro\text{-}Hyp)_{30}]_3$ and $[(Gly\text{-}Pro\text{-}Pro)_{30}]_3$ and contain 90 amino acid residues per tropocollagen strand. This truncation was necessary due to computational limitations, as the full-length collagen molecule, which is 300 nm long, is too large for atomistic simulations. However, shorter fragments still provide atomistic insight into interactions between tropocollagen strands [148]. Gly-Pro-Pro sequences resist most peptidases due to proline's structural properties, allowing them to enter the bloodstream and retain biological activity. Gly-Pro-Pro peptides are proposed to serve important roles as atheroprotective and anticoagulant agents [149]. Additionally, this motif is essential for collagen stability, as proline affects ring puckering and backbone dihedral angles, which influence the packing and organization of the collagen triple helix [150]. The Gly-Pro-Hyp sequence is crucial for stabilizing the collagen triple helix. Its high abundance in collagen greatly contributes to the strength and flexibility of connective tissues, emphasizing its vital role in supporting various biological functions [151].

Hexameric and heptameric configurations of tropocollagen were selected for their relevance to proposed models of collagen molecular packing [152]. The hexamer structure represents the hexagonal arrangement observed in protofibrils, in which triple helices are organized in a symmetric pattern that contributes to the cylindrical lattice found in native

collagen fibers [153]. According to Orgel et *al*. [154], several conflicting microfibril models existed, including one with seven molecular chains arranged in a quasi-hexagonal lattice, with one central strand surrounded by a hexagon of six additional strands. This model has subsequently been established [155]. This is the heptamer, and it is considered quasi-hexagonal because the chains are not identical. Comparing these two arrangements provides insights into how variations in strand number and spatial organization affect inter-strand interactions, hydrogen bonding, molecular dynamics, and the overall stability of collagen assemblies. This approach deepens understanding of native collagen structure and guides the development of biomimetic materials.

2.3.1 Number of Contacts Between Tropocollagen Strands

Table 2 shows the average number of contacts with the number of contacts per tropocollagen in the proline- and hydroxyproline-rich tropocollagen strands in both hexameric and heptameric forms.

Table 2. The average number of contacts, along with the number of contacts per tropocollagen (Contacts per TC) and the standard error (SE), was calculated for each tropocollagen system: hydroxyproline-rich hexamer, proline-rich hexamer, hydroxyproline-rich heptamer, and proline-rich heptamer.

Tropocollagen Systems	Number of Contacts		
	Avg	SE	Contacts per TC
hydroxyproline-rich hexamer	7561.3	0.2	1260
proline-rich hexamer	7128.4	0.2	1188
hydroxyproline-rich heptamer	8527.8	0.2	1218
proline-rich heptamer	7589.0	0.3	1084

The results in ***Table 2*** show that hydroxyproline-rich systems have more contacts than proline-rich systems. This suggests that hydroxyproline helps create a more stable molecular structure. The contacts indicate where the tropocollagen strands interact more frequently, suggesting tighter packing. This is notable despite the Hyp-containing tropocollagen strands having an extra OH group. The extra space provided for the OH group induces tighter packing between the strands even without the formation of covalent cross-links. The higher number of contacts in hydroxyproline-rich systems suggests enhanced structural stability and potentially higher resistance to deformation, key characteristics for effective fibril assembly. The tighter packing afforded by Hyp could be why hydroxyproline enhances collagen's structural stability more effectively than proline does [156]. This phenomenon is observed in both the heptamer and the hexamer. The additional triple helix in the heptamer increases interactions and binding with surrounding molecules, thereby enhancing stability. Consequently, the heptamer is more rigid and stable than the hexamer, making it better suited for tissues that require high

mechanical support. Therefore, collagen stability is influenced by residue-residue contacts, impacting its overall mechanical properties. This emphasizes the need to maintain these contacts to prevent the structural dissociation into individual tropocollagen strands.

2.3.2 Hydrogen Bonds Both Within and Between Tropocollagen Strands

Table 3 provides the average number of hydrogen bonds observed within and between the tropocollagen strands, along with the total number of bonds for the hydroxyproline-rich hexamer, proline-rich hexamer, hydroxyproline-rich heptamer, and proline-rich heptamer systems. The number of hydrogen bonds within the tropocollagen strands was slightly higher in the proline-rich systems than in the hydroxyproline-rich ones. However, the Hyp-rich tropocollagens had more hydrogen bonds between tropocollagen strands than the proline-rich systems did. While these intramolecular bonds contribute to the stability of tropocollagen, their influence is relatively minor compared to those of glycine, with its small size, and proline, with its fixed ϕ angle [157]. Glycine, the smallest amino acid, perfectly fits the tight spaces within the triple helix structure. Its presence in every third residue is critical for compactly packing the triple helix and vital for maintaining its stability [158]. Studies show that hydrogen bonds between the NH groups of glycine and the CO groups of adjacent amino acids are essential for maintaining the triple helix structure at the molecular level [159]. The fixed ϕ angle is crucial for properly aligning collagen chains, enabling the formation of the triple helical structure. Various studies have shown that alterations in proline or glycine residues destabilize helices [160].

Table 3. The average number of bond interactions, the number of bonds per tropocollagen (Avg/TC), and the total number of bonds (Sum/TC) were observed for each system: hydroxyproline-rich hexamer, proline-rich hexamer, hydroxyproline-rich heptamer, and proline-rich heptamer. The standard error (SE) reflects the variability of the averages across the runs.

Tropocollagen Systems	Hydrogen Bonds							
	Within Tropocollagen Strands			Between Tropocollagen Strands			Total	
	Avg	SE	Avg/TC	Avg	SE	Avg/TC	Sum	Sum/TC
hydroxyproline-rich hexamer	23.8	0.1	3.9	3.8	0.3	0.6	27.6	4.6
proline-rich hexamer	24.2	0.2	4	1.9	0.2	0.3	26.1	4.3
hydroxyproline-rich heptamer	23.6	0.1	3.3	3.4	0.4	0.5	27	3.8
proline-rich heptamer	24.0	0.2	3.4	0.0	0.0	0.0	24.0	3.4

These results are similar to those shown in ***Figure 12***, which presents the average number of hydrogen bonds within and between the tropocollagens in each system. Most hydrogen bonds within tropocollagens are formed between the amide nitrogen of a glycine residue (acting as a hydrogen bond donor) and the amide oxygen of a proline residue (acting as a hydrogen bond acceptor. Additionally, hydroxyproline is essential in forming hydrogen

bonds between the tropocollagens. Specifically, most of the hydrogen bonds were formed between the oxygen atom in the hydroxyl group (-OH) bonded to the γ-carbon of the pyrrolidine ring of a hydroxyproline residue, acting as a hydrogen bond donor, and the oxygen (O) of a glycine or hydroxyproline residue, acting as a hydrogen bond acceptor.

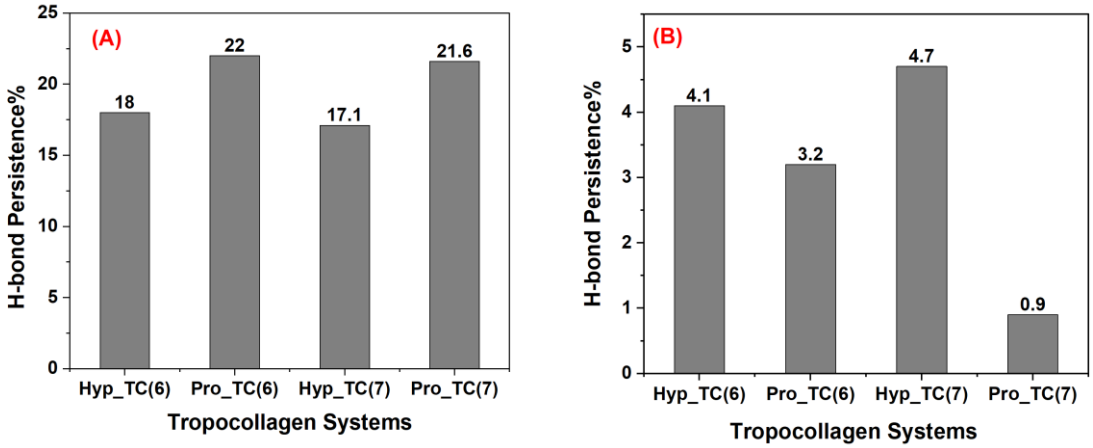

Figure 12. The average number of hydrogen bonds for each system: (A) within individual tropocollagen strands, (B) between strands. Systems analyzed include hydroxyproline-rich hexamer (Hyp_TC(6)), proline-rich hexamer (Pro_TC(6)), hydroxyproline-rich heptamer (Hyp_TC(7)), and proline-rich heptamer (Pro_TC(7)).

Adding a triple helix increases the number of these intermolecular bonds. The heptamer system has a higher number than the hexamer system. The cross-linking of tropocollagen is theorized to enhance its stability, not by improving the inherent stability of the triple helix, but through the properties of cross-linking and intermolecular interactions. Various studies support this perspective, emphasizing the role of cross-linking in improving collagen's thermal and mechanical properties [161].

2.3.3 Total, Hydrophobic, and Hydrophilic Solvent-Accessible Surface Area (SASA) of Tropocollagen Fragments

The surface area of a polymer that is available for interacting with neighboring molecules and solvent particles is known as the solvent-accessible surface area [162]. This factor is crucial for interacting with other environmental entities, including other polymers, proteins, carbohydrates, therapeutics, and small molecules [163]. These accessible regions have been divided into hydrophilic and hydrophobic regions, which can further predict how the molecule will partition between hydrophobic and hydrophilic media, such as the surface or the interior of a membrane, or between other hydrophobic or hydrophilic polymers or drugs. ***Figure 13*** shows that over 2000 ns, the average SASA values remained stable across all systems, indicating minimal fluctuations in the accessible surface areas of the total, hydrophobic, and hydrophilic regions. This is expected in the fixed aqueous environment,

since changes in surface area are most likely driven by large perturbations to the system or solvent.

.

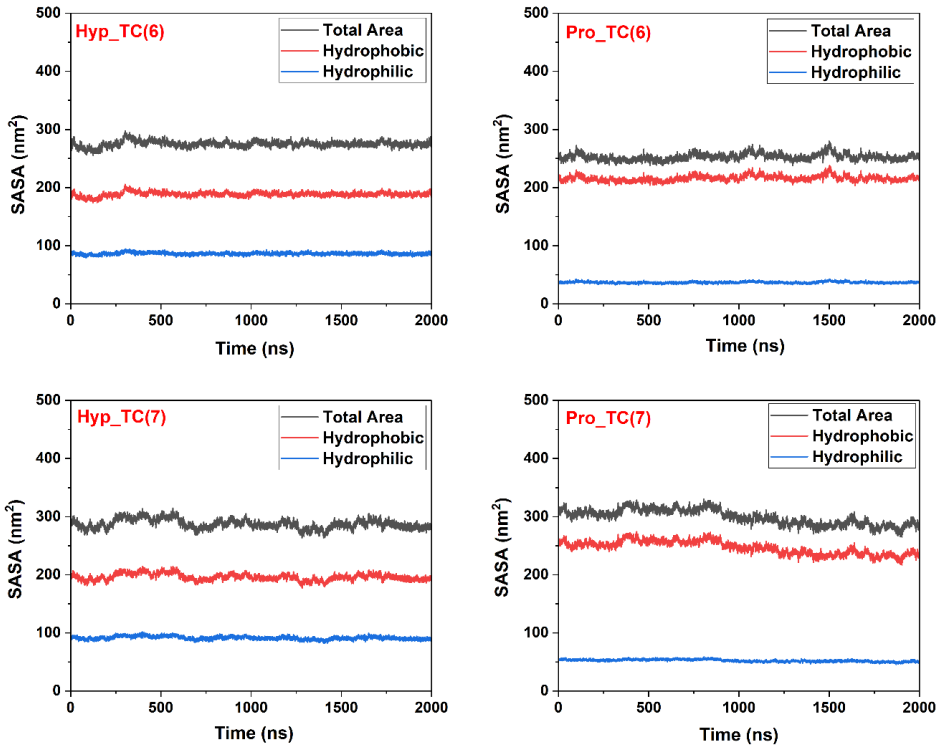

Figure 13. Average SASA over time of each system: hydroxyproline-rich hexamer (Hyp_TC(6)), proline-rich hexamer (Pro_TC(6)), hydroxyproline-rich heptamer (Hyp_TC(7)), and proline-rich heptamer (Pro_TC(7)). The black line represents the total SASA, the red line indicates the hydrophobic region, and the blue line denotes the hydrophilic region.

As noted in ***Table 4***, the heptamers' average total solvent-accessible surface areas are higher than those of the hexamers. This increase in SASA is attributed to an additional tropocollagen strand, which exposes a larger molecular surface area to solvent than in the corresponding hexamer. This is important for protein interactions and stability, especially since mutations associated with diseases often occur in regions of limited solvent accessibility [164]. This highlights the significance of SASA in protein functionality. When comparing the hydroxyproline-rich tropocollagens to the proline-rich ones, it is observed that hydroxyproline-rich systems have larger hydrophilic surface areas due to the additional hydroxyl group in hydroxyproline. This feature promotes enhanced interactions with water and other molecules, allowing these polymers to engage more effectively with hydrophilic molecules and surfaces, contributing to better assembly and fibril formation than proline-rich systems [165]. Simply converting the Hyp residues to Pro reduced the hydrophilic SASA by nearly half, a change greater than expected. These results suggest that this conversion could

shift collagen from hydrophilic to hydrophobic regions, alter the types of molecules that interact with collagen, and significantly alter its interactions with small molecules such as drugs and other therapeutics, both in molecular type and in kinetics and dissociation rates. Although proline-rich tropocollagen is not entirely hydrophobic, it is interesting to see the degree to which segments rich in proline and glycine contribute to its largely hydrophobic surface area [166].

The enlarged hydrophilic solvent-accessible surface area in hydroxyproline facilitates water interactions, influencing collagen's role in tissues and its molecular binding properties. In contrast, due to proline's amphiphilic nature, proline displays a lower hydrophilic SASA. It acts as a hydrotrope, assisting in the solubilization of hydrophobic molecules while maintaining a balance between hydrophilic and hydrophobic interactions. These findings underscore the importance of amino acid composition, particularly hydroxyproline and proline, in enhancing collagen stability.

Table 4. The average SASA values in nm² for the total surface in four systems (hydroxyproline-rich hexamer, proline-rich hexamer, hydroxyproline-rich heptamer, and proline-rich heptamer) are categorized by hydrophobic and hydrophilic regions. Includes percentages of hydrophobic and hydrophilic areas. The standard error (SE) is included to indicate the variability in the measurements.

Tropocollagen Systems	Solvent Accessible Surface Area (SASA) (nm^2)							
	Total		Hydrophobic			Hydrophilic		
	Avg	SE	Avg	SE	%	Avg	SE	%
hydroxyproline-rich hexamer	274.9	0.02	188.5	0.01	68.5	86.4	0.01	31.4
proline-rich hexamer	252.6	0.02	215.8	0.02	85.4	36.8	0.01	14.5
hydroxyproline-rich heptamer	287.5	0.02	196.1	0.02	68.2	91.3	0.01	31.8
proline-rich heptamer	299.1	0.03	246.6	0.03	82.4	52.4	0.01	17.5

2.3.4 Root Mean Square Fluctuation (RMSF) of the Protein Group within the Tropocollagens

RMSF is a measure commonly used to indicate the displacement of a specific atom or group of atoms from a reference structure [167]. The RMSF analysis offers insights into the dynamic regions of proteins and polymers, particularly flexible loops. Additionally, it can highlight the importance of specific regions in conformational changes and polymer interactions.

Figure 14 presents the average RMSF values for the protein group in each analyzed system at 400 ns intervals (400, 800, 1200, 1600, and 2000 ns). The data reveal that RMSF values stabilize at longer simulation times (e.g., 1200 ns, 1600 ns, and 2000 ns), indicating the system's approach to equilibrium. The analysis revealed that the heptamer and hexamer hydroxyproline-rich systems exhibited lower RMSF than the proline-rich systems. This finding suggests that hydroxyproline-rich tropocollagen structures may exhibit greater resistance to motion in an aqueous environment than proline-rich structures. The hydroxyl group in hydroxyproline is expected to promote additional hydrogen bonding and other polar interactions with solvent, small molecules, and surfaces in its environment, ultimately contributing to the structure's increased overall rigidity and stability [168].

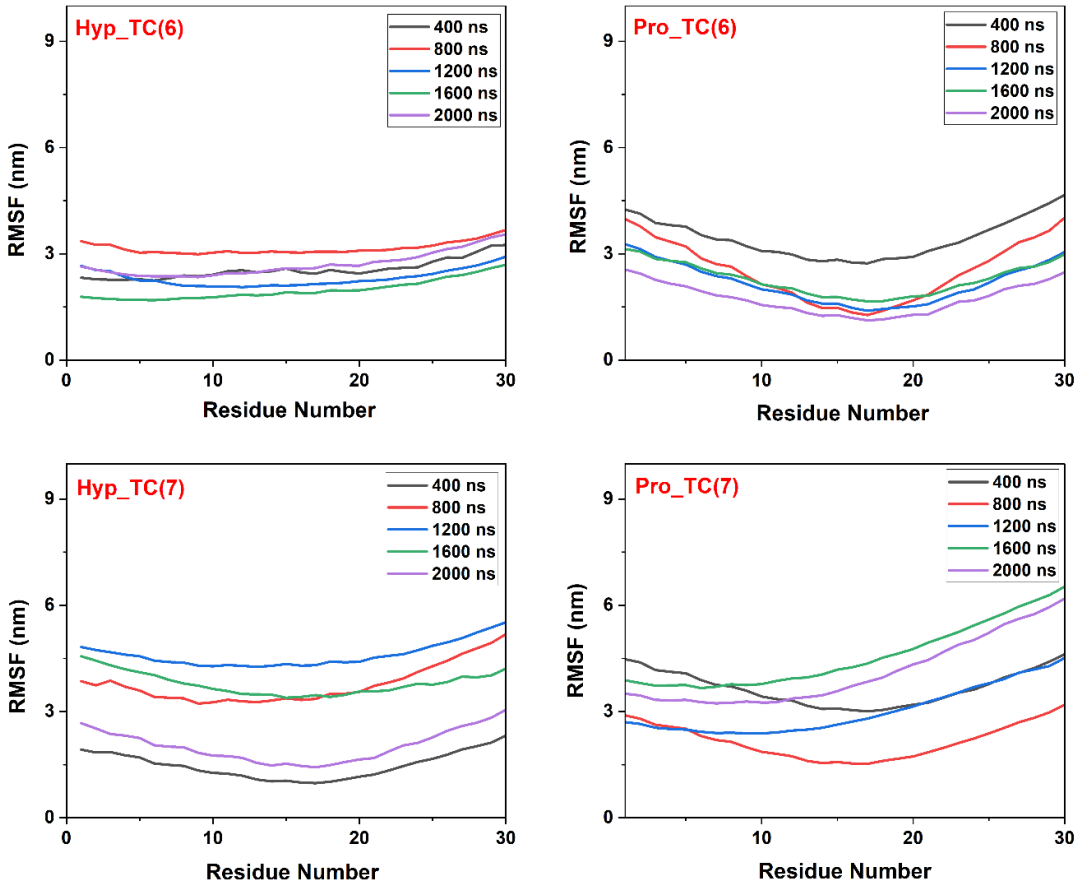

Figure 14. The average RMSF values of the protein group were calculated at 400 ns intervals for each of the four systems: hydroxyproline-rich hexamer (Hyp_TC(6)), proline-rich hexamer (Pro_TC(6)), hydroxyproline-rich heptamer (Hyp_TC(7)), and proline-rich heptamer (Pro_TC(7)).

Xu et *al*. [156] found that regions with a lower Hydroxyproline content are less stable and more susceptible to initial thermal disruption. This indicates that these areas are less rigid

and more flexible, especially under thermal stress, making them the initial sites of unfolding. Proline's flexible region affects the backbone parameters of alpha-helices, causing deviations that produce a kink of about 20-30 degrees. This distortion impacts the structural integrity and packing of proteins, especially in membrane and globular proteins [169].

Furthermore, our comparison of the tropocollagen heptamers and hexamers revealed a higher RMSF in the heptameric systems than in the hexameric ones, both in the case of the hydroxyproline and proline-rich tropocollagen. This higher RMSF indicates greater fluctuation. One possible explanation for this difference is that the greater number of chains in heptamers may confer greater flexibility. These results show that, although structural flexibility naturally increases with system size, hydroxyproline-rich systems exhibit a smaller increase in RMSF, indicating that hydroxyproline contributes to greater stability and resistance to dynamic fluctuations, even in larger assemblies.

2.3.5 Mean-Squared Displacements (MSD)

The mean-squared displacement is a parameter commonly used to characterize atomic movement [170]. Specifically, global mobility, as measured by MSD, reflects how the entire tropocollagen molecule responds to its environment, including diffusion, hydration effects, and larger-scale conformational changes, which are important in processes such as fibril assembly, network formation, and integration into extracellular matrices [171]. The diffusion coefficient (D) quantifies molecular mobility by indicating how easily molecules spread in a medium. A higher diffusion coefficient yields a greater MSD over time, whereas a lower diffusion coefficient results in restricted motion and a lower MSD. ***Figure 15*** shows that systems rich in hydroxyproline exhibit higher MSD than those rich in proline. The higher MSD observed in hydroxyproline-rich tropocollagen systems is primarily due to the strong interactions between hydroxyproline’s hydroxyl groups and surrounding water molecules. These –OH groups are highly hydrophilic and form extensive hydrogen bonds with water, creating a dynamic and structured hydration shell around the collagen molecule [172]. This hydration shell facilitates greater solvent molecular mobility, thereby increasing global motion in molecular dynamics simulations. Importantly, this increased MSD does not indicate reduced structural stability. On the contrary, hydroxyproline stabilizes the collagen triple helix by forming intermolecular hydrogen bonds between adjacent collagen chains, leading to tighter packing, increased contact numbers, and decreased RMSF values as previously noted. Thus, hydroxyproline-rich systems exhibit a unique behavior in which the internal structure remains rigid and stable, while the entire molecule undergoes greater motion in the solvent

environment. This dual effect results from hydroxyproline's polar nature and its ability to polarize water molecules in its hydration shell, enhancing solubility and adaptability without compromising mechanical integrity.

As seen in ***Table 5***, the lower diffusion coefficient observed in proline-rich systems aligns with their lower MSD, indicating reduced global mobility and a more rigid overall structure. This suggests that proline contributes to tighter molecular packing or stronger internal cohesion, thereby limiting overall molecular movement and creating a more compact environment [173]. However, this increased rigidity does not necessarily imply greater internal structural stability. In contrast, hydroxyproline-rich systems, despite exhibiting higher diffusion coefficients and MSD due to enhanced solvent interactions, demonstrate stronger internal stability [174].

Table 5. The average diffusion coefficient (D) in the four systems: hydroxyproline-rich hexamer, proline-rich hexamer, hydroxyproline-rich heptamer, and proline-rich heptamer. is presented, along with the standard error (SE).

Systems	Diffusion Coefficient (D) (nm^2/s)	
	Avg	SE
hydroxyproline-rich hexamer	0.3	0.0
proline-rich hexamer	0.1	0.2
hydroxyproline-rich heptamer	0.2	0.1
proline-rich heptamer	0.1	0.1

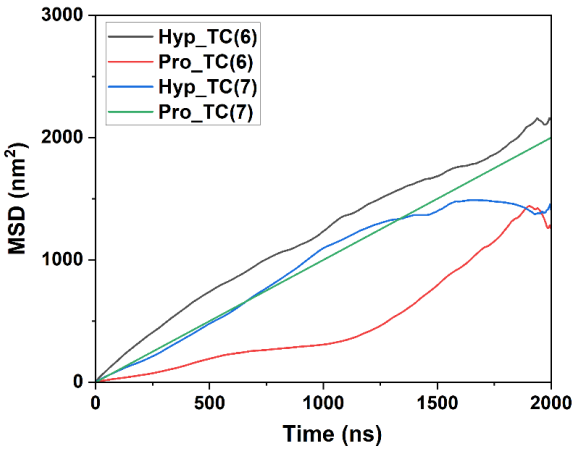

Figure 15. Average MSD for each of the four systems: hydroxyproline-rich hexamer (Hyp_TC(6)), proline-rich hexamer (Pro_TC(6)), hydroxyproline-rich heptamer (Hyp_TC(7)), and proline-rich heptamer (Pro_TC(7)).

To evaluate whether the tropocollagen strands experience vertical (Z-axis) sliding during the simulation, we calculated the MSD of each strand along the Z-axis. ***Table 6*** presents the average MSD for each system over the 2 μs simulations. It shows that inter-strand hydrogen bonding correlates with the MSD values. In both the hexamer and heptamer, the hydroxyproline-rich systems formed more hydrogen bonds and had lower MSD values than the respective Pro-rich systems.

Together, these results reveal a dual effect: hydroxyproline increases hydration and global motion while stabilizing the triple helix structure more effectively than proline, highlighting the complex balance between dynamics and structural integrity in collagen-like systems. Previous experimental studies have shown that flexible regions of collagen are more hydrophilic than rigid regions, potentially enhancing cell attachment and nutrient exchange. This increased hydrophilicity also aids adaptation to irregular bone defect shapes, helping maintain space for bone regeneration [175]. Conversely, rigid domains in collagen play a critical role in mechanical reinforcement. This indicates that the increase in stress with strain results from the initiation of stretching in these rigid regions of collagen molecules. This suggests that while flexible regions initially store energy, the rigid regions help the tendon resist further deformation at higher strains [176].

Table 6. Average mean-squared displacement and average number of intermolecular hydrogen bonds between tropocollagen strands in each of the four systems.

Tropocollagen Systems	MSD (nm^2)	Intermolecular Hydrogen Bonds
hydroxyproline-rich hexamer	320.5	3.8
proline-rich hexamer	333.4	1.9
hydroxyproline-rich heptamer	208.4	3.4
proline-rich heptamer	337.9	0.0

2.3.6 Interaction Energies

The interactions among contacts were examined in the four systems: hydroxyproline-rich hexamer, proline-rich hexamer, hydroxyproline-rich heptamer, and proline-rich heptamer to determine if they were driven by electrostatic or Lennard-Jones (LJ) interactions. Although PME handles long-range Coulombic interactions computationally, this study did not specifically investigate the role of electrostatic ordering over larger distances, such as collective dipole alignment. ***Table 7*** shows the total interaction energies, including the average Coulombic and Lennard-Jones energies for each system and for each tropocollagen. The total interaction energy was higher in hexamer systems compared to heptamer systems. This difference can be attributed to the distinct structural features of hexamers and heptamers, which significantly affect their interaction energies through variations in packing efficiency, hydrogen bonding, and overall stability. Hexamers, comprising six units, can achieve a more compact, optimal packing arrangement than heptamers, which consist of seven units. This efficient packing in hexamers allows closer intermolecular interactions, resulting in reduced inter-unit distances and enhanced attractive forces [177], ultimately leading to higher

interaction energies. Conversely, an additional unit in heptamers can introduce steric hindrance, disrupting optimal arrangements and weakening interactions.

Table 7. The total interaction energies, including the average Coulombic and Lennard-Jones energies in the four systems: hydroxyproline-rich hexamer, proline-rich hexamer, hydroxyproline-rich heptamer, and proline-rich heptamer, as well as for each tropocollagen, are presented. The standard error (SE) indicates the variability in measurements for each tropocollagen.

Tropocollagen Systems	Interaction Energy (kJ·mol^{-1})							
	Coulombic			LJ			Total	
	Avg	SE	Avg/TC	Avg	SE	Avg/TC	Sum	Sum/TC
hydroxyproline-rich hexamer	-10865.7	3.7	-1811	-793.7	9.5	-132.2	-11659.4	-1943.2
proline-rich hexamer	-10281.6	13.3	-1713.6	-771.2	9.3	-128.5	-11052.8	-1842.1
hydroxyproline-rich heptamer	-9853.9	3.3	-1407.7	-737.4	8.7	-105.3	-10591.3	-1513
proline-rich heptamer	-8688.7	3.4	-1241.2	-686.8	8.5	-98.1	-9375.5	-1339.3

Figure 16 shows that Coulombic (electrostatic) interactions are the dominant contributors to the total interaction energy in all four tropocollagen systems, accounting for approximately 90% of the total. This effect is particularly pronounced in the hydroxyproline-rich systems. The presence of the polar hydroxyl (-OH) group in hydroxyproline significantly enhances Coulombic stabilization by enabling extensive hydrogen bonding and polar interactions. Specifically, the -OH group of hydroxyproline forms a stronger hydrogen-bond network than that of standard proline [178]. In addition to forming direct interchain hydrogen bonds, the hydroxyl group also forms water bridges between adjacent peptide chains. These interactions contribute substantially to the structural stability of the collagen triple helix, underscoring the critical role of hydroxyproline in maintaining collagen integrity [179]. In contrast to the dominant electrostatic interactions, Lennard-Jones (LJ) interactions representing van der Waals and hydrophobic forces contribute a smaller fraction (~7–10%) of the total interaction energy in the four tropocollagen systems. These nonpolar interactions support close physical packing of the strands. Despite the presence of the polar hydroxyl group in hydroxyproline, the hydroxyproline-rich systems maintain strong LJ interactions, indicating that the added polarity does not significantly disrupt van der Waals compatibility [180].

These results underscore the importance of a delicate interplay between van der Waals forces and electrostatic interactions in stabilizing tropocollagen structures. While LJ interactions establish the foundational packing framework, the electrostatic forces, particularly those enhanced by hydroxyproline-mediated hydrogen bonding and water

bridging, provide additional stability and resilience to the structure. This balance between packing and polarity is essential for collagen's biological performance, enabling it to provide mechanical strength and elasticity to tissues.

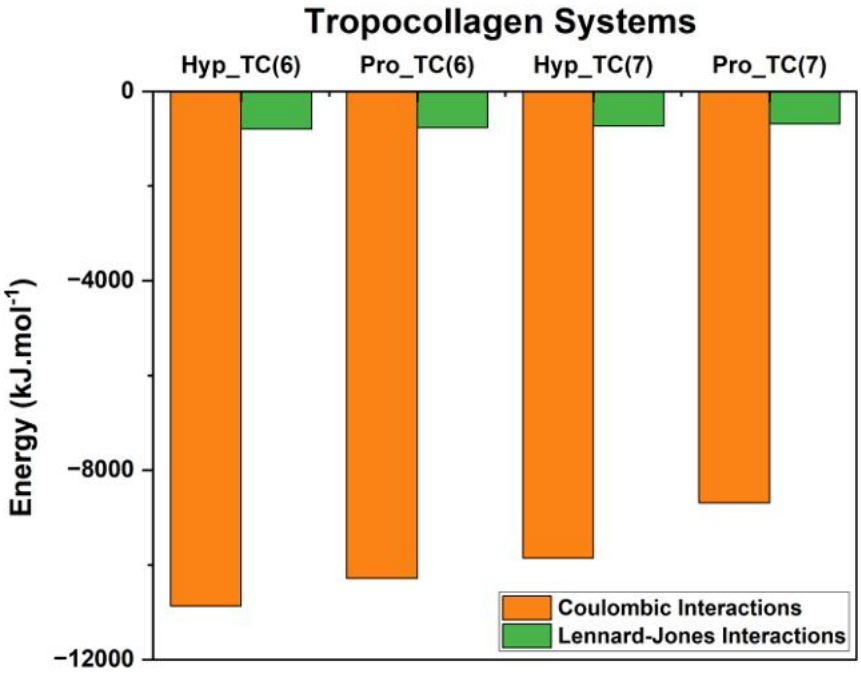

Figure 16. Average interaction energies, including Coulombic and Lennard-Jones energies in the four systems: hydroxyproline-rich hexamer (Hyp_TC(6)), proline-rich hexamer (Pro_TC(6)), hydroxyproline-rich heptamer (Hyp_TC(7)), and proline-rich heptamer (Pro_TC(7)).

2.3.7 Hyp and Pro-rich Tropocollagen are more Stable as a Hexamer than a Heptamer.

Both the heptamers and hexamers showed similar trends in the properties of the Hyp and Pro-enriched tropocollagens. This demonstrates that the effects of the Pro and Hyp residues are prevalent across multiple tropocollagen configurations. The aim of computing hexameric and heptameric Hyp and Pro-enriched tropocollagens is also to compare the relative stability of each configuration. To facilitate this comparison, the number of contacts, hydrogen bonds, and interaction energies were computed per tropocollagen strand, making the values of the two configurations comparable. Adding the tropocollagen strand to the Hyp and Pro-enriched system slightly increased the number of contacts per strand. It slightly decreased the number of hydrogen bonds per strand in the case of Pro, whereas it remained constant in Hyp. Most tellingly, the total interaction energy per strand decreased from -1943.2 to -1513 $kJ \cdot mol^{-1}$ by adding a tropocollagen strand to the Hyp-enriched system and from -1842.1 to -1339.3 $kJ \cdot mol^{-1}$ when adding a tropocollagen strand to the Pro-rich system. With stronger per-strand interactions in the hexamer, the hexameric form seems more stable in both the Hyp and

Pro-enriched systems. The difference between them is minor. Both cases support the stability of the Hyp-rich system and the flexibility of the Pro-rich system. A higher hydroxyproline content enhances the thermal stability of collagen by reinforcing intermolecular hydrogen bonds, which take more energy to break, making the structure more resistant to heat-induced denaturation. Flexibility, however, is vital for enabling movement and providing dynamic mechanical support to joints. Without it, the skeletal system would become too rigid, severely limiting mobility. Tendons, for instance, achieve their flexibility through a unique collagen cross-linking profile that includes a higher frequency of small-diameter fibrils. This organization allows interfibrillar sliding, facilitating elongation during skeletal development and improving the tissue's overall adaptability and resilience.

This comparative analysis examines how variations in tropocollagen size and composition affect the dynamic characteristics of collagen fibrils. The observed patterns across different hexameric and heptameric configurations reveal a fascinating aspect of tropocollagen assembly: its highly modular nature. This modularity allows tropocollagen strands to flexibly adjust their interactions, seamlessly accommodating different structural configurations and adapting to fulfill various biological functions. Such adaptability underscores the intricate versatility of collagen in maintaining tissue integrity and functionality.

2.4 Conclusions

This study provides in-depth insights into the molecular behaviors of hydroxyproline-rich and proline-rich tropocollagen in hexameric and heptameric configurations. The findings highlight crucial factors that influence collagen's stability and functionality, focusing on the effects of amino acid composition and strand arrangement. Hexameric structures exhibit exceptional packing efficiency, resulting in stronger intermolecular interactions and greater stability. In contrast, heptameric structures, while less efficient in packing, offer distinct advantages, such as increased solvent accessibility and a larger hydrophilic surface area, which improve their interactions with the surrounding environment. The study also highlights the distinct roles of hydroxyproline and proline: hydroxyproline enhances intermolecular hydrogen bonding and contributes to local structural rigidity. In contrast, proline increases residue-level flexibility but reduces overall molecular mobility. These insights advance our understanding of collagen’s hierarchical organization, molecular stability, and interactions. Furthermore, this study lays a foundational framework for experimental efforts to design synthetic collagen that mimics the structural and functional properties of its natural

counterpart. By understanding these principles, researchers can develop materials tailored to specific applications.

Chapter 3: Solution Properties in Electrospinning: Insights from Molecular Modeling and Experiments.

3.1 Summary

This chapter combines electrospinning experiments with molecular dynamics simulations to identify molecular factors that affect the electrospinning of polyvinyl alcohol, a synthetic polymer, as well as chitosan and collagen, natural polymers. The experimental part focuses on electrospinning solutions of these three polymers to assess nanofiber formation and morphology. Simultaneously, molecular dynamics simulations examine the solubility and structural properties of PVA, chitosan, and collagen molecules in water. These simulations analyze key polymer–solvent interactions, including hydrogen bonding, solvation behavior, and intra- and inter-chain interactions, that determine solution homogeneity and electrospinnability.

3.2 Materials and Methods

3.2.1 Experimental

3.2.1.1 Materials

High molecular weight chitosan (M_W = 310-375 kDa; degree of deacetylation (DD) >75%) and collagen from bovine achilles tendon (M_W = 300 kDa) were purchased from Sigma-Aldrich (Merck Life Science Kft, Budapest, Hungary). Glacial acetic acid (99.5%) and hydrochloric acid (35%) were supplied by Sigma-Aldrich. Polyvinyl alcohol (PVA) ($M_W \approx$ 72 kDa) was purchased from BioChemica (Dublin, Ireland). All chemicals received were used without further purification.

3.2.1.2 Preparation of Electrospinning Solutions

A 10% (w/v) polyvinyl alcohol solution was prepared by dissolving 5 g of PVA powder in 50 mL of demineralized water. The mixture was heated to 80-90 °C and stirred continuously with a magnetic stirrer at 600 rpm for 2 hours to obtain a homogeneous solution.

To make the chitosan solution, 0.1 g of chitosan powder was dissolved in 50 mL of demineralized water containing 0.1 M acetic acid. The solution was stirred continuously with a magnetic stirrer at 40-50 °C for 24 hours until the chitosan was fully dissolved.

The method described by Yang et *al*. [181] was used for dissolving type I collagen, which was extracted from bovine achilles tendon. A 0.1% collagen solution was prepared by

dissolving 50 mg of collagen powder in 50 mL of demineralized water containing 0.01 M hydrochloric acid (HCl). The solution was stirred overnight using a magnetic stirrer in a refrigerator at 3°C. The resulting solution appeared transparent, with a few small particles present and relatively low viscosity.

3.2.1.3 Electrospinning Procedure

The electrospinning experiments were performed using a custom-made, single-capillary system. A 10 mL syringe was used to deliver the polymer solution to a needle through a silicone rubber tube. The syringe was managed and connected to a syringe pump (Aitecs SEP-10S, Vilnius, Lithuania). The needle's tip was securely fastened with a steel bolt. After placing the syringe in the pump, the bolt touching the needle was connected to the positive terminal of the power supply (MA2000 NT 65/P, Nagykanizsa, Hungary) via a high-voltage cable. The electrospun fiber was placed on a grounded metallic collector and covered with aluminum foil taped to the collector for easier handling and sample storage. Each sample was electrospun continuously for 1 hour. The process was carried out under controlled conditions at 25.0 ± 2 °C and 34 ± 2% relative humidity. The technical parameters, such as needle gauge (G), flow rate (mL/h), applied voltage (kV), and the distance between the needle and collector (cm), were kept constant for the respective PVA, chitosan, and collagen solutions, as detailed in ***Table 8***.

Table 8. The technical parameters, including needle diameter Gauge (G), flow rate (mL/h), voltage (kV), and needle-collector distance (cm), were used to prepare nanofiber mats for PVA, chitosan, and collagen solutions.

Sample	Needle Gauge (G)	Flow Rate (mL/h)	Voltage (kV)	Needle-Collector Distance (cm)
PVA	25	0.7	27	20
Chitosan	20	0.5	27	21
Collagen	25	0.3	25	24

3.2.1.4 Characterization of Electrospun Nanofibers

The surface morphology of the nanofiber mats was investigated with a scanning electron microscope (SEM) (JEOL 6380 LA, Japan). Before the SEM examination, the nanofiber samples were sputter-coated with a gold-palladium (Au-Pd) alloy for 30 s. The nanofiber diameters were measured in ImageJ by randomly selecting 100 nanofibers from the SEM images.

3.2.2 Molecular Modeling

3.2.2.1 Simulation Systems

This study employed molecular dynamics simulations to investigate the structural properties of PVA, chitosan, and collagen. A 2.5% (w/v) solution was prepared for each

material in water, with each containing 30 repeating units per polymer chain. In the experiments, polymer concentrations were determined by solubility limits and electrospinning requirements (10% PVA, 0.2% chitosan, 0.1% collagen), whereas in simulations, a standard intermediate concentration (2.5% w/v) was used to ensure computational feasibility and allow meaningful comparisons across systems. The MD results were not intended to precisely match the experimental concentrations but to provide molecular-level insights into solubility and chain interactions that explain the observed electrospinning behavior. No ions were added to the PVA and collagen systems because these materials were electrically neutral. This choice allowed us to concentrate on their natural structure and behavior in water without interference from additional ions. However, 180 chloride (Cl^-) ions were included in the chitosan system to balance the positive charge from the protonated amino groups on the chitosan chains. This created an electrically balanced system, providing a more realistic representation of chitosan. The simulations were performed in a cubic box, and the molecular composition of the three systems is detailed in ***Table 9.***

Table 9. The molecular composition of the three systems (PVA, chitosan, and collagen) includes the number of polymer chains, the total number of atoms, water molecules, ions (if applicable), the size of the simulation box $(nm)^3$, and the concentration (w/v%).

Systems	Number of				Box Size $(nm)^3$
	Chains	Atoms	Water Molecules	Cl^- Ions	
2.5% (w/v) PVA	16	3392	46900	-	$(11.24)^3$
2.5% (w/v) Chitosan	6	4158	70620	180	$(12.86)^3$
2.5% (w/v) Collagen	4	4388	78900	-	$(13.36)^3$

3.2.2.2 Model Systems

A model of PVA consisting of repeating units of (–CH_2–CHOH–) was created. The Polymer Builder tool available in CHARMM-GUI was used to generate this structure. In addition, poly-*D*-glucosamine was employed to replicate the chitosan structure, as it represents the deacetylated form of chitin and distinguishes it from *N*-acetyl-D-glucosamine, which retains the acetyl groups found in chitin. This choice aligns with the characteristics of Sigma-Aldrich product 419419, which was crucial to our experimental procedures. The Glycan Reader & Modeler tool in CHARMM-GUI was used to construct this model [182]. Furthermore, our study used the crystal structure of a triple-helical collagen-like peptide model (PDB ID: 1QSU) consisting of $(Pro\text{-}Hyp\text{-}Gly)_4$-Glu-Lys-Gly-$(Pro\text{-}Hyp\text{-}Gly)_5$, obtained from the RCSB Protein Data Bank [151]. The structures of PVA, chitosan, and collagen are illustrated in ***Figure 17***.

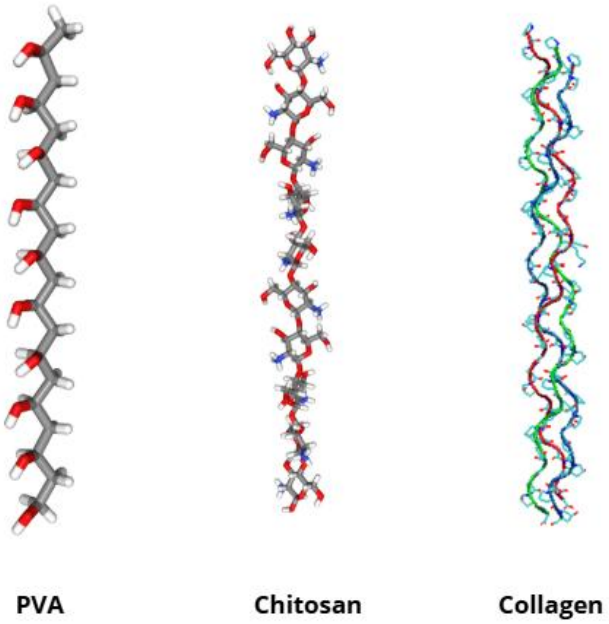

Figure 17. Molecular structures of the polymers used in this study: PVA, chitosan, and collagen. The repeating unit of PVA is (–CH_2–CHOH–), while chitosan consists of β-(1→4)-linked D-glucosamine units. Collagen is modeled as a peptide with the repeating tripeptide unit (Gly–Xxx–Yyy), where Xxx and Yyy are predominantly proline (Pro) and hydroxyproline (Hyp).

3.2.2.3 Simulation Protocol

The simulations were conducted using the GROMACS 2021 software package [143]. The force field parameters for all molecules used in this study are compatible with the CHARMM36m force field [183]. The TIP3P model was utilized for water [138]. Energy minimization was performed for all systems using the steepest-descent method for 50,000 steps to address any bad contacts. Following this minimization, equilibration was performed under the canonical (NVT) ensemble at 300 K for 5 ns. During this phase, the LINCS algorithm constrained all bond lengths involving hydrogen atoms, applying a time step of 2 fs. The temperature throughout the simulation was regulated by the Nosé-Hoover thermostat, with the polymer and solvent controlled independently. Initial velocities were generated at 300 K based on a Maxwell–Boltzmann distribution. The systems then entered a second equilibration stage under the isothermal-isobaric (NPT) ensemble for 5 ns, during which bonds remained constrained. The Parrinello-Rahman barostat was implemented to maintain a constant pressure of 1 bar while isotropically scaling the box volume. This included a pressure coupling relaxation time of 5 ps and a compressibility of 4.5e-5 bar^{-1}. Non-bonded atom pairs were updated every 20 simulation steps, and the Lennard-Jones interactions were cut off at 1.2 nm. The Verlet cutoff scheme was employed for neighbor searching. Periodic boundary conditions were enforced in all dimensions (xyz). The electrostatic interactions were evaluated using the Particle-Mesh Ewald summation with a real-space cutoff of 1.2 nm.

3.2.2.4 Analysis

Each system was simulated for 500 ns, and the data from each 500 ns period were used for the analysis. All analysis programs mentioned in this section are part of the standard release of the GROMACS 2021 program package. The *gmx polystat* program analyzes the static properties of polymers in molecular simulations. It calculates important metrics, such as the average end-to-end distance and the radius of gyration of polymer chains. This provides insights into their structural characteristics and conformational changes over time. With option -p , the persistence length is determined. The *gmx sasa* program calculated the solvent-accessible surface area (SASA), and the analysis categorized atoms into two groups: "Hydrophobic" and "Hydrophilic". The *gmx hbond* program calculates hydrogen bonds. The *gmx energy* program calculated the Coulombic and Lennard-Jones interaction enthalpies for each system. The *gmx density* tool computes and visualizes the molecular density distribution across the simulation box.

3.3 Results and Discussion

3.3.1 Experimental

3.3.1.1 Morphological Analysis Using Scanning Electron Microscopy (SEM)

The SEM images in ***Figure 18*** showed that the PVA fibers are smooth and uniform in diameter, averaging 233.9 nm (***Table 10)***. This uniformity indicates sufficient chain entanglement within the polymers in solution, effectively preventing bead formation during jet formation. These features characterize the high quality and consistency of the electrospun PVA nanofibers, as noted by Shalihah et *al*. [184]. The concentration of the PVA solution significantly influences viscosity and conductivity during electrospinning. A higher PVA concentration promotes uniform fiber formation by increasing solution viscosity, thereby facilitating adequate entanglement of polymer chains and reducing bead formation in nanofibers [185].

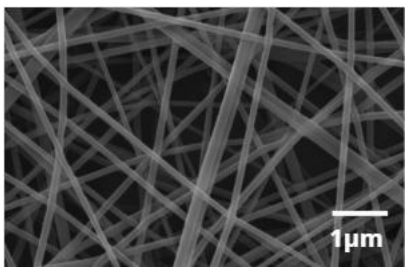

Figure 18. SEM images showing the surface morphology of nanofibers formed from pure PVA.

Efforts to produce nanofibers from chitosan solutions have encountered significant challenges. Of the conditions tested, only the concentration specified in the method section was chosen, even though the chitosan was not fully dissolved. This concentration was chosen because other formulations performed worse and were completely unsuitable for electrospinning. Repeated attempts to increase chitosan concentration, add more acetic acid, or use alternative solvents did not improve spinnability; instead, they led to incomplete dissolution, high viscosity, or unstable solutions, thereby preventing fiber formation. When dissolved in acetic acid, chitosan becomes protonated, resulting in strong charge repulsion along the polymer chains that promotes chain elongation. However, the highly polar and ionic nature of pure chitosan also increases the solution's surface tension, hindering the electrospinning jet from stretching into fine fibers. As a result, pure chitosan solutions tend to form spherical droplets to minimize surface energy rather than producing continuous nanofibers [186]. Collagen, like chitosan, also poses challenges for electrospinning due to its poor solubility and limited chain entanglement. However, unlike chitosan, which has high surface tension due to protonation, collagen solutions maintain low viscosity even at high concentrations, presenting a different challenge. Electrospinning collagen from the bovine Achilles tendon source is particularly difficult due to its low solubility, which obstructs the formation of stable electrospun mats. Others note that collagen's triple-helical structure is sensitive to solvents, leading to degradation during electrospinning [187].

Table 10. Average nanofiber diameters with standard errors (SE) for the PVA samples.

Sample	Volume (mL)	Average Diameter of Nanofibers (nm)	SE (nm)
PVA	30	233.9	1.1
Chitosan	30	-	-
Collagen	30	-	-

3.3.2 Molecular Modeling

3.3.2.1 The Structural Properties of PVA, Chitosan, and Collagen.

Table 11 summarizes the morphological properties of PVA, chitosan, and collagen, including end-to-end distance, radius of gyration, persistence length, aspect ratio, and anisotropy. These properties reflect the polymers' flexibility, compactness, and conformational behavior.

The PVA system exhibited the shortest average end-to-end distance of 2.2 nm and the smallest radius of gyration at 0.9 nm compared to chitosan and collagen, indicating the most compact and tightly coiled polymer structure. A related study demonstrated that the PVA chains are not extended but remain compact and tightly coiled. This compactness reveals that

the chains are closely packed [188]. Another important property of PVA is its persistence length of 2.7 nm, close to the end-to-end distance, indicating its rigidity and ability to maintain its shape. This is an important feature in electrospinning, where the jet stability depends on the polymer's ability to resist deformation under an applied electric field. Furthermore, PVA exhibits isotropic segmental motion (***Table 11***), as indicated by its extremely low anisotropy value of 0.1. Others have shown that PVA's chains undergo uniform movement in aqueous solution. This effect reduces chain constraints and enhances flexibility, which is crucial for electrospinning, as polymer dynamics significantly impact the final material properties [189].

Table 11. The structural properties of PVA, chitosan, and collagen, including end-to-end distance, radius of gyration, persistence length, aspect ratio, and anisotropy, along with their respective standard errors (SE).

Systems	End-to-End Distance (nm)		Radius of Gyration (nm)		Persistence Length (nm)		Aspect Ratio	Anisotropy
	Avg	SE	Avg	SE	Avg	SE		
PVA	2.2	0.01	0.9	0	2.7	0.1	2.4	0.1
Chitosan	13.2	0.02	4.1	0	0.8	0	3.2	0.05
Collagen	5.0	0.01	1.7	0	2.4	0.2	2.9	0.1

In contrast, the chitosan system exhibited an average end-to-end distance of 13.2 nm and a radius of gyration of 4.1 nm, indicating an extended and flexible configuration. This is in agreement with the findings of Shariatinia et *al*. [190], the significant end-to-end distance of the chitosan system suggests that the polymer chains are more stretched than coiled. This extended configuration reflects the polymer's capacity to adjust its conformation in response to solvent interactions and electrostatic repulsion, promoting a more elongated structure in solution. The persistence length of chitosan is 0.8 nm, indicating that it is highly flexible. The flexibility of chitosan is significantly influenced by the glycosidic linkages between its sugar units. These linkages can adopt different conformations, allowing for more chain bending and flexibility [191]. Chitosan has an aspect ratio of 3.2, indicating that it adopts an elongated conformation in solution. Its low isotropy value of 0.05 suggests that this extended shape is consistent across orientations, reflecting a stable, uniform molecular configuration.

In comparison, the collagen system showed an average end-to-end distance of 5.0 nm and a radius of gyration of 1.7 nm, indicating a semi-extended conformation rather than a tightly packed structure. Collagen is semi-flexible, and this characteristic varies among different types, sources, and environmental conditions, affecting its structural properties and hydration behavior [192]. The persistence length of collagen (2.4 nm) suggests that it is more rigid than chitosan but less stiff than PVA. This intermediate flexibility allows collagen to adopt extended yet adaptable conformations, which is important for its biological role in

providing structural support while maintaining elasticity. Unlike highly flexible polymers, collagen maintains an extended conformation with limited bending, preserving its overall molecular shape while allowing for some conformational adaptability in response to environmental forces. The aspect ratio of collagen (2.9) contributes to fiber alignment and organization, optimizing its ability to form strong, stable fibrillar structures. Additionally, collagen exhibits isotropic properties; however, it may exhibit slight directional dependence due to molecular alignment [193].

3.3.2.2 Total, Hydrophobic, and Hydrophilic Solvent-Accessible Surface Area (SASA)

The Solvent Accessible Surface Area (SASA) analysis is crucial for understanding the interactions of molecules such as PVA, chitosan, and collagen with water, particularly for distinguishing their hydrophobic and hydrophilic regions. This is vital for electrospinning solutions, as it influences the molecular interactions between the polymer and solvent, affecting solubility and electrospinnability. PVA's solvent-accessible surface area shows a nearly balanced hydrophilic-hydrophobic ratio (54.2% hydrophilic vs. 45.8% hydrophobic), as indicated in ***Table 12***, making it highly water-compatible. This water solubility is mainly driven by the abundance of hydroxyl (-OH) groups, which enhance water absorption and retention. As the concentration of PVA increases, these hydroxyl groups promote strong hydrogen bonding, further reinforcing the polymer's hydrophilic nature [194]. The high hydrophilic SASA of PVA correlates with strong polymer-water interactions, as confirmed by hydrogen bond analysis. This hydrophilicity is crucial in electrospinning, as it ensures that the polymer forms a homogeneous, stable solution that can be efficiently processed into nanofibers.

Table 12. The average SASA values in nm^2 for the total surface in three systems (PVA, chitosan, and collagen) are categorized by hydrophobic and hydrophilic regions. Includes percentages of hydrophobic and hydrophilic areas. The standard error (SE) is included to indicate the variability in the measurements.

Systems	Solvent Accessible Surface Area (SASA) (nm^2)							
	Total		Hydrophobic			Hydrophilic		
	Avg	SE	Avg	SE	%	Avg	SE	%
PVA	262.5	0.1	120.2	0.1	45.8%	142.3	0.1	54.2%
Chitosan	345.5	0.0	136.1	0.0	39.4%	209.3	0.0	60.6%
Collagen	213.1	0.1	137.2	0.1	64.4%	75.9	0.0	35.6%

Chitosan, with a hydrophilic solvent-accessible surface area (SASA) ratio of 60.6%, shows a strong affinity for water. This hydrophilicity is mainly due to its amino ($-NH_2$) and hydroxyl (-OH) functional groups, which form hydrogen bonds with surrounding water molecules, as evidenced by its high average polymer–water hydrogen-bonding (940.2 bonds). This strong interaction enhances chitosan's water absorption capacity, making it highly

suitable for biomedical applications, such as wound dressings, where moisture retention and biocompatibility are crucial. Additionally, chitosan's solubility and flexibility are closely related to its degree of acetylation (DA): lower DA (more deacetylated) chitosan chains are more flexible and soluble because of increased hydrogen bonding potential, while highly acetylated forms tend to cluster into rigid structures with decreased solubility [128]. These variations directly influence its processing behavior, particularly in aqueous systems and formulations for electrospinning and drug delivery.

Collagen has a high hydrophobic solvent-accessible surface area ratio of 64.4%, indicating its limited interaction with water. This is primarily due to its triple-helix structure, where nonpolar proline and hydroxyproline residues are oriented outward. In contrast, residues without hydrophobic side chains, such as glycine, are buried within the core. This structural configuration not only stabilizes the helix but also encourages aggregation into dense, self-assembled fibrils. Although collagen contains hydrophilic amino acids, the relatively low hydrophilic SASA (35.6%) and fewer polymer–water hydrogen bonds (totaling 687.6) imply restricted water accessibility. These characteristics contribute to collagen's low solubility and minimal swelling behavior compared to more hydrophilic polymers, such as PVA and chitosan. Consequently, collagen maintains high structural integrity, making it suitable for tissue-supporting functions; however, it is more difficult to process in aqueous applications, such as electrospinning, unless modified or blended with more hydrophilic polymers.

3.3.2.3 Hydrogen Bonds

***Table* 13** presents the hydrogen bonding characteristics of PVA, chitosan, and collagen. It details the interactions between polymer chains (polymer-polymer) and between the polymer and water (polymer-water), as well as the total number of hydrogen bonds. PVA does not form significant interchain hydrogen bonds; it has 3.8 hydrogen bonds per chain. This disruption occurs because water interferes with polymer-polymer interactions. Water molecules compete with PVA chains for hydrogen-bonding sites, thereby weakening intermolecular interactions and preventing the formation of stable inter-chain hydrogen bonds [195]. Furthermore, PVA compensates for its weak inter-chain bonding by forming numerous hydrogen bonds with water, producing an average of 869.5 total polymer-water interactions. This strong affinity for water makes PVA ideally suited for applications that require a hydrated, gel-like state, thereby ensuring its stability and solution processability [196].

Chitosan exhibits more intra-chain hydrogen bonding than PVA, forming an average of 10.4 bonds per chain. These bonds are primarily of the O–H···O and N–H···O types, involving hydroxyl and amine groups located within the same monomer unit. With an average occupancy of 26.5% during the simulation, these interactions help stabilize the conformation of individual monomer units by limiting internal motion within the sugar rings, thereby supporting the polymer chain's cohesion and consistent organization in solution. Interestingly, chitosan doesn't form significant inter-chain hydrogen bonds; it's stabilized by strong intramolecular hydrogen bonding, which links nitrogen atoms to adjacent ring oxygen atoms and hydroxymethyl groups. This internal stabilization prevents extensive interchain bonding [197], thereby differentiating it from other hydrogen-bonding polymers. However, chitosan exhibits a strong hydrogen-bonding interaction with water, forming approximately 940.2 polymer-water hydrogen bonds. Its polar amine ($-NH_2$) and hydroxyl (-OH) groups facilitate this strong interaction, which involves dipole-dipole interactions and hydrogen bonding with water molecules [198]. Despite chitosan's capacity to form hydrogen bonds, Ogawa et *al.* [199] found that chitosan's hydrogen bond strength is weaker than cellulose's. This is because chitosan's amino groups are less effective hydrogen-bond donors than the hydroxyl groups in cellulose, which act as both donors and acceptors. Consequently, these weaker hydrogen bonds contribute to chitosan's lower water solubility.

Collagen exhibits a relatively high level of intra-chain hydrogen bonding, with an average of 17.3 hydrogen bonds per chain and an average occupancy of 30.4% observed during the simulation. These interactions primarily involve backbone functional groups, such as amine (–NH) and carbonyl (C=O) groups, as well as side-chain carboxylate and hydroxyl groups. The presence of these hydrogen bonds contributes to local conformational stability by reinforcing specific regions of each chain and supporting its organized structure. Beyond intra-chain interactions, collagen also forms inter-chain hydrogen bonds between adjacent chains, with an average occupancy of 85.5% observed during the simulation. These intermolecular interactions occur predominantly between backbone amide and carbonyl groups, as well as between polar side chains. By reinforcing lateral associations between chains, these hydrogen bonds enhance the alignment and cohesion of collagen fibrils, playing a crucial role in stabilizing its triple-helical architecture [200]. In addition to intra- and inter-chain hydrogen bonding, collagen forms approximately 687.6 hydrogen bonds with surrounding water molecules, highlighting its affinity for hydration. These hydrogen bonds are primarily formed between polar functional groups on the collagen surface, such as amine,

carbonyl, and hydroxyl groups, and water molecules. Some water molecules are tightly associated with the polymer, contributing to local conformational stability, while others remain more loosely bound and mobile. This dynamic hydration shell facilitates molecular flexibility and solvent interaction, influencing collagen's behavior in aqueous environments. The balance between bound and free water is critical for maintaining collagen's hydrated state, which is essential for its function and stability in biological and biomedical applications [201].

Table 13. Hydrogen bonding characteristics in PVA, chitosan, and collagen are categorized into polymer–polymer and polymer–water interactions. Values are reported as averages per chain, between chains, and total counts across each system. Standard error (SE) values are included to reflect measurement variability.

Systems	Hydrogen Bonds									
	Polymer-Polymer					Polymer-Water			Total	
	Between Chains		Within Chains		Total	Per Chain		Total	Per Chain	Total
	Avg	SE	Avg	SE		Avg	SE			
PVA (16 Chains)	0.1	0.0	3.8	0.1	61.6	54.3	0.1	869.5	58.1	931.1
Chitosan (6 Chains)	0.0	0.0	10.4	0.1	62.5	156.7	0.1	940.2	167.1	1002.7
Collagen (4 Chains)	2.0	0.7	17.3	1.3	79.6	171.9	2.0	687.6	189.2	767.2

3.3.2.4 Interaction Enthalpies

The intra- and inter-chain interaction enthalpies, as well as solution (polymer-water) interaction enthalpies, for PVA, chitosan, and collagen were studied to understand how these interactions shape the properties of polymers in solution. ***Table 14*** compares the intra-chain interaction enthalpies of PVA, chitosan, and collagen by separating contributions from Coulombic and Lennard-Jones (LJ) interactions. PVA exhibits the lowest overall intra-chain interaction enthalpies, with Coulombic enthalpy contributing only 6.4% and LJ interactions contributing –2.3% of the total, indicating minimal electrostatic and van der Waals forces. This is primarily due to the dominance of hydrogen bonding with water rather than in PVA chains. As a result, PVA chains demonstrate low self-interaction and are highly mobile, enhancing their solubility and making them well-suited for processing applications such as film formation and electrospinning. In contrast, chitosan and collagen exhibit significantly stronger intra-chain interactions, with Coulombic contributions of 94% and 93%, respectively. These high values result primarily from protonated amino groups in chitosan and charged amino acid residues, such as lysine, in collagen, both of which promote strong electrostatic stabilization. The LJ contributions, accounting for 6% of the total intra-chain interaction enthalpy in chitosan and 7% in collagen, represent short-range van der Waals interactions that,

although weaker than Coulombic forces, enhance molecular packing. In chitosan, van der Waals interactions between the sugar rings further support the formation of tightly packed, extended chains [202]. In collagen, LJ forces help maintain the triple helix's tight alignment, contributing to the fibrillar structure's overall compactness.

Table 14. The intra-chain interaction enthalpy for PVA, chitosan, and collagen comprises Coulombic and Lennard-Jones (LJ) interactions. The average (Avg), standard error (SE), average enthalpy per chain (Avg/C), total enthalpy (Sum), and total enthalpy per chain (Sum/C) are reported for each system.

Systems	Intra-Chain Interaction Enthalpy (kJ·mol^{-1})							
	Coulombic			LJ			Total	
	Avg	SE	Avg/C	Avg	SE	Avg/C	Sum	Sum/C
PVA	4.3×10^{3}	0.4	2.7×10^{2}	-9.8×10^{1}	0.3	-6.1	4.2×10^{3}	2.6×10^{2}
Chitosan	-1.4×10^{4}	0.6	-2.4×10^{3}	-3.7×10^{2}	0.2	-62.5	-1.4×10^{4}	-2.4×10^{3}
Collagen	-2.1×10^{4}	11.4	-5.2×10^{3}	-1.2×10^{3}	7.6	-300.3	-2.2×10^{4}	-5.5×10^{3}

As shown in ***Table 15***, PVA shows weak inter-chain interactions, with a total enthalpy of -3.4 kJ·mol^{-1}. Only small contributions come from Coulombic (1.6%) and Lennard-Jones (1.4%) interactions, reflecting the polymer's hydrophilic nature. PVA contains numerous hydroxyl groups that prefer to form hydrogen bonds with surrounding water molecules rather than other PVA chains. This limited polymer–polymer interaction explains PVA's excellent dispersion and solubility in aqueous environments. Chitosan, in contrast, displays no measurable inter-chain interaction enthalpy in this analysis; neither Coulombic nor van der Waals contributions are present. This indicates that chitosan chains do not interact significantly with one another, and that stabilization primarily occurs through strong intra-chain forces. These forces include hydrogen bonding and electrostatic interactions within the polymer backbone, which contribute to its rigid structure and poor solubility, particularly under neutral conditions.

Table 15. The inter-chain interaction enthalpy for PVA, chitosan, and collagen comprises Coulombic and Lennard-Jones (LJ) interactions. The average (Avg), standard error (SE), average enthalpy per chain (Avg/C), total enthalpy (Sum), and total enthalpy per chain (Sum/C) are reported for each system.

Systems	Inter-Chain Interaction Enthalpy (kJ·mol^{-1})							
	Coulombic			LJ			Total	
	Avg	SE	Avg/C	Avg	SE	Avg/C	Sum	Sum/C
PVA	-1.8	0.2	-0.1	-1.6	0.2	-0.1	-3.4	-19.2
Chitosan	0.0	0.0	0.0	0.0	0.0	0.0	0.0	0.0
Collagen	-231.1	6.5	-57.7	-211.3	6.9	-52.8	-442.4	-110.6

Collagen exhibits the highest inter-chain interaction enthalpy among the studied polymers, totaling –442.4 kJ·mol^{-1}. Coulombic interactions contribute about 52%, while LJ interactions account for approximately 48%, indicating strong and balanced electrostatic and van der Waals forces between collagen molecules. These interactions are consistent with collagen's natural tendency to form compact, fibrous aggregates in solution. They also explain

its partial insolubility: only a fraction of collagen dissociates into soluble units, while the rest remains stable in fibrillar form [203].

Table 16 presents the interaction enthalpies between each polymer and solvent, offering insight into their hydration behavior and solubility. For PVA, the Coulombic interaction enthalpy with water is – 2.07×10^{6} kJ·mol^{-1}, reflecting strong electrostatic interactions. This high value is attributed to the formation of numerous hydrogen bonds with surrounding water molecules. These interactions facilitate excellent hydration, promote isotropic segmental motion, and allow uniform chain dispersion. This behavior contributes to PVA's solubility, making it well-suited for hydrogels, coatings, and electrospinning applications. On the other hand, chitosan's interaction with water displays a strong Coulombic enthalpy of -3.39×10^{6} kJ·mol^{-1} (***Table 16***), indicating significant electrostatic interactions between chitosan's polar functional groups (-NH_2, -OH) and water molecules. This interaction promotes extensive hydrogen bonding, improving chitosan's hydration and affecting its structural behavior in solution. However, the Lennard-Jones (LJ) enthalpy indicates that chitosan molecules aggregate in solution due to intra-hydrogen bonding. However, the hydration shell formed by water molecules hinders intramolecular hydrogen bonding, thereby reducing aggregation [131]. This interplay between hydration and self-association explains chitosan's limited solubility under neutral conditions. Collagen shows the strongest polymer–solvent Coulombic interaction among the polymers. However, despite this strong interaction with water, collagen does not fully dissolve. Instead, water hydrates the fibrillar structure without disrupting its organization, thereby maintaining mechanical stability. As a result, collagen typically exists in aqueous environments as a mixture of soluble and insoluble forms [125].

Table 16. Total interaction enthalpy for PVA, chitosan, and collagen in solution, including Coulombic and Lennard-Jones (LJ) interactions. The table presents the average (Avg), standard error (SE), and total enthalpy (Sum) for each system.

Systems	Total Interaction Enthalpy (kJ·mol^{-1}) for Polymer-Solvent				
	Coulombic		LJ		Total
	Avg	SE	Avg	SE	Sum
PVA	-2.07×10^{6}	0.3	2.07×10^{5}	0.2	-1.87×10^{6}
Chitosan	-3.39×10^{6}	0.4	3.17×10^{5}	0.3	-3.07×10^{6}
Collagen	-3.69×10^{6}	1.1	3.47×10^{5}	0.9	-3.34×10^{6}

3.3.2.5 Density

Calculating density in molecular dynamics simulations is essential for accurately modeling polymer behavior in solution, as it directly affects stability and fiber formation in electrospinning. The PVA system demonstrates a low average density at 1011.1 kg·m^{-3}, as

shown in ***Table 17***. This system also maintains remarkable consistency in density, with only minor fluctuations, indicating that MD simulations can reproduce experimentally determined values, as shown in ***Figure 19***. The interaction between PVA and water molecules helps maintain a density similar to that of water, as the polymer chains are well dispersed, allowing a uniform structure within the solution.

Table 17. Average bulk densities ($kg \cdot m^{-3}$) and standard errors for PVA, chitosan, and collagen systems.

Systems	Density ($kg \cdot m^{-3}$)	
	Avg	SE
PVA	1011.1	0.1
Chitosan	1018.2	0.1
Collagen	1012.1	0.2

The average collagen density was slightly higher at 1012.1 $kg \cdot m^{-3}$. ***Figure 19*** illustrates that the collagen system undergoes an initial decline in density, likely due to hydration-induced expansion and a temporary disruption of inter-chain hydrogen bonds. Following this, the relatively higher fluctuations in density suggest a dynamic competition between hydration effects and the self-association of collagen chains. The strong inter-chain interactions (as shown in ***Table 15***) indicate that collagen retains significant intermolecular cohesion. Additionally, high hydrogen bonding stabilizes the triple-helix conformation of collagen, reinforcing its structural integrity. These findings confirm that intermolecular bonding and helix stability influence fiber packing efficiency, directly impacting density and mechanical properties.

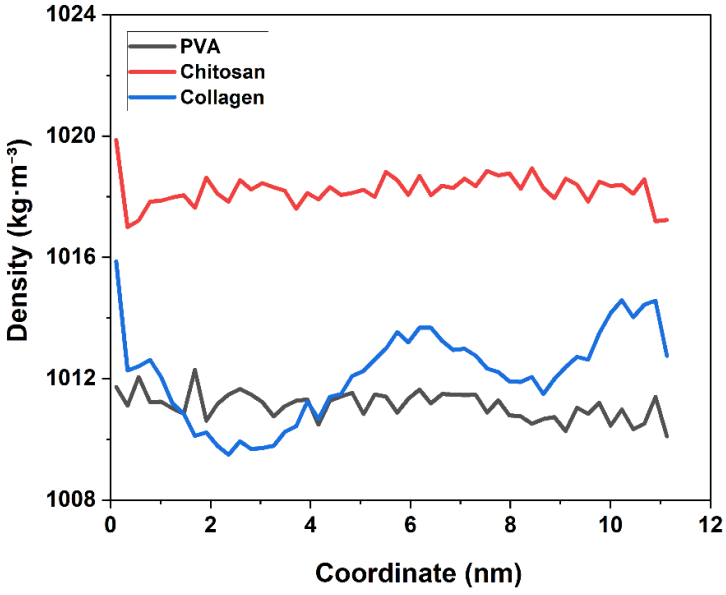

Figure 19. Density variations of PVA, chitosan, and collagen systems plotted as a function of the coordinate distance along the Z-axis (in nanometers).

In contrast, the chitosan system has the highest average density, at 1018.2 $kg \cdot m^{-3}$, with minor fluctuations. This result is due to strong intra-chain hydrogen bonding and electrostatic interactions, as confirmed by interaction enthalpy and hydrogen-bond analyses. Unlike PVA, which exhibits weak intra-chain interactions and greater molecular flexibility, chitosan's highly cohesive intra-chain interactions limit its solubility. The strong hydration shell formed by polymer-water hydrogen bonds further compacts chitosan molecules, restricting aggregation while maintaining a dense structure. According to Sigma-Aldrich, the reported density of chitosan is 1000 $kg \cdot m^{-3}$, which is within 2% of the computed value of 1018.2 $kg \cdot m^{-3}$, thereby confirming the accuracy of the simulation method. Compared to collagen, chitosan's dense molecular arrangement enhances its stability in solution, making it well-suited for applications that require structured hydrogels.

3.4 Conclusion

In the experimental section, this study examines the morphology of electrospun nanofibers. The results show that the synthetic polymer PVA readily forms uniform, bead-free nanofibers due to sufficient molecular entanglement and stable jet formation. In contrast, the natural polymers chitosan and collagen faced significant challenges and did not produce continuous fibers, highlighting the inherent differences in electrospinnability between synthetic and natural polymers.

Molecular dynamics (MD) simulations support experimental findings by providing a detailed molecular-level understanding of the solubility issues associated with chitosan and collagen. While both biopolymers contain functional groups capable of hydrogen bonding with water, their intrinsic molecular structures limit their solubility and processability. In chitosan, strong intra-chain hydrogen bonds and significant electrostatic interactions promote self-association, yielding viscous, heterogeneous solutions that are difficult to electrospin. Likewise, collagen's extensive network of inter- and intra-chain hydrogen bonds and its predominant hydrophobic interactions result in fibrillar aggregation and poor water solubility. These molecular insights align with experimental reports describing challenges in dissolving chitosan and collagen into uniform solutions, which hampers their use in electrospinning. As a result, they often require chemical modification or blending with more hydrophilic polymers to improve solubility, processability, and electrospinning suitability. In contrast, PVA offers highly favorable electrospinning characteristics, including excellent water compatibility, high chain flexibility, and strong polymer–solvent interactions. These properties enable it to

dissolve efficiently and form homogeneous, stable solutions, findings that support the experimental observations.

Chapter 4: Computational and Experimental Study of PVA-Biopolymer Blends.

4.1 Summary

In this chapter, a combined experimental and computational approach is employed, integrating electrospinning experiments with atomistic molecular dynamics simulations to systematically examine collagen–PVA and chitosan–PVA blends. The MD simulations provide insights into molecular interactions, hydrogen-bonding networks, and conformational changes induced by blending with PVA. Three blend ratios (1:1, 1:2, and 2:1) are analyzed for both collagen–PVA and chitosan–PVA systems to understand how composition influences solubility, spinnability, and structural integrity. This combined approach aims to identify optimal blending ratios that promote uniform molecular mixing and the production of high-quality nanofibers.

4.2 Materials and Methods

4.2.1 Experimental

4.2.1.1 Preparation of Electrospinning Solutions

We used the same materials as described in Section 3.2.1.1. The polyvinyl alcohol, chitosan, and collagen solutions were prepared separately, as presented in Section 3.2.1.2, before being combined. The PVA and chitosan solutions were mixed at room temperature at the following ratios of chitosan to polyvinyl alcohol: 1:1, 1:2, and 2:1. Next, the collagen and PVA solutions were combined in the ratios of collagen to polyvinyl alcohol (1:1, 1:2, and 2:1) and stirred for one hour. The performance of each solution was evaluated in subsequent electrospinning protocols.

4.2.1.2 Electrospinning Procedure

Electrospinning experiments were conducted using the same custom-built single-capillary setup described in Section 3.2.1.3. The technical parameters, such as needle gauge (G), flow rate (mL/h), applied voltage (kV), and the distance between the needle and collector (cm), were kept constant for the respective chitosan-PVA and collagen-PVA solutions, as detailed in ***Table 18***.

Table 18. The technical parameters used to prepare various nanofiber mats for chitosan-PVA and collagen-PVA solutions.

Sample	Needle Gauge (G)	Flow Rate (mL/h)	Voltage (kV)	Needle-Collector Distance (cm)
Chitosan-PVA	21	0.5	27	27
Collagen-PVA	25	0.2	25	24

4.2.1.3 Characterization of Electrospun Nanofibers

The surface morphology of the nanofiber mats was investigated with a scanning electron microscope (SEM) (JEOL 6380 LA, Japan).

4.2.2 Molecular Modeling

4.2.2.1 Simulation Systems

This study used molecular dynamics simulations to examine the structural properties of collagen-PVA and chitosan-PVA solutions. A 2.5% (w/v) solution was prepared for each material in water, with each containing 30 repeating units per polymer chain. No ions were added to the PVA and collagen systems because these materials were electrically neutral. However, chloride (Cl^-) ions were included in the chitosan system to balance the positive charge from the protonated amino groups on the chitosan chains. The simulations were performed in a cubic box, and the molecular composition of the systems is detailed in ***Table 19.***

Table 19. The molecular composition of the collagen-PVA and chitosan-PVA systems includes the mixing ratio, the number of polymer chains, the total number of atoms, water molecules, ions (if applicable), and the simulation box size $(nm)^3$.

Systems	Mixing Ratio	Number of				Box Size
		Chains	Atoms	Water Molecules	Cl^- Ions	$(nm)^3$
collagen-PVA	1:1	8-8	10472	86210	-	$(18.00)^3$
	1:2	8-16	12168	97356	-	$(17.00)^3$
	2:1	16-8	19248	161272	-	$(20.00)^3$
chitosan-PVA	1:1	8-8	7240	55660	240	$(17.86)^3$
	1:2	8-16	8936	66800	240	$(17.86)^3$
	2:1	16-8	12784	100160	480	$(17.86)^3$

4.2.2.2 Simulation Protocol

The molecular models of PVA, chitosan, and collagen used in this chapter are the same as those in Section 3.2.2.2. All molecular dynamics simulations conducted here follow the same protocol outlined in Section 3.2.2.3. Briefly, simulations were performed using GROMACS 2021, with the CHARMM36m force field, and the TIP3P water model. Systems were energy-minimized using the steepest descent algorithm, then equilibrated in the NVT and NPT ensembles at 300 K and 1 bar. Bond constraints were managed with the LINCS algorithm, temperature and pressure were controlled by the Nosé–Hoover thermostat and Parrinello–Rahman barostat, respectively, and long-range electrostatics were handled using

the Particle-Mesh Ewald method. The analysis methods used in this chapter follow those outlined in Section 3.2.2.4. In brief, trajectories from the 1000 ns production runs were examined. Solvent-accessible surface area (SASA), hydrogen bonding, and interaction enthalpies were calculated with gmx sasa, gmx hbond, and gmx energy, respectively.

4.3 Results and Discussion

4.3.1 Experimental

4.3.1.1 Morphological Analysis Using Scanning Electron Microscopy (SEM)

The scanning electron microscope images in ***Figure 20(a)*** showed that the 2:1 chitosan-to-PVA ratio produces irregular morphology, with visible beads and an average diameter of 98.5 nm (***Table 20)***. In contrast, the 1:1 chitosan-to-PVA ratio (***Figure 20(b)***) produced more uniform, continuous fibers with fewer beads and an average fiber diameter that was 13.8% smaller than in ***Figure 20(a)***. A higher PVA ratio (1:2 chitosan-to-PVA) (***Figure 20(c)***) enhances electrospinning, producing smoother, more uniform nanofibers with an average diameter 22.4% smaller and minimal bead formation compared to ***Figure 20(a)***. A previous study found that changes in chain entanglements due to molecular weight, concentration, and chitosan-additive ratios significantly influence electrospinning instabilities, leading to variations in jet behavior and fiber morphology and ultimately affecting the stability of the electrospinning process [204]. Others also emphasize this and suggest that lower chitosan-to-PVA ratios are preferable for producing uniform nanofibers [205]. Furthermore, researchers indicate that increasing the chitosan-to-PVA ratio results in larger fiber diameters, shorter fiber lengths, and more beads and droplets, demonstrating the significant impact of chitosan on nanofiber quality [206]. This aligns with our results.

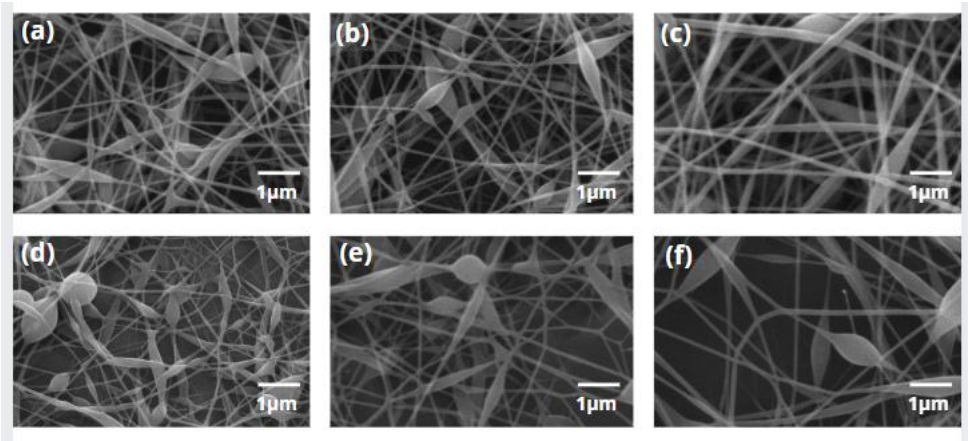

Figure 20. Morphological analysis of nanofiber using SEM imaging. (a) Chitosan-PVA (2:1), (b) Chitosan-PVA (1:1), (c) Chitosan-PVA (1:2), (d) Collagen-PVA (2:1), (e) Collagen-PVA (1:1), and (f) Collagen-PVA (1:2).

At a 2:1 collagen-to-PVA ratio (***Figure 20(d)***), the fibers are irregular, with beads and diameter variations; the average diameter is 90.7 nm. The electrospinning process becomes

more challenging due to phase separation and reduced chain entanglement. This increases the solution's resistance to flow, reduces jet stability, and prevents uniform fiber elongation. Conversely, at 1:1 (***Figure 20(e)***) and 1:2 (***Figure 20(f)***) collagen-to-PVA ratios, increasing the PVA-to-collagen ratio reduces bead formation and enhances fiber uniformity. Compared with ***Figure 20(d),*** the fiber diameter decreases by approximately 18.6% and 25.7%, respectively. Resulting in more uniform fibers with minimal bead formation. This finding agrees with Kan et *al*. [207], who observed that increasing the PVA ratio in the collagen–PVA solution decreased the diameter of the electrospun nanofibers. This effect can be attributed to the solution's enhanced viscosity and conductivity, facilitating finer fiber formation during electrospinning.

Both chitosan–PVA and collagen–PVA systems showed that increasing the PVA ratio improves electrospinning performance by enhancing jet stability and reducing bead formation. A previous study reported that, in chitosan-based systems, strong intermolecular hydrogen bonding restricts polymer-chain mobility and hinders stable jet elongation under applied electric fields. Similarly, collagen-based systems exhibit limitations, including structural instability and poor aqueous stability. These challenges can be effectively mitigated by blending with synthetic polymers [208].

Table 20. Mixing ratios, solution volumes, and average nanofiber diameters, with standard errors (SE) for the Chitosan-PVA and Collagen-PVA samples.

Sample	Mixing Ratio	Volume (mL)	Average Diameter of Nanofibers (nm)	SE (nm)
Chitosan:PVA	2:1	30	98.5	1.4
	1:1	20	84.9	1.9
	1:2	30	76.4	2.4
Collagen:PVA	2:1	30	90.7	1.6
	1:1	20	73.8	1.2
	1:2	30	67.4	1.7

4.3.2 Molecular Modeling

4.3.2.1 Physical Properties of Blended Polymer Systems

To better understand the structural behavior of the polymer systems, several physical parameters were analyzed, including the end-to-end distance, radius of gyration, and aspect ratio, as summarized in ***Table 21***. The end-to-end distance characterizes the overall extension of a polymer chain, whereas the radius of gyration reflects the chain's spatial distribution and compactness around its center of mass. The aspect ratio indicates the anisotropy and elongation of the molecular structure. These parameters are important in electrospinning

because polymer-chain extension and flexibility strongly influence chain entanglement and solution viscoelasticity. Previous studies have reported that during electrospinning, a high stretching rate leads to the formation of a non-equilibrium supermolecular structure, which is crucial to the properties of electrospun polymer nanofibers and underscores the importance of polymer chain entanglement [209].

In the chitosan-PVA systems, chitosan exhibited significantly larger end-to-end distance and radius of gyration than PVA, indicating a more extended, less compact molecular conformation. In contrast, PVA exhibited lower values for both parameters, indicating a more compact, flexible chain structure. The more extended conformation of chitosan can be attributed to its rigid polysaccharide backbone and a strong intermolecular and intramolecular hydrogen-bonding network. Previous studies have reported that hydrated chitosan forms complex two-fold helical chain arrangements and stable hydrogen-bonded structures, including both direct and water-mediated hydrogen bonds, which contribute to its structural stability and extended molecular organization [210]. Meanwhile, the more flexible carbon–carbon backbone of PVA allows greater chain mobility and a more compact molecular arrangement. A previous study reports that the electron diffraction patterns of PVA suggest a zigzag C-atom chain structure with side-chain clustering, indicating a compact arrangement. This configuration contributes to the polymer's flexibility and high elasticity by distorting the main chain [211].

Blending chitosan and PVA solutions at a 1:1 volume ratio reduced both the end-to-end distance and the radius of gyration relative to the isolated chitosan system (***Table 21***). The decrease in these structural parameters indicates that the polymer chains adopted a more compact, less extended configuration after blending. Similar behavior has been reported in chitosan-polyvinylpyrrolidone blends, where good compatibility and low heterogeneity between the polymers were associated with stronger intermolecular interactions and restricted chain mobility [212]. In the present study, the decrease in the structural parameters after blending indicates that interactions between chitosan and PVA limit the spatial extension of the chitosan chains, resulting in a more constrained molecular configuration. The 1:2 chitosan–PVA blend exhibits a distinctive structural setup, characterized by increased end-to-end distance and radius of gyration, indicating a more expanded shape than the 1:1 blend. Still, these values are lower than those of pure chitosan, implying a controlled molecular structure supported by PVA. This balance promotes better polymer chain organization while avoiding excessive expansion. In contrast, the 2:1 chitosan-rich blend exhibited the largest

end-to-end distance and radius of gyration among the chitosan–PVA blend systems, with values of 10.7 nm and 3.3 nm, respectively. Compared with the 1:1 and 1:2 blends, these higher structural parameters indicate that the polymer chains adopt a more extended, less compact molecular configuration when chitosan is present in higher amounts than PVA. The aspect ratio of chitosan-PVA blends offers insight into their structural behavior. Chitosan exhibits a higher aspect ratio than PVA, and this shape is preserved in the blends, which have aspect ratios of (3.1-3.2). This suggests that while PVA is added, it does not reduce the anisotropic nature of chitosan; instead, it affects the spatial arrangement and density of the polymer chains.

Table 21. Structural properties of chitosan–PVA systems at three mixing ratios (1:1, 1:2, and 2:1), including the end-to-end distance, radius of gyration, and aspect ratio, along with their respective standard errors (SE).

Mixing Ratios		end-to-end distance (nm)		radius of gyration (nm)		aspect ratio
		Avg	SE	Avg	SE	
1:1	Chitosan	13.0	0	4.1	0	3.1
	PVA	1.5	0	0.6	0	2.5
	Chitosan–PVA	4.2	0.4	1.3	0.4	3.2
1:2	Chitosan	13.0	0	4.1	0	3.1
	PVA	1.4	0	0.5	0	2.8
	Chitosan–PVA	7.6	0.1	2.4	0.1	3.1
2:1	Chitosan	13.1	0.1	4.1	0	3.1
	PVA	1.1	0	0.5	0	2.2
	Chitosan–PVA	10.7	0.1	3.3	0.1	3.2

The structural behavior of the isolated single-polymer chains in the collagen–PVA systems was evaluated in ***Table 22***. The results showed that collagen exhibited larger end-to-end distance and radius of gyration values than PVA, indicating that collagen adopts a more extended molecular conformation, whereas PVA remains relatively compact. The relatively extended conformation of collagen can be attributed to its organized triple-helical molecular structure and intermolecular hydrogen-bonding interactions, which help maintain a stable, elongated chain arrangement in aqueous environments [213].

Blending collagen and PVA solutions at a 1:1 volume ratio reduces the end-to-end distance and radius of gyration compared with the isolated collagen chain (***Table 22***), indicating that PVA limits the spatial extension of collagen chains. This is likely because PVA segments partially wrap around collagen, resulting in a more ordered structure. This matches what Lan et *al.* [214] reported: in similar collagen-PVA blend systems at a 1:1 ratio, PVA segments partially wrap around collagen, leading to a more ordered structure that improves mechanical properties. The 1:2 collagen-to-PVA blend exhibited an end-to-end distance lower

than that observed for the 1:1 ratio (***Table 22***). This reduction indicates that the collagen chains adopted a less extended configuration in the PVA-rich system. The more compact arrangement may result from intermolecular interactions between collagen and PVA, which can restrict the spatial extension of the collagen chains within the blended system. In the collagen-PVA 2:1 system, the end-to-end distance and radius of gyration were 3.3 nm and 1.2 nm, respectively, showing only small changes compared with the other collagen–PVA blend systems. Unlike the 2:1 chitosan-PVA system, no increase in the end-to-end distance or radius of gyration was observed, indicating that increasing the collagen content did not promote greater chain extension. Instead, the values suggest that the collagen chains remained comparatively compact and spatially constrained despite the higher collagen concentration. This behavior may be attributed to the rigid triple-helical structure of collagen, which limits large-scale conformational flexibility within the blended system [215].

Table 22. Structural properties of collagen–PVA systems at three mixing ratios (1:1, 1:2, and 2:1), including the end-to-end distance, radius of gyration, and aspect ratio, along with their respective standard errors (SE).

Mixing Ratios		end-to-end distance (nm)		radius of gyration (nm)		aspect ratio
		Avg	SE	Avg	SE	
1:1	Collagen	4.2	0.1	1.5	0	2.8
	PVA	2.3	0	1.0	0	2.3
	Collagen–PVA	3.8	0.2	1.3	0.2	2.9
1:2	Collagen	4.1	0.1	1.5	0	2.7
	PVA	2.3	0	1.0	0	2.3
	Collagen–PVA	3.5	0.1	1.3	0.2	2.6
2:1	Collagen	3.4	0.1	1.3	0	2.6
	PVA	2.2	0	1.0	0	2.2
	Collagen–PVA	3.3	0.1	1.2	0.1	2.7

The aspect ratios of the collagen–PVA blended systems further support these observations. Across the three blending ratios, the aspect ratios of the collagen–PVA systems remained within a relatively narrow range of 2.6–2.9 (***Table 22***), which is close to the values observed for isolated collagen chains. This indicates that blending with PVA did not significantly alter the overall anisotropic and elongated molecular character of collagen. Instead, the primary effect of PVA appears to be modifying intermolecular interactions and molecular packing within the blended environment rather than fundamentally changing the overall shape of the collagen chains.

4.3.2.2 Total, Hydrophobic, and Hydrophilic Solvent-Accessible Surface Area (SASA)

SASA analysis was performed on both chitosan–PVA and collagen–PVA blends at three different mixing ratios (1:1, 1:2, and 2:1) to examine how variations in polymer composition affect molecular surface exposure and solvent interactions. Since effective electrospinning relies on a balance between polymer–solvent compatibility and sufficient chain cohesion, understanding the extent of each system's hydrophilicity or hydrophobicity is crucial for predicting solubility, molecular behavior, and packing.

The SASA results for the chitosan–PVA blends listed in ***Table 23*** show that at the (1:1) ratio, the composition has a total SASA of 554.5 nm² and a highly hydrophilic surface (62%), indicating an open, solvent-exposed structure in which chitosan and PVA interact to form a hydrated interface. When the ratio changes to 1:2, the total SASA decreases slightly to 531.5 nm², while the hydrophobic fraction increases to 45%, indicating the influence of the higher PVA content. This rise in hydrophobic exposure suggests that excess PVA causes the complex to pack more tightly, reducing overall solvent accessibility [216]. In contrast, the 2:1 ratio results in a significant increase in total SASA to 938.2 nm², the most solvent-exposed structure among all, mainly due to the dominance of chitosan's polar groups, which raise hydrophilic SASA to 58%. Although this structure is highly hydrated, its large SASA indicates an overly open, swollen configuration where polymer chains are too dispersed.

Table 23. The average SASA values (nm²) for the total surface area in chitosan–PVA systems at the three mixing ratios (1:1, 1:2, and 2:1) are categorized into hydrophobic and hydrophilic regions. The table includes the percentage contributions of hydrophobic and hydrophilic areas, and the standard error (SE) is provided to show measurement variability.

Mixing Ratios		Solvent Accessible Surface Area (SASA) (nm^2)							
		Total		Hydrophobic			Hydrophilic		
		Avg	SE	Avg	SE	%	Avg	SE	%
1:1	Chitosan	447.2	0.1	175.9	0	39%	271.2	0.1	60%
	PVA	56.3	0	41.1	0	73%	15.2	0	27%
	Chitosan–PVA	554.5	0.1	208.3	0.1	37%	346.2	0.1	62%
1:2	Chitosan	449.8	0.1	177.1	0	39%	272.6	0.1	60%
	PVA	101.6	0.1	75.0	0.1	73%	26.6	0	26%
	Chitosan–PVA	531.5	0.2	242.4	0.1	45%	289.1	0.1	54%
2:1	Chitosan	893.9	0.1	352.2	0	39%	541.6	0.1	60%
	PVA	63.7	0	47.1	0	73%	16.5	0	26%
	Chitosan–PVA	938.2	0.1	389.8	0.1	41%	548.3	0.1	58%

Across all ratios, chitosan consistently exhibits high hydrophilic exposure [217], while PVA appears more hydrophobic despite its OH groups due to its carbon-rich backbone. These contrasting properties explain why SASA-ratio-dependent shifts affect electrospinning

performance. Effective electrospinning requires a balance between solubility and chain cohesion: the polymers must be sufficiently hydrated to dissolve well, yet compact enough to entangle and form a stable jet [218]. The 1:2 chitosan–PVA blend achieves this balance best because its moderate hydrophilicity ensures solvation, while its higher hydrophobic exposure promotes chain cohesion. In comparison, the 1:1 blend is adequately hydrated but less compact, whereas the 2:1 blend is overly extended, resulting in weak chain entanglement.

The SASA results for the collagen–PVA systems shown in ***Table 24*** demonstrate clear changes in surface exposure with varying mixing ratios. In the 1:1 blend, the complex exhibits a total SASA of 559.3 nm², with a dominant hydrophobic surface (67%) and a smaller hydrophilic area (32%). When the ratio shifts to 1:2, the total SASA increases to 612.2 nm², and the hydrophilic SASA rises to 41%, while hydrophobic exposure decreases to 58%. This change reflects the increasing influence of PVA, whose flexible chains and numerous hydroxyl groups migrate toward the solvent interface, exposing more hydrophilic regions [194].

Table 24. The average SASA values (nm²) for the total surface in collagen–PVA systems at the three mixing ratios (1:1, 1:2, and 2:1) are categorized into hydrophobic and hydrophilic regions. The table includes the percentage contributions of hydrophobic and hydrophilic areas, and the standard error (SE) is provided to show measurement variability.

Mixing Ratios		Solvent Accessible Surface Area (SASA) (nm^2)							
		Total		Hydrophobic			Hydrophilic		
		Avg	SE	Avg	SE	%	Avg	SE	%
1:1	Collagen	460.9	0.7	298.3	0.4	64%	162.5	0.2	35%
	PVA	164.5	0.2	122.6	0.2	74%	41.8	0.1	25%
	Collagen–PVA	559.3	1.1	375.1	0.7	67%	184.2	0.3	32%
1:2	Collagen	497.5	0.6	317.7	0.4	63%	179.7	0.2	36%
	PVA	263.1	0.1	121.5	0.1	46%	141.5	0.1	53%
	Collagen–PVA	612.2	1.1	358.7	0.6	58%	253.4	0.4	41%
2:1	Collagen	885.4	0.8	567.4	0.5	64%	317.9	0.3	35%
	PVA	140.1	0.1	64.4	0	45%	75.6	0	53%
	Collagen–PVA	945.4	1.1	588.3	0.6	62%	357.1	0.4	37%

Consequently, the PVA-rich system becomes more water-facing and significantly more hydrophilic compared to the 1:1 system. Conversely, the 2:1 collagen-rich blend shows the highest total SASA at 945.4 nm², with 62% hydrophobic and 37% hydrophilic surface areas. This strong hydrophobic dominance occurs because the higher collagen content reveals more hydrophobic residues, such as proline and hydroxyproline [219], resulting in a highly expanded, solvent-accessible structure. Among the three systems, the PVA-rich 1:2 ratio has the most hydrophilic surface, the collagen-rich 2:1 ratio exhibits the most expanded, hydrophobic structure, and the 1:1 system remains intermediate, though still primarily

hydrophobic. Considering electrospinning needs, which require good solubility, sufficient hydrophilic exposure, and proper chain cohesion, the 1:2 collagen–PVA mixture offers the best balance, providing improved hydrophilicity without the excessive expansion seen in the collagen-rich system.

4.3.2.3 Hydrogen Bonds

The hydrogen-bonding results for the chitosan–PVA mixtures shown in ***Table 25*** offer detailed insights into polymer–polymer and polymer–water interactions. In the 1:1 chitosan–PVA blend, only 13.3 hydrogen bonds form between chitosan and PVA, a significant decrease from pure chitosan (83.1) and pure PVA (81.1). This suggests that when mixed in equal proportions, chitosan and PVA do not interact strongly, likely because their functional groups face outward and form hydrogen bonds with surrounding water rather than each other. This is supported by the high number of polymer–water hydrogen bonds, reaching 704.7 for chitosan and 226.6 for PVA, indicating a hydration-focused structure of the blend. These findings are consistent with the SASA results, which indicate a hydrophilic, solvent-exposed surface. ***Figure 21*** shows a representative configuration of chitosan and PVA chains from MD simulations, visualized with VMD. One chain from each polymer is displayed to highlight the intermolecular arrangement and solvent exposure related to the hydrogen-bonding behavior discussed in ***Table 25***.

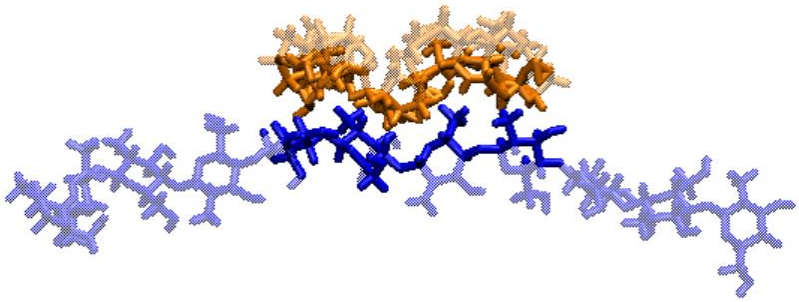

Figure 21. Representative molecular configuration of the chitosan–PVA system obtained from the molecular dynamics trajectory and visualized with VMD. For clarity, one polymer chain from each component is shown, with chitosan in blue and PVA in orange.

When the ratio shifts to 1:2 (chitosan: PVA), the hydrogen-bonding pattern changes to reflect a more organized and stable mixture. The number of chitosan–PVA hydrogen bonds increases to 23.1, indicating that chitosan and PVA interact more effectively than in the 1:1 blend. Simultaneously, both polymers form more hydrogen bonds with water. Chitosan–water bonding rises sharply to 1237.8, and PVA–water bonding increases to 502.0, contributing to a high level of hydration in the mixture. Although the polymers interact, much of their surface

remains accessible to water. This aligns with the SASA findings, which indicate that the 1:2 mixture is highly hydrated yet remains compact. The additional PVA enables its flexible –OH-rich chains to partially encase chitosan, regulating its expansion while still exposing many hydrophilic groups to water.

Table 25. Hydrogen-bonding characteristics in chitosan–PVA systems at three mixing ratios (1:1, 1:2, and 2:1), classified as polymer–polymer and polymer–water interactions. Values are given as the average hydrogen-bond counts per interaction type and the total number of hydrogen bonds in each system. Standard errors (SE) are included to indicate measurement variability.

Mixing Ratios		Hydrogen Bonds				
		Polymer-Polymer		Polymer-Water		Total
		Avg	SE	Avg	SE	
1:1	Chitosan	83.1	0	704.7	0.4	787.8
	PVA	81.1	0	226.6	0.1	307.7
	Chitosan–PVA	13.3	0	-	-	-
1:2	Chitosan	83.6	0.1	1237.8	0.3	1321.4
	PVA	179.9	0.1	502.0	0.2	681.9
	Chitosan–PVA	23.1	0.1	-	-	-
2:1	Chitosan	178.3	0.2	2822.1	2.8	3000.4
	PVA	90.4	0.1	312.4	1.0	402.8
	Chitosan–PVA	22.2	0.1	-	-	-

In the 2:1 chitosan-rich blend, the number of chitosan–PVA hydrogen bonds was 22.2, similar to the 1:2 ratio, indicating that increasing chitosan content does not strengthen chitosan–PVA intermolecular cohesion. Instead, the system becomes dominated by hydrogen bonding with water. Chitosan forms a very high number of hydrogen bonds with water (2822.1), and PVA also contributes additional hydration through 312.4 polymer–water bonds. This strong hydration indicates that both polymers prefer to interact with water rather than with each other, resulting in highly solvated, dispersed polymer chains. The SASA results support this, revealing that the 2:1 mixture has the highest total SASA (938.2 nm^2) and adopts a more open, expanded structure. Despite its strong hydrophilicity, the large number of polymer–water bonds causes excessive swelling and poor chain entanglement. This makes the 2:1 blend structurally unstable and unsuitable for electrospinning, despite its high water affinity.

The hydrogen-bonding patterns observed in collagen–PVA are detailed in ***Table 26***. In the 1:1 collagen–PVA mixture, the number of collagen–PVA hydrogen bonds formed is relatively low at 33.9, which is significantly less than the strong intermolecular bonds in pure collagen (161.2). It is only slightly lower than in pure PVA (35.5). This suggests that when collagen and PVA are present in equal amounts, they do not interact strongly and instead

orient their functional groups toward the solvent. This is reflected in the polymer–water hydrogen-bonding: collagen forms 164.3 bonds with water, while PVA forms 378.5, indicating that PVA interacts more readily with water. The difference is due to their chemical structures: PVA has numerous accessible hydroxyl (–OH) groups along a flexible backbone, making it highly capable of hydrogen bonding with water [220]. In contrast, collagen's triple-helix structure limits access to many of its polar groups [221]. As a result, the 1:1 blend becomes mainly hydration-driven, with both polymers preferring interaction with water over forming strong intermolecular bonds with each other. To further illustrate the intermolecular arrangement in the collagen–PVA system, a representative configuration from the molecular dynamics trajectory was analyzed using VMD (***Figure 22***). One collagen chain and one PVA chain were selected to highlight polymer–polymer proximity and chain organization. As shown in the figure, PVA chains tend to cluster closely with collagen through their hydroxyl-rich backbone.

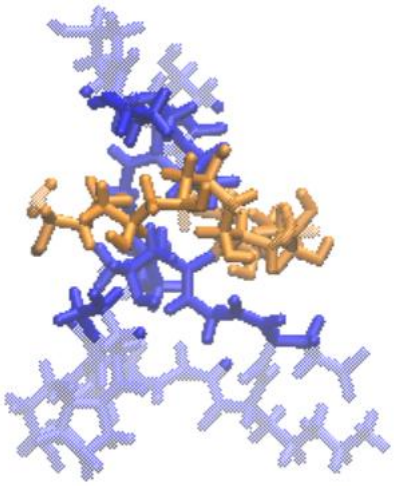

Figure 22. Representative molecular configuration of the collagen–PVA system extracted from the molecular dynamics trajectory and visualized using VMD. One polymer chain from each component is shown for clarity, with collagen displayed in blue and PVA displayed in orange.

When the ratio shifts to 1:2 (collagen: PVA), significant changes in hydrogen-bonding behavior occur, indicating a more organized blend structure. The collagen–PVA hydrogen bonds increase markedly from 33.9 at the 1:1 ratio to 74.7, indicating that the interaction between collagen and PVA becomes much stronger at higher PVA concentrations. This improvement happens because PVA's flexible chains and numerous hydroxyl (–OH) groups are more accessible, enabling more of them to engage with the collagen surface. As a result, more PVA chains can align with collagen's hydrogen-bonding sites, enhancing intermolecular

cohesion. At the same time, the mixture becomes significantly more hydrated, mainly due to PVA. PVA forms 737.9 hydrogen bonds with water, nearly doubling its hydration level compared to the 1:1 system (378.5). Collagen–water bonding remains nearly the same at 162.8, indicating that collagen's triple-helical structure limits further exposure of its polar groups. Since PVA dominates the surface at this ratio, its extensive –OH–water interactions primarily drive hydration [222]. This results in a surface environment that is highly water-attracting but still stabilized by improved collagen–PVA interactions. These hydrogen-bond patterns align directly with the SASA results. The increased PVA content leads to a surface abundant in hydrophilic –OH groups, explaining the higher hydrophilic SASA percentage observed in the system with more PVA.

Table 26. Hydrogen-bonding characteristics in collagen–PVA systems at three mixing ratios (1:1, 1:2, and 2:1) are categorized into polymer–polymer and polymer–water interactions. Values are reported as average hydrogen-bond counts per interaction type and as total hydrogen-bond counts per system. Standard errors (SE) are included to indicate measurement variability.

Mixing Ratios		Hydrogen Bonds				
		Polymer-Polymer		Polymer-Water		Total
		Avg	SE	Avg	SE	
1:1	Collagen	161.2	0.1	164.3	4.4	325.5
	PVA	35.5	0.1	378.5	0.3	414.0
	Collagen–PVA	33.9	0.1	-	-	-
1:2	Collagen	152.0	0.1	162.8	3.8	314.8
	PVA	76.9	0.1	737.9	0.5	814.8
	Collagen–PVA	74.7	0.2	-	-	-
2:1	Collagen	306.3	0.2	2735.7	0.9	3042.0
	PVA	33.0	0.1	383.8	0.3	416.8
	Collagen–PVA	34.9	0.1	-	-	-

In the collagen-rich 2:1 system, collagen primarily governs the interactions, as indicated by the hydrogen-bonding data. It forms a very high number of polymer–water hydrogen bonds (2735.7), much more than in the 1:1 or 1:2 mixtures. This increase is simply due to the greater amount of collagen present, which exposes more functional groups to the solvent. The higher collagen concentration provides more amide, hydroxyl, and carbonyl groups for water to interact with, greatly improving the system's hydration [223]. In contrast, PVA–water hydrogen bonding is fairly low (383.8) because collagen mainly covers the surface. With most of the accessible area covered by collagen, PVA's hydroxyl groups are less exposed and contribute less to water bonding. Meanwhile, the number of collagen–PVA hydrogen bonds (34.9) remains low, indicating weak interactions. This suggests that although the system interacts strongly with water, it does not form strong internal cohesive bonds. This very high level of hydration causes collagen chains to swell and separate. Water molecules

infiltrate between the chains, preventing them from coming close enough to form a dense or entangled structure [224]. This agrees with the SASA results.

4.3.2.4 Interaction Enthalpies

Inter-chain interaction enthalpy is vital for understanding the structural features of polymer blends, as it influences their miscibility, stability, and overall physical properties. The strength of these interactions determines how closely polymer chains associate, which in turn affects their density and entanglement density. By analyzing interaction enthalpies across various mixing ratios, one can observe how changes in composition affect polymer cohesion and how these variations influence processing performance, such as suitability for electrospinning.

Table 27 displays the interaction enthalpies for the chitosan–PVA systems at three different mixing ratios. In the 1:1 chitosan–PVA system, the interaction enthalpy is only -1121.8 kJ·mol^{-1}. The Coulombic component is –820.5 kJ·mol^{-1} because both chitosan and PVA contain polar functional groups that produce limited electrostatic interactions [225], while the Lennard-Jones interaction of –301.3 kJ·mol^{-1} remains weak due to poor chain packing at this ratio. In their pure forms, both chitosan and PVA exhibit much higher interaction enthalpies of –62420.2 kJ·mol^{-1} and –7500.2 kJ·mol^{-1}, respectively. Chitosan, with its high density of polar groups, forms strong self-associations [226], while PVA demonstrates moderate cohesion through hydrogen bonds along its backbone. When blended in equal parts, these strong self-interactions are broken, but they are not replaced by equally strong chitosan–PVA bonds. Consequently, the mixture does not form a stable, cohesive network and remains loosely connected.

In the 1:2 chitosan–PVA system, the overall interaction enthalpy increases slightly to –1193.2 kJ·mol^{-1}, indicating a modest increase in inter-chain attraction compared to the 1:1 blend. This mainly results from a stronger Coulombic interaction (–884.4 kJ·mol^{-1}), showing enhanced electrostatic interactions between the polymers. The increase occurs because the higher PVA content provides more hydroxyl groups, which facilitate better alignment with chitosan's amino and hydroxyl groups. As a result, the polymers come into closer contact and form more interactions than in the 1:1 ratio. The Lennard-Jones interaction (–308.7 kJ·mol^{-1}) remains similar to that in the 1:1 system, indicating that van der Waals interactions do not change significantly, and the improvement in stability is mainly due to stronger polar interactions rather than increased packing density. Although the interaction enthalpy remains

much lower than in the pure polymers, indicating that the blend remains much weaker than chitosan–chitosan or PVA–PVA self-associations, the increase confirms that the polymers interact more effectively when PVA is in excess.

In the 2:1 chitosan–PVA system, the overall interaction enthalpy is higher at –1618.3 kJ·mol⁻¹, indicating stronger inter-chain attraction than in the 1:1 and 1:2 blends. This mainly results from the high Coulombic interaction (–1161.8 kJ·mol⁻¹), which reflects increased density of chitosan's polar and partially protonated groups when it is in excess. With more chitosan chains available, electrostatic interactions between amino and hydroxyl groups occur more frequently, leading to greater energetic stability [227]. Additionally, the Lennard-Jones interaction is high (–456.5 kJ·mol⁻¹), indicating slightly improved van der Waals interactions as chitosan chains interact more directly with one another rather than with PVA.

Table 27. The inter-chain interaction enthalpy for chitosan–PVA systems at the three mixing ratios (1:1, 1:2, and 2:1) includes Coulombic and Lennard-Jones (LJ) interactions. The table reports the average enthalpy (Avg), standard error (SE), average enthalpy per chain (Avg/C), total enthalpy (Sum), and total enthalpy per chain (Sum/C) for each system.

Mixing Ratios		Inter-Chain Interaction Enthalpy (kJ·mol^{-1})							
		Coulombic			LJ			Total	
		Avg	SE	Avg/C	Avg	SE	Avg/C	Sum	Sum/C
1:1	Chitosan	-58711.9	1.2	-7338.9	-3708.3	1.1	-463.5	-62420.2	-7802.5
	PVA	-5560.3	1.3	-695.0	-1939.9	0.4	-242.4	-7500.2	-937.5
	Chitosan–PVA	-820.5	0.8	-51.2	-301.3	0.3	-18.8	-1121.8	-70.1
1:2	Chitosan	-58854.9	1.1	-7356.8	-3713.0	1.1	-464.1	-62567.9	-7820.9
	PVA	-11673.5	2.1	-729.5	-3679.6	0.6	-229.9	-15353.1	-959.5
	Chitosan–PVA	-884.4	0.8	-36.8	-308.8	0.8	-12.8	-1193.2	-49.7
2:1	Chitosan	-117247	1.7	-7327.9	-7467.4	1.5	-466.7	-124714	-7794.6
	PVA	-5398.8	1.5	-674.8	-2094.5	0.5	-261.8	-7493.3	-936.6
	Chitosan–PVA	-1161.8	0.8	-48.4	-456.5	0.3	-19.0	-1618.3	-67.4

Table 28 illustrates how the inter-chain interaction enthalpies for collagen–PVA vary with the three different mixing ratios, demonstrating the influence of composition on Coulombic and Lennard-Jones (LJ) interactions. In the 1:1 collagen–PVA blend, the overall interaction enthalpy is –2548.4 kJ·mol⁻¹, significantly lower than that of the pure polymers. Collagen alone shows a much higher value (–55279.3 kJ·mol⁻¹) due to its dense electrostatic and van der Waals interactions within its triple-helical structure [222], while pure PVA (–10861.1 kJ·mol⁻¹) exhibits moderate cohesion. When combined equally, these strong self-interactions are reduced but are not replaced by substantial collagen–PVA interactions, as indicated by the weak Coulombic (–1204.7 kJ·mol⁻¹) and Lennard-Jones (–1343.7 kJ·mol⁻¹) interactions. This suggests poor alignment and packing of the polymers, resulting in a loosely

connected structure rather than a cohesive network. This weak interaction supports the hydrogen-bonding results.

In the 1:2 collagen–PVA blend, the overall interaction enthalpy rises to –5338.9 kJ·mol⁻¹, indicating stronger intermolecular attraction than in the 1:1 system. This increase is mainly due to a higher Coulombic interaction energy (–2633.7 kJ·mol⁻¹), suggesting that adding more PVA enhances electrostatic compatibility between the polymers. With more PVA, extra hydroxyl groups can interact with collagen's polar residues, leading to better alignment and stronger polar interactions than in the balanced mixture. The Lennard-Jones interaction also becomes more significant (–2705.2 kJ·mol⁻¹), showing tighter chain packing and improved van der Waals forces, which were limited in the 1:1 blend. Despite these increases, the interaction enthalpy remains much lower than those of pure collagen (–115069.2 kJ·mol⁻¹) and pure PVA (–10861.1 kJ·mol⁻¹), indicating that both still favor self-association over blending. However, the increase in Coulombic and LJ interactions at a 1:2 ratio suggests stronger interactions between collagen and PVA when PVA is in excess.

Table 28. The inter-chain interaction enthalpy for collagen–PVA systems at the three mixing ratios (1:1, 1:2, and 2:1) includes Coulombic and Lennard-Jones (LJ) interactions. The table reports the average enthalpy (Avg), standard error (SE), average enthalpy per chain (Avg/C), total enthalpy (Sum), and total enthalpy per chain (Sum/C) for each system.

Mixing Ratios		Inter-Chain Interaction Enthalpy (kJ·mol^{-1})							
		Coulombic			LJ			Total	
		Avg	SE	Avg/C	Avg	SE	Avg/C	Sum	Sum/C
1:1	Collagen	-46204.2	2.4	-5775.5	-9075.1	2.0	-1134.3	-55279.3	-6909.9
	PVA	-9710.6	2.5	-1213.8	-1150.5	0.8	-143.8	-10861.1	-1357.6
	Collagen–PVA	-1204.7	1.5	-75.2	-1343.7	1.3	-83.9	-2548.4	-159.2
1:2	Collagen	-46558.4	2.4	-5819.8	-8897.6	1.1	-1112.2	-55456.0	-6932.0
	PVA	-18894.2	3.1	-1180.8	-2218.1	1.2	-138.6	-21112.3	-1319.5
	Collagen–PVA	-2633.7	2.8	-109.7	-2705.2	2.4	-112.7	-5338.9	-222.4
2:1	Collagen	-96527.2	1.2	-6032.9	-18542	2.1	-1158.8	-115069.2	-7191.8
	PVA	-9835.5	2.0	-1229.4	-1194.5	1.1	-149.3	-11030.0	-1378.7
	Collagen–PVA	-1244.7	2.2	-51.8	-1337.6	1.9	-55.7	-2582.3	-107.5

In the 2:1 collagen–PVA blend, the total interaction enthalpy is –2582.3 kJ·mol⁻¹, staying relatively low despite the higher collagen content. The Coulombic (–1244.7 kJ·mol⁻¹) interaction shows only a slight change from the 1:1 mixture, indicating that adding more collagen does not strengthen electrostatic interactions with PVA. This is because collagen already dominates the polar interactions, and excess collagen chains mainly interact with water rather than forming new electrostatic contacts with PVA. The Lennard-Jones interaction (–1337.6 kJ·mol⁻¹) also remains weak, showing that chains do not pack more tightly or have

improved van der Waals interactions at this ratio. In contrast, the pure polymers exhibit very strong self-association, with pure collagen at –115069.2 kJ·mol^{-1} and pure PVA at –10861.1 kJ·mol^{-1}, indicating that both polymers are more inclined to interact with their own chains rather than with each other. In the 2:1 blended system, interactions between the two polymers decrease because excess collagen becomes highly hydrated, as shown by hydrogen-bond analysis. Water molecules occupy available interaction sites, preventing collagen chains from bonding with one another or with PVA. As a result, the polymer network becomes more dispersed rather than more cohesive.

4.4 Conclusion

This study investigates the morphology of nanofibers made from chitosan–PVA and collagen–PVA blends. The results show that adding PVA to chitosan and collagen solutions is essential for enhancing nanofiber quality. PVA increases solution viscosity, reduces bead formation, and promotes the formation of uniform, continuous fibers. These improvements are due to greater molecular chain entanglement, which stabilizes the electrospinning process and leads to more consistent fiber production.

Molecular dynamics (MD) simulations complement experimental results by providing a molecular-level understanding of how chitosan–PVA and collagen–PVA blends' molecular interactions affect solution behavior. Producing stable nanofibers depends on balancing hydration, intermolecular compatibility, and chain packing. Molecular dynamics results indicate that this balance is significantly affected by the polymer ratio: PVA-rich blends promote better mixing, more stable interactions, and a solution environment suitable for continuous jet formation. Conversely, mixtures with higher polymer content tend to overhydrate or separate between chains, leading to structures lacking the cohesion necessary for effective fiber formation. In all analyses, the 1:2 polymer-to-PVA blends consistently exhibited optimal structural balance. Higher PVA content enhanced compatibility with biopolymers and improved molecular interactions without compromising solubility. All computational metrics, such as SASA, hydrogen-bonding patterns, and interaction enthalpies, confirmed that the 1:2 systems were the most compact, organized, and stable configurations.

The simulation results closely matched the experimental electrospinning findings. The 1:2 blends produced the most consistent and well-formed nanofibers, while other ratios showed defects consistent with their expected molecular instability.

Chapter 5: Summary

Understanding how a polymer's molecular structure dictates its macroscopic behavior during processing is essential for designing high-performance materials. While electrospinning is a premier method for fabricating advanced nanofibers, its success depends entirely on the structural organization and interactions within the polymer solution. To link these molecular mechanisms to macroscopic processing outcomes, this study integrates atomistic molecular dynamics (MD) simulations with empirical electrospinning experiments. By systematically evaluating three distinct polymers, PVA, chitosan, and collagen, this investigation clarifies how polymer architecture shapes solution dynamics, governs jet stability, and ultimately determines nanofiber morphology.

Natural polymers such as collagen and chitosan are highly attractive candidates for advanced applications. However, their complex molecular structures pose significant challenges for solution processing and electrospinning. Collagen has a rigid triple-helical structure maintained by specific amino-acid sequences, extensive hydrogen bonding, and hierarchical assembly into fibrils. While this structure is vital for collagen's mechanical strength and biological function in native tissues, it greatly reduces its water solubility and chain flexibility, making it difficult to form stable electrospinning jets. Although less structurally complex than collagen, chitosan presents unique processing challenges, mainly due to its degree and pattern of N-acetylation. These structural features affect chain rigidity, crystallinity, and the distribution of hydrogen-bonding sites along the polymer backbone. In acidic solutions, protonation of amino groups induces strong electrostatic repulsion between chains, promoting chain extension but also increasing the solution's surface tension and instability. As a result, chitosan solutions often show poor chain entanglement and unstable jet behavior, restricting the formation of continuous nanofibers during electrospinning.

To fundamentally understand these macroscopic processing challenges for collagen, we found it critical to refocus our investigation on collagen's core structural unit, tropocollagen. Recognizing that bulk material performance originates at this foundational level, we determined that isolating tropocollagen's behavior is a prerequisite for elucidating macroscopic mechanisms. To accomplish this, Molecular dynamics simulations were used to analyze hexameric and heptameric tropocollagen assemblies rich in proline or hydroxyproline residues, isolating the effects of packing density and amino acid composition on

intermolecular interactions. The results show that hydroxyproline-rich tropocollagen assemblies form more contacts, display stronger intermolecular hydrogen bonding, and have a larger hydrophilic solvent-accessible surface area. These structural features increase overall stability while moderating interactions with water, explaining differences in rigidity, hydration behavior, and resistance to structural disruption. Comparisons between hexameric and heptameric assemblies further indicate that supramolecular packing plays a key role in controlling flexibility, molecular mobility, and the ability of collagen structures to withstand dynamic fluctuations. By linking these nanoscale structural mechanisms to macroscopic mechanical behavior and processing responses, the tropocollagen-level analysis offers mechanistic insight into how collagen's intrinsic molecular organization governs its behavior.

Following our analysis of tropocollagen, we expanded our study to investigate solution behavior during electrospinning across three polymers: PVA, chitosan, and collagen. This allowed us to systematically analyze how molecular-level differences among these materials affect their macroscopic solution properties. Electrospinning experiments showed that PVA easily forms uniform, bead-free nanofibers, while pure chitosan and collagen solutions fail to produce stable nanofibers under similar conditions. Molecular simulations provide a structural explanation for these results. PVA chains assume compact, isotropic shapes and form extensive hydrogen bonds with water, resulting in homogeneous solutions with enough chain cohesion for stable jet formation. In contrast, collagen's rigid triple-helical structure and relatively low hydrophilic surface area limit its interaction with water and decrease chain mobility in solution, whereas chitosan's highly extended, flexible chains form extensive hydrogen bonds with water, leading to strong solvation and chain separation rather than effective intermolecular bonding.

Consequently, blending natural polymers with PVA was systematically evaluated to improve electrospinning performance. Both experimental results and MD simulations show that PVA stabilizes collagen–PVA and chitosan–PVA systems by modifying hydrogen-bonding networks, solvent-accessible surface areas, and chain packing. The blend ratio is key. PVA-rich blends offer better solubility, improved hydration balance, and stronger intermolecular cohesion, which help produce uniform nanofibers with fewer beads. In contrast, polymer-rich blends tend to become excessively hydrated and structurally expand, leading to weak chain entanglement and poor electrospinning performance. These findings indicate that successful electrospinning depends on both the chemical composition and the reorganization of molecular structures within the blended systems.

Overall, this work demonstrates that understanding polymer behavior at the molecular scale can systematically guide formulation design and optimize electrospinning conditions. By explaining how polymer architecture and intermolecular interactions govern solution dynamics and jet stability, this study reduces reliance on trial-and-error methods in nanofiber production. As a result, biopolymer electrospinning processes can become fundamentally more reproducible, use raw materials more efficiently, and generate significantly less waste, ultimately promoting the sustainable fabrication of advanced biopolymer-based nanofibrous materials.

Chapter 6: New Scientific Results

My PhD research's main findings are summarized, with an emphasis on the new scientific contributions of this work.

1st Thesis

Insights into collagen structure can be gained by studying the smaller, more computationally accessible tropocollagen. In this thesis, molecular dynamics simulations were used to characterize, for the first time, model hexameric and heptameric tropocollagen assemblies enriched in proline or hydroxyproline residues. The principal scientific contributions of this work are summarized as follows:

a) Hexameric tropocollagen exhibits tighter molecular packing and stronger interactions than the heptameric assembly.

Hydrogen bond analysis showed that the hexamer forms more hydrogen bonds than the heptamer in both Pro- and Hyp-enriched systems. This observation is further supported by the higher per-strand interaction energy in the hexameric assemblies, indicating stronger interactions. Collectively, these findings demonstrate that the hexameric architecture promotes more efficient molecular packing and is predicted to provide greater structural stability than the heptameric architecture.

b) Heptameric tropocollagen provides enhanced solvent accessibility, which may facilitate intermolecular interactions and broaden its functional applicability.

Solvent-accessible surface area analysis showed that the heptameric assemblies have higher average solvent-accessible surface areas than the corresponding hexamers. Increased solvent accessibility is expected to promote interactions with surrounding molecules. Furthermore, these findings are relevant because disease-associated mutations frequently occur within regions of limited solvent accessibility [164], suggesting that differences in assembly architecture may influence the structural and functional consequences of such mutations.

2nd Thesis

Molecular dynamics simulations elucidated the molecular mechanisms governing the electrospinnability of PVA, chitosan, and collagen by revealing how molecular conformation,

intermolecular interactions, and polymer–solvent interactions collectively determine solution processability and nanofiber formation. The principal scientific contributions of this work are:

a) PVA exhibits molecular characteristics that promote efficient electrospinning and the formation of uniform nanofibers.

Experimental electrospinning produced smooth, bead-free PVA nanofibers, while molecular dynamics simulations showed that this behavior arises from the polymer's balanced hydrophilic–hydrophobic surface, high chain flexibility, weak polymer–polymer interactions, and strong polymer–water hydrogen bonding. These molecular characteristics enable efficient dissolution and sufficient chain entanglement, providing the molecular basis for PVA's superior electrospinning performance.

b) Chitosan exhibits intramolecular interactions that limit its electrospinnability despite its strong affinity for water.

Molecular dynamics simulations revealed that chitosan possesses strong intra-chain hydrogen bonding, pronounced electrostatic interactions, and extensive polymer–water hydrogen bonding. Together, these molecular interactions promote the formation of a dense hydration shell and highly viscous solutions, limiting chain rearrangement and preventing the formation of a uniformly dispersed, well-entangled polymer solution required for stable electrospinning.

c) Collagen exhibits strong intermolecular cohesion that favors fibrillar aggregation over electrospinnable solution formation.

The simulations showed that collagen forms an extensive network of intra- and inter-chain hydrogen bonds, along with strong hydrophobic and intermolecular interaction enthalpies that stabilize its fibrillar architecture. These interactions reduce solvent accessibility, limit effective dissolution, and promote molecular aggregation despite substantial polymer–water interactions.

3rd Thesis

The combined experimental and molecular dynamics investigation established that the electrospinnability of collagen–PVA and chitosan–PVA blends is governed by the molecular balance between polymer hydration and intermolecular cohesion. Increasing the PVA content shifts this balance toward homogeneous molecular organization, yielding stable electrospinning solutions and improved nanofiber formation.

a) Molecular dynamics simulations elucidated the molecular mechanisms underlying the superior electrospinnability of PVA-rich blends.

SASA analysis showed that increasing PVA content promotes a more homogeneous molecular organization by maintaining an appropriate balance between solvent accessibility and molecular packing. Hydrogen-bond analysis further demonstrated that PVA-rich blends form a cohesive intermolecular network while preserving sufficient polymer–water interactions to ensure effective solvation. These molecular characteristics promote homogeneous solution structures that sustain continuous electrospinning.

b) Excessive polymer content limits effective polymer–PVA interactions and molecular organization.

Increasing the chitosan or collagen content shifts the balance among polymer–polymer, polymer–PVA, and polymer–water interactions. Higher biopolymer concentrations expose more polar functional groups to the solvent, strengthening interactions with water and promoting self-association among similar polymer chains rather than enabling effective polymer–PVA integration. As a result, polymer chains adopt a more expanded, solvent-exposed conformation, reducing chain proximity, molecular packing efficiency, and the formation of a continuous, entangled network with PVA.

Overall, this thesis established a molecular-level understanding of how structural organization and polymer–solvent interactions govern the stability and processability of collagen- and chitosan-based systems. The tropocollagen study showed that variations in molecular assembly architecture influence collagen stability, packing efficiency, and solvent accessibility. The study further revealed that the molecular characteristics of PVA, chitosan, and collagen directly govern their electrospinnability through differences in chain flexibility, hydrogen bonding, hydration behavior, and intermolecular interactions. Finally, the polymer blending study demonstrated that optimizing the polymer-PVA ratio is essential for balancing hydration and cohesion: excessive biopolymer content promotes excessive hydration, resulting in a more extended and less compact chain arrangement with reduced molecular organization, whereas appropriate PVA incorporation enables stable solutions and uniform nanofiber formation. Collectively, these findings highlight that molecular-scale interactions provide the fundamental basis for controlling biomaterial structure, processing behavior, and nanofiber performance, offering new insights for the rational design of advanced natural polymer-based materials.

Scientific publications

Publications Related to the Subject of the Dissertation

1. **Nesreen Alkanakri**, Babak Minofar, and Michael C. Owen. ″Effects of Hydroxylation and Packing Geometry on Tropocollagen Stability: Insights from Molecular Dynamics Simulations,″ *The Journal of Physical Chemistry B***,** 2025, 129: 40, 10490–10503. https://doi.org/10.1021/acs.jpcb.5c02935. (Q1; IF=2.9)

2. **Nesreen Alkanakri**, Kolos Molnár, Babak Minofar, Zsolt Fejes, Kardo Khalid Abdullah, and Michael C. Owen. ″Properties of PVA, Chitosan, and Collagen Solutions and Their Role in Electrospinning: Insights from Simulations and Experiments,″ *The Journal of Physical Chemistry B*, 2026, 130: 1, 419–430. https://doi.org/10.1021/acs.jpcb.5c06703.

3. **Nesreen Alkanakri** and Michael C. Owen. ″ Molecular dynamics simulations of the proline and hydroxyproline of collagen,″ *Multidiscipinary Sciences,* 2024, 14: 1, 71-82. https://doi.org/10.35925/j.multi.2024.1.7.

Further Publications

1. **Nesreen Alkanakri** and Michael C. Owen. ″ Temperature- and Composition-Dependent Hydrogen Bonding in Chitosan–PNIPAm Blends: A Molecular Dynamics Study,″ *Symposium on Polymer(s) Innovation & Soil Innovation for Regenerative Agriculture (SPI-SIRA 2025)- Conference publications,* 2025.

2. **Nesreen Alkanakri** and Michael C. Owen. ″ Preparation of Chitosan and Collagen Nanofiber Mats,″ *Symposium on Polymer(s) Innovation- Conference publications,* 2024.

3. **Nesreen Alkanakri** and Michael C. Owen. ″ A Review of Biomaterials, definition, basics, and description of the most used biomaterials,″ *Doktorandusz Almanach,* 2023, 58-63.

Presentations and Posters

1. ^{14}th Visegrad Symposium on Biomolecular Interactions

Oral presentation/Spala, Poland, 2026.27 – 30.05.

Computational and experimental study of PVA biopolymer blends

2. [13]th Visegrad Symposium on Biomolecular Interactions

Oral presentation/Ostravice, Czech Republic, 2025.18 – 21.06.

Experimental and Computational Insights into Electrospinning Solutions of PVA, Chitosan, and Collagen.

3. [12]th Visegrad Symposium on Biomolecular Interactions

Poster presentation/Piešany, Slovakia, 2024.23-25.05.

A Computational Study of the Tropocollagen Hexamer and Heptamer.

4. [27]th Spring Wind Conference

Oral presentation/Budapest, Hungary, 2024.03-04.05

A Computational Study of Collagen Proline and Hydroxyproline.

5. Basics & Application of Computational Chemistry in Action (BACCA), Erasmus+ Blended Intensive Programme, virtual session

Oral presentation/Online, 2024.04.04

A Computational Protocol of Collagen Proline and Hydroxyproline.

6. MultiScience - XXXVIII. microCAD, International Multidisciplinary Scientific Conference. I. Innovations in sustainability

Oral presentation/Miskolc, Hungary, 2023.10.12

Molecular dynamics simulations of the proline and hydroxyproline of collagen.

7. Hungarian Science Day

Oral presentation/Miskolc, Hungary, 2023.11.14.

Molecular dynamics simulations of collagen molecules.

8. [11]th Visegrad Symposium on Biomolecular Interactions

Poster presentation/Szidonia Castle, Hungary, 2023.20-23.06.

Molecular Dynamics Simulations Of The Proline And Hydroxyproline Of Collagen.

9. [26]th Spring Wind Conference

Oral presentation/Miskolc, Hungary, 2023.05-07.05.

Molecular Dynamics Simulations Of The Hexameric And Heptameric Forms of Collagen.

10. Hungarian Science Day

Oral presentation/Miskolc, Hungary, 2022.11.09.

Investigating Biomaterials for Wound-Healing.

References

[1] Ma X. The Analysis of the Development and Application Prospects of Nanomaterials. *Applied and Computational Engineering.* 2025; 122(1):8-12. https://doi.org/10.54254/2755-2721/122/2025.19572.

[2] Khude P. Nanofibers for High Efficiency Filtration. *Journal of Material Science & Engineering.* 2017; 6(6). https://doi.org/10.4172/2169-0022.1000399.

[3] Kannan B, Cha H, Hosie IC. Electrospinning—Commercial Applications, Challenges and Opportunities. *Nano-size Polymers.* 2016; pp. 309-342. https://doi.org/10.1007/978-3-319-39715-3_11.

[4] Sharma A, Sharma RK, Nunzi JM, Mahajan A, Sharma DP, Pathak D. Electrospun Polymer Nanofibers for Technology Applications: A Short Review. *Current Materials Science.* 2023; 16(4): 376–399. https://doi.org/10.2174/2666145416666230104104150.

[5] Rasouli R, Barhoum A, Bechelany M, Dufresne A. Nanofibers for Biomedical and Healthcare Applications. *Macromolecular bioscience*. 2019; 19(2). https://doi.org/10.1002/mabi.201800256.

[6] Tański T, Matysiak W, Jarka P. Introductory Chapter: Electrospinning-smart Nanofiber Mats. *Electrospinning Method Used to Create Functional Nanocomposite Films.* InTech, 2018. https://doi.org/10.5772/intechopen.77198.

[7] Zhong H, Huang J, Wu J, Du J. Electrospinning nanofibers to 1D, 2D, and 3D scaffolds and their biomedical applications. *Nano Res.* 2022; 15: 787–804. https://doi.org/10.1007/s12274-021-3593-7.

[8] Gugulothu D, Barhoum A, Afzal SM, Venkateshwarlu B, Uludag H. Structural Multifunctional Nanofibers and Their Emerging Applications. *Handbook of Nanofibers*. *Springer*, 2019, 693–732. https://doi.org/10.1007/978-3-319-53655-2_16.

[9] Reddy MSB, Ponnamma D, Choudhary R, Sadasivuni KK. A Comparative Review of Natural and Synthetic Biopolymer Composite Scaffolds. *Polymers*. 2021; *13*(7). https://doi.org/10.3390/polym13071105.

[10] Miele D, Catenacci L, Rossi S, Sandri G, Sorrenti M, Terzi A, Giannini C, Riva F, Ferrari F, Caramella C, Bonferoni MC. Collagen/PCL Nanofibers Electrospun in Green Solvent by DOE Assisted Process. An Insight into Collagen Contribution. *Materials.* 2020; *13*(21):1–24. https://doi.org/10.3390/ma13214698.

[11] Fu W, Liu Z, Feng B, Hu R, He X, Wang H, Yin M, Huang H, Zhang H, Wang W. Electrospun gelatin/PCL and collagen/PLCL scaffolds for vascular tissue engineering. *International journal of nanomedicine*. 2014; 9(1): 2335–2344. https://doi.org/10.2147/IJN.S61375.

[12] Wang XC, Li X. Core-shell structured nanocomposites with electromagnetic properties. *Advanced Materials Research.* 2013; 607–612. https://doi.org/10.4028/www.scientific.net/AMR.785-786.607.

[13] Zou L, Gan L, Lv R, Wang M, Huang Z, Kang F, Shen W. A film of porous carbon nanofibers that contain Sn/SnOx nanoparticles in the pores and its electrochemical performance as an anode material for lithium ion batteries. *Carbon*. 2011; 49(1): 89–95. https://doi.org/10.1016/j.carbon.2010.08.046.

[14] Zhang K, Wang X, Yang Y, Wang L, Zhu M, Hsiao BS, Chu B. Aligned and molecularly oriented semihollow ultrafine polymer fiber yarns by a facile method. *J Polym Sci B Polym Phys.* 2010; 48(10): 1118–1125. https://doi.org/10.1002/polb.22003.

[15] Wei Q, Xia X. Types and processing of structured functional nanofibers: Core-shell, aligned, porous and gradient nanofibers. Functional Nanofibers and their Applications. 2012; 22–37. https://doi.org/10.1533/9780857095640.1.22.

[16] Matsuda T, Kawahara D. Electrospinning fabrication of high-trackable catheter tip with gradually graded or gradient flexibility. *Journal of biomedical materials research. Part B, Applied biomaterials*. 2008; *87*(1): 35–41. https://doi.org/10.1002/jbm.b.31061.

[17] Liu Y, Goebl J, Yin Y. Templated synthesis of nanostructured materials. *Chem Soc Rev.* 2013; 42(7): 2610–2653. https://doi.org/10.1039/C2CS35369E.

[18] Dahlin RL, Kasper FK, Mikos AG. Polymeric nanofibers in tissue engineering. *Tissue Eng Part B Rev*. 2011;17(5):349-364. https://doi.org/10.1089/ten.TEB.2011.0238.

[19] Shahi H, Kaur J, Vaidya S. Designing Nanostructured Materials through Self-Assembly and their Applications. *J. Inst. Eng. India Ser. C* 103, 2022; 135–142. https://doi.org/10.1007/s40032-021-00660-4.

[20] Guo Y, Wang X, Shen Y, Dong K, Shen L, Alzalab, AAA. Research progress, models and simulation of electrospinning technology: a review. *Journal of materials science*. 2022; *57*(1): 58–104. https://doi.org/10.1007/s10853-021-06575-w.

[21] Yoon K, Hsiao BS, Chu B. Functional nanofibers for environmental applications. *J Mater Chem.* 2008;18(44): 5326–5334. https://doi.org/10.1039/B804128H.

[22] Chinnappan A, Baskar C, Baskar S, Ratheesh G, Ramakrishna S. An overview of electrospun nanofibers and their application in energy storage, sensors and wearable/flexible electronics. *Journal of Materials Chemistry C*. 2017; 5, 12657-12673. https://doi.org/10.1039/C7TC03058D.

[23] Lu P, Murray S, Zhu M. Electrospun nanofibers for catalysts. in *Electrospinning: Nanofabrication and Applications.* 2019; pp. 695–717. https://doi.org/10.1016/B978-0-323-51270-1.00023-6.

[24] Maduna L, Patnaik A. Challenges Associated with the Production of Nanofibers. *Processes.* 2024; 12(10):2100. https://doi.org/10.3390/pr12102100.

[25] He H, Shi X, Chen W, Chen R, Zhao C, Wang S. Temperature/pH Smart Nanofibers with Excellent Biocompatibility and Their Dual Interactions Stimulus-Responsive Mechanism. *Journal of agricultural and food chemistry*. 2020; *68*(28): 7425–7433. https://doi.org/10.1021/acs.jafc.0c01493.

[26] Abadi B, Goshtasbi N, Bolourian S, Tahsili J, Adeli-Sardou M, Forootanfar H. Electrospun hybrid nanofibers: Fabrication, characterization, and biomedical applications. *Frontiers Media S.A.* 2022; 10. https://doi.org/10.3389/fbioe.2022.986975.

[27] Ghosh A, Orasugh JT, Ray SS, Chattopadhyay D. Integration of 3D Printing-Coelectrospinning: Concept Shifting in Biomedical Applications. *ACS omega*, 2023; *8*(31): 28002–28025. https://doi.org/10.1021/acsomega.3c03920.

[28] Thomas S, Seufert B, Serrano-Garcia W, Devisetty M, Khan R, Puttananjegowda K, Alcantar N. Eco-friendly, biodegradable, and biocompatible electrospun nanofiber membranes and applications. in *Sustainable Nanotechnology: Strategies, Products, and Applications*, 2022; pp. 173–199. https://doi.org/10.1002/9781119650294.ch11.

[29] Salazar-Brann SA, Patiño-Herrera R, Navarrete-Damián J, Louvier-Hernández JF. Electrospinning of chitosan from different acid solutions. *AIMS Bioeng. 2021; 8(1):*112–129. https://doi.org/10.3934/bioeng.2021011.

[30] Uhljar LÉ, Ambrus R. Electrospinning of Potential Medical Devices (Wound Dressings, Tissue Engineering Scaffolds, Face Masks) and Their Regulatory Approach. *Pharmaceutics*. 2023; 15(2):417. https://doi.org/10.3390/pharmaceutics15020417.

[31] Tamilarasi GP, Sabarees G, Manikandan K, Gouthaman S, Alagarsamy V, Solomon VR. Advances in electrospun chitosan nanofiber biomaterials for biomedical applications. *Royal Society of Chemistry.* 2023; 4(15): 3114-3139. https://doi.org/10.1039/d3ma00010a.

[32] Kilic A, Oruc F, Demir A. Effects of Polarity on Electrospinning Process. *Textile Research Journal*. 2008;78(6):532-539. https://doi.org/10.1177/0040517507081296.

[33] Jirsák J, Moučka F, Nezbeda I. Insight into electrospinning via molecular simulations. *Ind Eng Chem Res.* 2014; 53(19): 8257–8264. https://doi.org/10.1021/ie404268f.

[34] Aliheidari N, Aliahmad N, Agarwal M, Dalir H. Electrospun Nanofibers for Label-Free Sensor Applications. *Sensors*. 2019; 19(16):3587. https://doi.org/10.3390/s19163587.

[35] Bhattacharjee PK, Rutledge GC. Electrospinning and polymer nanofibers: Process fundamentals. in *Comprehensive Biomaterials. 2011; pp. 497–512. https://doi.org/10.1016/B978-0-08-055294-1.00039-8*.

[36] Teo WE, Ramakrishna S. Electrospun nanofibers as a platform for multifunctional, hierarchically organized nanocomposite. *Composites Science and Technology*. 2009; 69: 1804-1817. https://doi.org/10.1016/j.compscitech.2009.04.015.

[37] Thompson CJ, Chase GC, Yarin AL, Reneker DH. Effects of parameters on nanofiber diameter determined from electrospinning model. *Polymer.* 2007; 48(23): 6913–6922. https://doi.org/10.1016/j.polymer.2007.09.017.

[38] Fong H, Chun I, Reneker DH. Beaded nanofibers formed during electrospinning. *Polymer*. 1999; 40(16): 4585-4592. https://doi.org/10.1016/S0032-3861(99)00068-3.

[39] Kriegel C, Arecchi A, Kit K, McClements DJ, Weiss J. Fabrication, functionalization, and application of electrospun biopolymer nanofibers. *Crit Rev Food Sci Nutr*. 2008; 48(8): 775-797. https://doi.org/10.1080/10408390802241325.

[40] Kohse S, Grabow N, Schmitz K-P, Eickner T. Electrospinning of polyimide nanofibres–effects of working parameters on morphology. *Current Direct Biomed Eng*. 2017; 3(2): 687–690. https://doi.org/10.1515/cdbme-2017-0145.

[41] Luzio A, Canesi EV, Bertarelli C, Caironi M. Electrospun Polymer Fibers for Electronic Applications. *Materials*. 2014; 7(2): 906-947. https://doi.org/10.3390/ma7020906.

[42] Doshi J, Reneker DH. Electrospinning process and applications of electrospun fibers. *Journal of Electrostatics*. 1995; 35: 151-160. https://doi.org/10.1016/0304-3886(95)00041-8.

[43] Liu G, Gu Z, Hong Y, Cheng L, Li C. Electrospun starch nanofibers: Recent advances, challenges, and strategies for potential pharmaceutical applications. *Journal of Controlled Release*. 2017; 252: 95-107. https://doi.org/10.1016/j.jconrel.2017.03.016.

[44] Choi S, Kim HR, Jeong YK, Bang JY, Kim HS. Mechanism of Electrospinning for Poly(amic acid)/Polyacrylonitrile Fiber Fabrication. *Journal of Macromolecular Science, Part B*, 2018; 57(3): 222–230. https://doi.org/10.1080/00222348.2018.1441221.

[45] Hayati I, Bailey AI, Tadros TF. Investigations into the mechanisms of electrohydrodynamic spraying of liquids: I. Effect of electric field and the environment on pendant drops and factors affecting the formation of stable jets and atomization. *Journal of Colloid and Interface Science*. 1987; 117(1): 205-221. https://doi.org/10.1016/0021-9797(87)90185-8.

[46] Bhardwaj N, Kundu SC. Electrospinning: a fascinating fiber fabrication technique. *Biotechnol Adv*. 2010; 28(3): 325-347. https://doi.org/10.1016/j.biotechadv.2010.01.004.

[47] De Vrieze S, Van Camp T, Nelvig A, Hagström B, Westbroek P, De Clerck K. The effect of temperature and humidity on electrospinning. *J Mater Sci. 2009;* **44(5)**: 1357–1362. https://doi.org/10.1007/s10853-008-3010-6.

[48] Vega-Lugo AC, Lim LT. Effects of poly(ethylene oxide) and pH on the electrospinning of whey protein isolate. *J Polym Sci B Polym Phys.* 2012; 50(16): 1188–1197. https://doi.org/10.1002/polb.23106.

[49] Lu C, Chen P, Li J, Zhang Y. Computer simulation of electrospinning. Part I. Effect of solvent in electrospinning. *Polymer.* 2006; 47(3): 915–921. https://doi.org/10.1016/j.polymer.2005.11.090.

[50] Sill TJ, von Recum HA. Electrospinning: applications in drug delivery and tissue engineering. *Biomaterials*. 2008; 29(13): 1989-2006. https://doi.org/10.1016/j.biomaterials.2008.01.011.

[51] Yuan XY, Zhang YY, Dong C, Sheng J. Morphology of ultrafine polysulfone fibers prepared by electrospinning. *Polym Int.* 2004; 53(11): 1704–1710. https://doi.org/10.1002/pi.1538.

[52] Megelski S, Stephens JS, Bruce Chase D, Rabolt JF. Micro- and nanostructured surface morphology on electrospun polymer fibers. *Macromolecules. 2002; 35(22): 8456–8466. https://doi.org/10.1021/ma020444a*.

[53] Yang GZ, Li HP, Yang JH, Wan J, Yu DG. Influence of Working Temperature on The Formation of Electrospun Polymer Nanofibers. *Nanoscale Res Lett*. 2017; 12(1): 55. https://doi.org/10.1186/s11671-016-1824-8.

[54] Huang C, Thomas NL. Fabricating porous poly(lactic acid) fibres via electrospinning. *Eur Polym J.* 2018; 99:464–476. https://doi.org/10.1016/j.eurpolymj.2017.12.025.

[55] Taylor GI. Electrically driven jets. *Proc. R. Soc. Lond*. 1969; A313: 453–475 http://doi.org/10.1098/rspa.1969.0205.

[56] Yarin AL, Koombhongse S, Reneker DH. Taylor cone and jetting from liquid droplets in electrospinning of nanofibers. *J Appl Phys.* 2001; 90(9): 4836–4846. http://doi.org/10.1063/1.1408260.

[57] Wang Q, Wang Z, Yang S, Li B, Xu H, Yu K, Wang J. Experimental study on electrohydrodynamic atomization (EHDA) in stable cone-jet with middle viscous and low conductive liquid. *Experimental Thermal and Fluid Science.* 2021; 121. 110260. https://doi.org/10.1016/j.expthermflusci.2020.110260.

[58] Shin YM, Hohman MM, Brenner MP, Rutledge GC. Experimental characterization of electrospinning: the electrically forced jet and instabilities. *Polymer*. 2001; 42(25): 09955-09967. https://doi.org/10.1016/S0032-3861(01)00540-7.

[59] Baji A, Mai YW, Wong SC, Abtahi M, Chen P. Electrospinning of polymer nanofibers: Effects on oriented morphology, structures and tensile properties. *Composites Science and Technology*. 2010; 70(5): 703-718. https://doi.org/10.1016/j.compscitech.2010.01.010.

[60] Allen MP, Dominic JT, Computer Simulation of Liquids, 2nd edn (Oxford, 2017; online edn, Oxford Academic, 23 Nov. 2017), https://doi.org/10.1093/oso/9780198803195.001.0001,

[61] Danwanichakul P, Danwanichakul D. Two-dimensional simulation of electrospun nanofibrous structures: Connection of experimental and simulated results. *J Chem.* 2014; https://doi.org/10.1155/2014/479139.

[62] Sarmadi M, Shamloo A, Mohseni M. Utilization of Molecular Dynamics Simulation Coupled with Experimental Assays to Optimize Biocompatibility of an Electrospun PCL/PVA Scaffold. *PLoS One*. 2017; 12(1): e0169451. https://doi.org/10.1371/journal.pone.0169451.

[63] Vao-soongnern V. Monte Carlo simulation of molecular and structural properties of mono- and bi-dispersed poly(ethylene oxide) nanofibers. *J Polym Res*. 2019; 26(6): 147. https://doi.org/10.1007/s10965-019-1753-1.

[64] Steffens L, Morás AM, Arantes PR, Masterson K, Cao Z, Nugent M, Moura DJ. Electrospun PVA-Dacarbazine nanofibers as a novel nano brain-implant for treatment of glioblastoma: in silico and in vitro characterization. *Eur J Pharm Sci*. 2020; 143: 105183. https://doi.org/10.1016/j.ejps.2019.105183.

[65] Sarkar K, Ben Ghalia M, Wu Z, Bose SC. A neural network model for the numerical prediction of the diameter of electro-spun polyethylene oxide nanofibers. *J Mater Process Technol. 2009; 209(7):* 3156–3165. https://doi.org/10.1016/j.jmatprotec.2008.07.032.

[66] Kanjanapongkul K, Wongsasulak S, Yoovidhya T. Investigation and prevention of clogging during electrospinning of zein solution. *J Appl Polym Sci.* 2010; 118(3): 1821–1829. https://doi.org/10.1002/app.32499.

[67] Liu H, Gough CR, Deng Q, Gu Z, Wang F, Hu X. Recent Advances in Electrospun Sustainable Composites for Biomedical, Environmental, Energy, and Packaging Applications. *International Journal of Molecular Sciences*. 2020; 21(11): 4019. https://doi.org/10.3390/ijms21114019.

[68] Hosseini Ravandi SA, Sadrjahani M, Valipouri A, Dabirian F, Ko FK. Recently developed electrospinning methods: a review. *Textile Research Journal*. 2022; 92(23-24): 5130-5145. https://doi.org/10.1177/00405175211069880.

[69] Chaparro AM, Conde JJ, Reneker DH, Chun I. A Comparative Study of Electrospray and Airbrushing Processes for Deposition of Catalyst Layers. *Abstr.* 2019; https://doi.org/10.1149/MA2019-02/32/1448.

[70] Wang L, Ryan AJ. Introduction to electrospinning. In *Electrospinning for Tissue Regeneration.* 2011; 3-33. https://doi.org/10.1533/9780857092915.1.3.

[71] Kirkness MW, Lehmann K, Forde NR. Mechanics and structural stability of the collagen triple helix. *Curr Opin Chem Biol*. 2019; 53: 98-105. https://doi.org/10.1016/j.cbpa.2019.08.001.

[72] Yu Z, An B, Ramshaw JA, Brodsky B. Bacterial collagen-like proteins that form triple-helical structures. *J Struct Biol*. 2014; 186(3): 451-461. https://doi.org/10.1016/j.jsb.2014.01.003.

[73] Kar K, Ibrar S, Nanda V, Getz TM, Kunapuli SP, Brodsky B. Aromatic interactions promote self-association of collagen triple-helical peptides to higher-order structures. *Biochemistry*. 2009; 48(33): 7959-7968. https://doi.org/10.1021/bi900496m.

[74] Jenkins CL, Bretscher LE, Guzei IA, Raines RT. Effect of 3-hydroxyproline residues on collagen stability. *J Am Chem Soc*. 2003; 125(21): 6422-6427. https://doi.org/10.1021/ja034015j.

[75] Walker JM. Methods in Molecular Biology. *Springer Nature.* https://link.springer.com/series/7651.

[76] Liu X, Zheng C, Luo X, Wang X, Jiang H. Recent advances of collagen-based biomaterials: Multi-hierarchical structure, modification and biomedical applications. *Mater Sci Eng C Mater Biol Appl*. 2019; 99:1509-1522. https://doi.org/10.1016/j.msec.2019.02.070.

[77] Sorushanova A, Coentro JQ, Pandit A, Zeugolis DI, Raghunath M. Collagen: Materials Analysis and Implant Uses. *Comprehensive Biomaterials,* 2017*; 2*: 332-350. https://doi.org/10.1016/B978-0-12-803581-8.10155-9.

[78] Orgel JP, Irving TC, Miller A, Wess TJ. Microfibrillar structure of type I collagen in situ. *Proc Natl Acad Sci U S A*. 2006; 103(24): 9001-9005. https://doi.org/10.1073/pnas.0502718103.

[79] Eyre DR. The collagens of articular cartilage. *Semin Arthritis Rheum*. 1991; 21(3 Suppl 2): 2-11. https://doi.org/10.1016/0049-0172(91)90035-x.

[80] Coppola D, Oliviero M, Vitale GA, Lauritano C, D'Ambra I, Iannace S, de Pascale D. Marine Collagen from Alternative and Sustainable Sources: Extraction, Processing and Applications. *Marine Drugs*. 2020; 18(4): 214. https://doi.org/10.3390/md18040214.

[81] Hulmes DJ. Building collagen molecules, fibrils, and suprafibrillar structures. *J Struct Biol*. 2002; 137(1-2): 2-10. https://doi.org/10.1006/jsbi.2002.4450.

[82] Gordon MK, Gerecke DR, Olsen BR. Type XII collagen: distinct extracellular matrix component discovered by cDNA cloning. *Proc Natl Acad Sci U S A*. 1987; 84(17): 6040-6044. https://doi.org/10.1073/pnas.84.17.6040.

[83] Sasaki N, Shukunami N, Matsushima N, Izumi Y. Time-resolved X-ray diffraction from tendon collagen during creep using synchrotron radiation. *J Biomech*. 1999; 32(3): 285-292. https://doi.org/10.1016/s0021-9290(98)00174-2.

[84] Wess T. Collagen Fibrillar Structure and Hierarchies. In: *Fratzl, P. (eds) Collagen. Springer, Boston, MA*. 2008. https://doi.org/10.1007/978-0-387-73906-9_3.

[85] Fratzl P, Misof K, Zizak I, Rapp G, Amenitsch H, Bernstorff S. Fibrillar structure and mechanical properties of collagen. *J Struct Biol*. 1998; 122(1-2): 119-122. https://doi.org/10.1006/jsbi.1998.3966.

[86] Calejo MT, Almeida AJ, Fernandes AI. Exploring a new jellyfish collagen in the production of microparticles for protein delivery. *J Microencapsul*. 2012; 29(6): 520-531. https://doi.org/10.3109/02652048.2012.665089.

[87] Dong B, Arnoult O, Smith ME, Wnek GE. Electrospinning of collagen nanofiber scaffolds from benign solvents. *Macromol Rapid Commun*. 2009; 30(7): 539-542. https://doi.org/10.1002/marc.200800634.

[88] Wakuda Y, Nishimoto S, Suye Si, Fujita S. Native collagen hydrogel nanofibres with anisotropic structure using core-shell electrospinning. *Sci Rep* **8**, 2018; 6248. https://doi.org/10.1038/s41598-018-24700-9.

[89] Jiang Q, Reddy N, Zhang S, Roscioli N, Yang Y. Water-stable electrospun collagen fibers from a non-toxic solvent and crosslinking system. *J Biomed Mater Res A*. 2013; 101(5):1237-1247. https://doi.org/10.1002/jbm.a.34422.

[90] Gough JE, Scotchford CA, Downes S. Cytotoxicity of glutaraldehyde crosslinked collagen/poly(vinyl alcohol) films is by the mechanism of apoptosis. *J Biomed Mater Res*. 2002; 61(1):121-130. https://doi.org/10.1002/jbm.10145.

[91] Drexler JW, Powell HM. Dehydrothermal crosslinking of electrospun collagen. *Tissue Eng Part C Methods*. 2011; 17(1): 9-17. https://doi.org/10.1089/ten.TEC.2009.0754.

[92] Eckes S, Braun J, Wack JS, Ritz U, Nickel D, Schmitz K. Rose Bengal Crosslinking to Stabilize Collagen Sheets and Generate Modulated Collagen Laminates. *Int J Mol Sci*. 2020; 21(19): 7408. https://doi.org/10.3390/ijms21197408.

[93] Kumar D, Shahid M. Natural materials and products from insects: Chemistry and applications. *Springer International Publishing*, 2020. https://doi.org/10.1007/978-3-030-36610-0.

[94] Morin-Crini N, Lichtfouse E, Torri G, Crini G. Fundamentals and Applications of Chitosan. In: Crini G, Lichtfouse E. (eds) Sustainable Agriculture Reviews 35. *Sustainable Agriculture Reviews*, 2019; 35. Springer, Cham. https://doi.org/10.1007/978-3-030-16538-3_2.

[95] Li B, Mu X. Recent Progress in the Utilization of Chitin/Chitosan for Chemicals and Materials. *Fuels, Chemicals and Materials from the Oceans and Aquatic Sources.* 2017; 151-187. https://doi.org/10.1002/9781119117193.ch7.

[96] Aranaz I, Mengíbar M, Harris R, Panos I. Functional Characterization of Chitin and Chitosan. *Current Chemical Biology*. 2009; 3(2): 203-230. https://doi.org/10.2174/187231309788166415.

[97] Alvarenga ES. Characterization and Properties of Chitosan. in *Biotechnology of Biopolymers*, InTech, 2011. https://doi.org/10.5772/17020.

[98] Sivashankari PR, Prabaharan M. Deacetylation modification techniques of chitin and chitosan. in *Chitosan Based Biomaterials: Fundamentals: Volume 1.* 2017; 117-133. https://doi.org/10.1016/B978-0-08-100230-8.00005-4.

[99] Ujang Z, Diah M, Hazri A, Rashid A, Halim AS. The Development, Characterization and Application of Water Soluble Chitosan. In *Biotechnology of Biopolymers.* 2011. https://doi.org/10.5772/16771.

[100] Lizardi-Mendoza J, Argüelles Monal WM, Goycoolea Valencia FM. Chemical Characteristics and Functional Properties of Chitosan. in *Chitosan in the Preservation of Agricultural Commodities.* 2016; pp. 3–31. https://doi.org/10.1016/B978-0-12-802735-6.00001-X.

[101] Akpan EI, Gbenebor OP, Adeosun SO, Cletus O. Solubility, degree of acetylation, and distribution of acetyl groups in chitosan. in *Handbook of Chitin and Chitosan: Volume 1: Preparation and Properties.* 2020; pp. 131–164. https://doi.org/10.1016/B978-0-12-817970-3.00005-5.

[102] Muzzarelli RAA. Biomedical Exploitation of Chitin and Chitosan via Mechano-Chemical Disassembly, Electrospinning, Dissolution in Imidazolium Ionic Liquids, and Supercritical Drying. *Marine Drugs*. 2011; 9(9):1510-1533. https://doi.org/10.3390/md9091510.

[103] Singla AK, Chawla M. Chitosan: some pharmaceutical and biological aspects--an update. *J Pharm Pharmacol*. 2001; 53(8): 1047-1067. https://doi.org/10.1211/0022357011776441.

[104] Mawazi SM, Kumar M, Ahmad N, Ge Y, Mahmood S. Recent Applications of Chitosan and Its Derivatives in Antibacterial, Anticancer, Wound Healing, and Tissue Engineering Fields. *Polymers*. 2024; 16(10):1351. https://doi.org/10.3390/polym16101351.

[105] Merzendorfer, H. Chitosan Derivatives and Grafted Adjuncts with Unique Properties. In: Cohen, E., Merzendorfer, H. (eds) Extracellular Sugar-Based Biopolymers Matrices. *Biologically-Inspired Systems*, 2019; 12. https://doi.org/10.1007/978-3-030-12919-4_3.

[106] Wang X, Guan J, Zhuang X, Li Z, Huang S, Yang J, Liu C, Li F, Tian F, Wu J, Shu Z. Exploration of Blood Coagulation of N-Alkyl Chitosan Nanofiber Membrane in Vitro. *Biomacromolecules.* 2018;19(3) :731-739. https://doi.org/10.1021/acs.biomac.7b01492.

[107] Fonseca-Santos B, Chorilli M. An overview of carboxymethyl derivatives of chitosan: Their use as biomaterials and drug delivery systems. *Materials Science and Engineering: C*. 2017; 77: 1349-1362. https://doi.org/10.1016/j.msec.2017.03.198.

[108] Tan H, Ma R, Lin C, Liu Z, Tang T. Quaternized Chitosan as an Antimicrobial Agent: Antimicrobial Activity, Mechanism of Action and Biomedical Applications in Orthopedics. International *Journal of Molecular Sciences*. 2013; 14(1):1854-1869. https://doi.org/10.3390/ijms14011854.

[109] Ibrahim HM, El-Zairy EMR. Chitosan as a Biomaterial — Structure, Properties, and Electrospun Nanofibers. in *Concepts, Compounds and the Alternatives of Antibacterials.* 2015; https://doi.org/10.5772/61300.

[110] Salas C, Thompson Z, Bhattarai N. Electrospun chitosan fibers. in *Electrospun Nanofibers.* 2017; pp. 371–398. https://doi.org/10.1016/B978-0-08-100907-9.00015-5.

[111] De Vrieze S, Westbroek P, Van Camp T, Van Langenhove L. Electrospinning of chitosan nanofibrous structures: feasibility study. *J Mater Sci.* 2007*;* 42, 8029–8034. https://doi.org/10.1007/s10853-006-1485-6.

[112] Homayoni H, Ravandi SAH, Valizadeh M. Electrospinning of chitosan nanofibers: Processing optimization. *Carbohydr Polym,* 2009; 77(3): 656–661. https://doi.org/10.1016/j.carbpol.2009.02.008.

[113] Sharma S, Kumar P, Chandra R. Applications of BIOVIA Materials Studio, LAMMPS, and GROMACS in Various Fields of Science and Engineering. In Molecular Dynamics Simulation of Nanocomposites Using BIOVIA Materials Studio, Lammps and Gromacs. *Micro and Nano Technologies.* 2019; 329-341. https://doi.org/10.1016/B978-0-12-816954-4.00007-3.

[114] González MA. Force fields and molecular dynamics simulations. *Collect*. SFN 2011; 12: 169-200. http://dx.doi.org/10.1051/sfn/201112009.

[115] Izadi S, Onufriev AV. Accuracy limit of rigid 3-point water models. *J Chem Phys*. 2016; 145(7):074501. https://doi.org/10.1063/1.4960175.

[116] Singh A, Vanga SK, Orsat V, Raghavan V. Application of molecular dynamic simulation to study food proteins: A review. *Crit Rev Food Sci Nutr*. 2018; 58(16):2779-2789. https://doi.org/10.1080/10408398.2017.1341864.

[117] Miao J, Hodgson KO, Sayre D. An approach to three-dimensional structures of biomolecules by using single-molecule diffraction images. *Proc Natl Acad Sci U S A*. 2001; 98(12):6641-6645. https://doi.org/10.1073/pnas.111083998.

[118] Kroemer RT. Structure-based drug design: docking and scoring. *Curr Protein Pept Sci*. 2007; 8(4):312-328. https://doi.org/10.2174/138920307781369382.

[119] Thambiliyagodage C, Jayanetti M, Mendis A, Ekanayake G, Liyanaarachchi H, Vigneswaran S. Recent Advances in Chitosan-Based Applications—A Review. *Materials*. 2023; 16(5): 2073. https://doi.org/10.3390/ma16052073.

[120] Visser D, Rogg K, Fuhrmann E, Marzi J, Schenke-Layland K, Hartmann H. Electrospinning of collagen: enzymatic and spectroscopic analyses reveal solvent-independent disruption of the triple-helical structure. *Journal of Materials Chemistry B.* 2023; 2207-2218. https://doi.org/10.1039/D2TB02602C.

[121] Mauricio J, Mancipe A, Marcos LD, Rossana Mara da Silva MT. Type I collagen – poly(vinyl alcohol) electrospun nanofibers: FTIR study of the collagen helical structure preservation. *Polymer-Plastics Technology and Materials.* 2022; 61(8): 846–860. https://doi.org/10.1080/25740881.2022.2029887.

[122] Bürck J, Heissler S, Geckle U, Ardakani MF, Schneider R, Ulrich AS, Kazanci M. Resemblance of electrospun collagen nanofibers to their native structure. *Langmuir*. 2013; 29(5):1562-1572. https://doi.org/10.1021/la3033258.

[123] Abraham LC, Zuena E, Perez-Ramirez B, Kaplan DL. Guide to collagen characterization for biomaterial studies. *J Biomed Mater Res B Appl Biomater*. 2008; 87(1): 264-285. https://doi.org/10.1002/jbm.b.31078.

[124] Zhou Y, Li S, Wang D, Zhao Y, Lei X. Estimation of type i collagen structure dissolved in inorganical acids from circular dichroism spectra. *Bioscience Journal*. 2018; 34(3). https://doi.org/10.14393/BJ-v34n3a2018-39998.

[125] Vassaux M. Heterogeneous Structure and Dynamics of Water in a Hydrated Collagen Microfibril. *Biomacromolecules*. 2024; 25(8): 4809-4818. https://doi.org/10.1021/acs.biomac.4c00183.

[126] Gautieri A, Vesentini S, Redaelli A, Buehler MJ. Viscoelastic properties of model segments of collagen molecules. *Matrix Biol*. 2012; 31(2): 141-149. https://doi.org/10.1016/j.matbio.2011.11.005.

[127] Lees S, Pined M, Escoubes M. A generalized packing model for type I collagen. *International Journal of Biological Macromolecules*. 1984; 6(3): 133-136. https://doi.org/10.1016/0141-8130(84)90053-9.

[128] Franca EF, Freitas LC, Lins RD. Chitosan molecular structure as a function of N-acetylation. *Biopolymers*. 2011; 95(7): 448-460. https://doi.org/10.1002/bip.21602.

[129] Sogias IA, Khutoryanskiy VV, Williams AC. Exploring the factors affecting the solubility of chitosan in water. *Macromol Chem Phys.* 2010; 211(4): 426–433. https://doi.org/10.1002/macp.200900385.

[130] Romany A, Payne GF, Shen J. Effect of Acetylation on the Nanofibril Formation of Chitosan from All-Atom De Novo Self-Assembly Simulations. *Molecules*. 2024; 29(3):561. https://doi.org/10.3390/molecules29030561.

[131] Borca CH, Arango CA. Molecular Dynamics of a Water-Absorbent Nanoscale Material Based on Chitosan. *J Phys Chem B*. 2016; 120(15): 3754-3764. https://doi.org/10.1021/acs.jpcb.5b11230.

[132] Faria RR, Guerra RF, de Sousa Neto LR, Motta LF, Franca Ede F. Computational study of polymorphic structures of α- and β- chitin and chitosan in aqueous solution. *J Mol Graph Model*. 2016; 63: 78-84. https://doi.org/10.1016/j.jmgm.2015.11.001.

[133] Geng X, Kwon OH, Jang J. Electrospinning of chitosan dissolved in concentrated acetic acid solution. *Biomaterials*. 2005; 26(27): 5427-5432. https://doi.org/10.1016/j.biomaterials.2005.01.066.

[134] Karo Karo A, Giat Sukaryo S, Dwi Adistiana K, Dahlan K. Synthesis of Nanofiber from Poly Vinil Alcohol (PVA) Collagen. *Indonesian Journal of Applied Chemistry. 2020; 21(2): 55-65. https://doi.org/10.14203/jkti.v21i2.428*.

[135] Chikhaoui E, Cherif E, Ammar M, Chaste J, Bouville D, Herth E. Rheological and film-forming properties of carboxymethylcellulose and polyvinyl alcohol (CMC/PVA) mixtures. *J Mol Liq*. 2024; 421. https://doi.org/10.1016/j.molliq.2024.126819.

[136] Hu J, Li J, Jiang J, Wang L, Roth J, McGuinness KN, Baum J, Dai W, Sun Y, Nanda V, *et al*. Design of synthetic collagens that assemble into supramolecular banded fibers as a functional biomaterial testbed. *Nature communications*. 2022; 13(1):6761. https://doi.org/10.1038/s41467-022-34127-6.

[137] Aduri R, Psciuk BT, Saro P, Taniga H, Schlegel HB, SantaLucia J. AMBER Force Field Parameters for the Naturally Occurring Modified Nucleosides in RNA. *Journal of chemical theory and computation*. 2007; *3*(4):1464–1475. https://doi.org/10.1021/ct600329w.

[138] Jorgensen WL, Chandrasekhar J, Madura JD, Impey RW, Klein ML. Comparison of simple potential functions for simulating liquid water. *J Chem Phys*. 1983; 79(2):926–935. https://doi.org/10.1063/1.445869.

[139] Berk H, Bekker H, Berendsen HJC, Fraaije JGEM**.** LINCS: A Linear Constraint Solver for molecular simulations. *Article in Journal of Computational Chemistry*. 1998; 18(12):1463-1472. https://doi.org/10.1002/(SICI)1096-987X(199709)18:12%3C1463::AID-JCC4%3E3.0.CO;2-H.

[140] Nosé S. A unified formulation of the constant temperature molecular dynamics methods. *J Chem Phys*. 1984; 81(1):511–519. https://doi.org/10.1063/1.447334.

[141] Ke Q, Gong X, Liao S, Duan C, Li L. Effects of thermostats/barostats on physical properties of liquids by molecular dynamics simulations. *J Mol Liq*. 2022; 365:120116. https://doi.org/10.1016/j.molliq.2022.120116.

[142] Essmann U, Perera L, Berkowitz ML, Darden T, Lee H, Pedersen LG. A smooth particle mesh Ewald method. *J Chem Phys*. 1995; 103(19):8577–8593. https://doi.org/10.1063/1.470117.

[143] Hess B, Kutzner C, van der Spoel D, Lindahl E. GROMACS 4: Algorithms for Highly Efficient, Load-Balanced, and Scalable Molecular Simulation. *Journal of chemical theory and computation*. 2008; 4(3):435–447. https://doi.org/10.1021/ct700301q.

[144] Mukhopadhyay A. On Clustering using Gromos Algorithm on biased and unbiased trajectories followed by reweighting. Technical Report, Indian Institute of Technology Kanpur. 2022. http://dx.doi.org/10.13140/RG.2.2.10132.48007.

[145] Gorelov S, Titov A, Tolicheva O, Konevega A, Shvetsov A. Determination of Hydrogen Bonds in GROMACS: A New Implementation to Overcome Memory Limitation. *Journal of chemical information and modeling*. 2024; 64(16):6241–6246. https://doi.org/10.1021/acs.jcim.3c02087

[146] The Lekmul Lab Home Page. https://osf.io/3wunt.

[147] Yekeen AA, Durojaye OA, Idris MO, Muritala HF, Arise RO. CHAPERONg: A tool for automated GROMACS-based molecular dynamics simulations and trajectory analyses. *Computational and structural biotechnology journal*. 2023; 21:4849–4858. https://doi.org/10.1016/j.csbj.2023.09.024.

[148] Raman SS, Parthasarathi R, Subramanian V, Ramasami T. Role of length-dependent stability of collagen-like peptides. *The journal of physical chemistry. B*. 2008; 112(5):1533–1539. https://doi.org/10.1021/jp0728297.

[149] Andreeva LA, Myasoedov NF, Lyapina LA, Grigor'eva ME, Obergan TY, Shubina TA. Effect of the PRO-GLY-PRO peptide on hemostasis and lipid metabolism in rats with hypercholesterolemia. *Doklady Biological Sciences*. 2013; 453(1):333–335. https://doi.org/10.1134/S0012496613060069

[150] Improta R, Mele F, Crescenzi O, Benzi C, Barone V. Understanding the role of stereoelectronic effects in determining collagen stability. 2. A quantum mechanical/molecular mechanical study of (Proline-Proline-Glycine)n polypeptides. *J Am Chem Soc*. 2002; 124(26):7857–7865. https://doi.org/10.1021/ja020187p.

[151] Okuyama K, Kawaguchi T, Shimura M, Noguchi K, Mizuno K, Bächinger HP. Crystal structure of the collagen model peptide (Pro-Pro-Gly) 4-Hyp-Asp-Gly-(Pro-Pro-Gly)4 at 1.0 Å resolution. *Biopolymers*. 2013; 99(7): 436–447. https://doi.org/10.1002/bip.22198.

[152] Segrest JP, Cuwningham LW. Unit Fibril Models Derived from the Molecular Topography of Collagen. *Biopolymers.* 1973; 12(4):825-834. https://doi.org/10.1002/bip.1973.360120411.

[153] Sasisekharan V, Ramachandran GN. Studies on collagen. *Proc. Indian Acad. Sci.* 1957; 45:363–376. https://doi.org/10.1007/BF03052553.

[154] Orgel JP, San Antonio JD, Antipova O. Molecular and structural mapping of collagen fibril interactions. *Connective Tissue Research*, 2011; *52*(1): 2-17. https://doi.org/10.3109/03008207.2010.511353.

[155] Hulmes DJ, Miller A. Quasi-hexagonal molecular packing in collagen fibrils. *Nature*, 1979; *282*(5741): 878–880. https://doi.org/10.1038/282878a0.

[156] Xu S, Gu M, Wu K, Li G. Unraveling the Role of Hydroxyproline in Maintaining the Thermal Stability of the Collagen Triple Helix Structure Using Simulation. *The journal of physical chemistry. B*. 2019; 123(36): 7754–7763. https://doi.org/10.1021/acs.jpcb.9b05006.

[157] Deber CM, Brodsky B, Rath A. Proline Residues in Proteins. *Encyclopedia of Life Sciences*, Wiley. 2010; http://dx.doi.org/10.1002/9780470015902.a0003014.pub2.

[158] Melton SD, Brackhahn EAE, Orlin SJ, Jin P, Chenoweth DM. Rules for the design of aza-glycine stabilized triple-helical collagen peptides. *Chem Sci*. 2020; 11(39):10638–10646. https://doi.org/10.1039/D0SC03003A.

[159] Qi Y, Zhou D, Kessler JL, Qiu R, Yu SM, Li G, Qin Z, Li Y. Terminal repeats impact collagen triple-helix stability through hydrogen bonding. *Chem Sci*. 2022; 13(42):12567–12576. https://doi.org/10.1039/D2SC03666E.

[160] Ratnatilaka P, Eastwood JR, Qin Z, Kessler JL, Li Y, Whitby FG, Hill CP, Kirshenbaum K, Yu SM. Structural and Positional Effects of Peptoid Residues on Stability of the Collagen Triple Helix. *ChemRxiv*. 2024; https://doi.org/10.26434/chemrxiv-2024-pz51s.

[161] Wu X, Liu Y, Liu A, Wang W. Improved thermal-stability and mechanical properties of type I collagen by crosslinking with casein, keratin and soy protein isolate using transglutaminase. *International journal of biological macromolecules*. 2017; 98:292–301. https://doi.org/10.1016/j.ijbiomac.2017.01.127.

[162] Mitternacht S. FreeSASA: An open source C library for solvent accessible surface area calculations. *F1000Research*. 2016; 5:189. https://doi.org/10.12688/f1000research.7931.1.

[163] Raghunathan S. Solvent accessible surface area-assessed molecular basis of osmolyte-induced protein stability. *RSC Adv*. 2024; 14(34):25031–25041. https://doi.org/10.1039/D4RA02576H.

[164] Savojardo C, Manfredi M, Martelli PL, Casadio R. Solvent Accessibility of Residues Undergoing Pathogenic Variations in Humans: From Protein Structures to Protein Sequences. *Frontiers in molecular biosciences*. 2021; 7:626363. https://doi.org/10.3389/fmolb.2020.626363.

[165] Watanabe S, Tanimoto Y, Nishiwaki H, Watanabe Y. Identification and characterization of bifunctional proline racemase/hydroxyproline epimerase from archaea: discrimination of substrates and molecular evolution. *PloS one*. 2015; 10(3):e0120349. https://doi.org/10.1371/journal.pone.0120349.

[166] Schobert B, Tschesche H. Unusual solution properties of proline and its interaction with proteins. *Biochimica et biophysica acta*. 1978; 541(2):270–277.https://doi.org/10.1016/0304-4165(78)90400-2.

[167] Martínez L. Automatic identification of mobile and rigid substructures in molecular dynamics simulations and fractional structural fluctuation analysis. *PLOS ONE*. 2015; 10(3):e0119264. https://doi.org/10.1371/journal.pone.0119264.

[168] Chen YS, Chen CC, Horng JC. Thermodynamic and kinetic consequences of substituting glycine at different positions in a Pro-Hyp-Gly repeat collagen model peptide. *Peptide Science*. 2011; 96(1):60–68. https://doi.org/10.1002/bip.21470.

[169] Sankararamakrishnan R, Vishveshwara S. Conformational Studies on Peptides with Proline in the Right-Handed a-Helical Region. *Biopolymers.* 1990; 30(3-4):287-298 https://doi.org/10.1002/bip.360300307.

[170] Li T, Shen J, Wu L, Song Z, Lv S, Cai D, Zhang S, Guo T, Song S, Zhu M. Atomic-Scale Observation of Carbon Distribution in High-Performance Carbon-Doped Ge2Sb2Te5 and Its Influence on Crystallization Behavior. *Journal of Physical Chemistry C*. 2019; 123(21):13377–13384. https://doi.org/10.1021/acs.jpcc.9b02098.

[171] Mangaud E, Rotenberg B. Sampling mobility profiles of confined fluids with equilibrium molecular dynamics simulations. *The Journal of Chemical Physics*. 2020; 153(4):044125. https://doi.org/10.1063/5.0013952.

[172] Ulman K, Busch S, Hassanali AA. Quantum mechanical effects in zwitterionic amino acids: The case of proline, hydroxyproline, and alanine in water. *Journal of Chemical Physics*. 2018; 148(22): https://doi.org/10.1063/1.5008665.

[173] Radhakrishnan A, Vitalis A, Mao AH, Steffen AT, Pappu RV. Improved atomistic Monte Carlo simulations demonstrate that poly-l-proline adopts heterogeneous ensembles of conformations of semi-rigid segments interrupted by kinks. *Journal of Physical Chemistry B*. 2012; 116(23):6862–6871. https://doi.org/10.1021/jp212637r.

[174] Naziga EB, Schweizer F, Wetmore SD. Solvent interactions stabilize the polyproline II conformation of glycosylated oligoprolines. *Journal of Physical Chemistry B*. 2013; 117(9):2671–2681. https://doi.org/10.1021/jp312487v

[175] Lee D, Ko YC, Koo KT, Seol YJ. A Flexible Membrane May Improve Bone Regeneration by Increasing Hydrophilicity and Conformability in Lateral Bone Augmentation. *Biomaterials research.* 2024; 28: 0113. https://doi.org/10.34133/bmr.0113

[176] Freeman JW, Silver FH, Woods MD, Laurencin CT. The Role of Type I Collagen Molecular Structure in Tendon Elastic Energy Storage. *MRS Online Proceedings Library 874*. 2005; 16. https://doi.org/10.1557/PROC-874-L1.6

[177] Streeter I, de Leeuw NH. Atomistic modeling of collagen proteins in their fibrillar environment. *The journal of physical chemistry. B*. 2010; 114(41):13263–13270. https://doi.org/10.1021/jp1059984

[178] Bełdowski P, Przybyłek M, Bełdowski D. Dedinaite A, Sionkowska A, Cysewski P, Claesson PM. Collagen type II-hyaluronan interactions - the effect of proline hydroxylation: a molecular dynamics study. *J Mater Chem B*. 2022; 10(46):9713–9723, https://doi.org/10.1039/D2TB01550A

[179] Improta R, Berisio R, Vitagliano L. Contribution of dipole-dipole interactions to the stability of the collagen triple helix. *Protein science.* 2008; 17(5):955–961. https://doi.org/10.1110/ps.073301908

[180] Cramer J, Sager CP, Ernst B. Hydroxyl Groups in Synthetic and Natural-Product-Derived Therapeutics: A Perspective on a Common Functional Group. *American Chemical Society*. 2019; 62(20): 8915–8930. https://doi.org/10.1021/acs.jmedchem.9b00179

[181] Yang L. Mechanical properties of collagen fibrils and elastic fibers explored by AFM. [PhD Thesis - Research UT, graduation UT, University of Twente]. University of Twente, 2008, https://doi.org/10.3990/1.9789036526234.

[182] Jo S, Cheng X, Islam SM, Huang L, Rui H, Zhu A, Lee HS, Qi Y, Han W, Vanommeslaeghe K, *et al*. CHARMM-GUI PDB Manipulator for Advanced Modeling and Simulations of Proteins Containing Non-standard Residues. *Adv. Protein Chem. Struct. Biol.* 2014; 96: 235-265. https://doi.org/10.1016/bs.apcsb.2014.06.002.

[183] Huang J, MacKerell AD Jr. CHARMM36 all-atom additive protein force field: Validation based on comparison to NMR data. *J Comput Chem*. 2013; 34(25): 2135–2145. https://doi.org/10.1002/jcc.23354.

[184] Shalihah H, Kusumaatmaja A, Nugraheni AD, Triyana K. Optimization of chitosan/pva concentration in fabricating nanofibers membrane and its prospect as air filtration. *Materials Science Forum*. 2017; 901: 20–25. https://doi.org/10.4028/www.scientific.net/MSF.901.20.

[185] Ge JC, Wu G, Yoon SK, Kim MS, Choi NJ. Study on the Preparation and Lipophilic Properties of Polyvinyl Alcohol (PVA) Nanofiber Membranes via Green Electrospinning. *Nanomaterials*. 2021; 11(10): 2514. https://doi.org/10.3390/nano11102514.

[186] Chatterjee S, Salaün F, Campagne C, Vaupre S. Synthesis and characterization of chitosan droplet particles by ionic gelation and phase coacervation. *Polymer Bulletin*. 2014; 71(4): 1001–1013. https://doi.org/10.1007/s00289-014-1107-4.

[187] Bazrafshan Z, Stylios GK. A novel approach to enhance the spinnability of collagen fibers by graft polymerization. *Materials Science and Engineering C*. 2019; 94: 108–116. https://doi.org/10.1016/j.msec.2018.09.016.

[188] Awad TM, Mohammed MAS. The structural properties of the pure PVA nanopolymer. *Materials Today: Proceedings*. 2021; 47: 6035–6038. https://doi.org/10.1016/j.matpr.2021.04.610.

[189] Sacristan Bermejo J, Mijangos Ugarte C. Influence of water content on structure and mobility of polyvinyl alcohol: A molecular dynamics simulation. *Journal of Chemical Physics*. 2008; 129(15): 154907. http://dx.doi.org/10.1063/1.2994731.

[190] Shariatinia Z, Mazloom-Jalali A. Chitosan nanocomposite drug delivery systems designed for the ifosfamide anticancer drug using molecular dynamics simulations. *J Mol Liq*. 2019; 273: 346–367. https://doi.org/10.1016/j.molliq.2018.10.047.

[191] Tsai CC, Morrow BH, Chen W, Payne GF, Shen J. Toward Understanding the Environmental

Control of Hydrogel Film Properties: How Salt Modulates the Flexibility of Chitosan Chains. *Macromolecules*. 2017; 50(15): 5946–5952. https://doi.org/10.1021/acs.macromol.7b01116.

[192] Hajjari MM, Sharif N. In-silico behavior of dissolved prolamins under electric field effect applied by electrospinning process using molecular dynamics simulation. *J Mol Liq*. 2021; 344. https://doi.org/10.1016/j.molliq.2021.117778.

[193] Zhai C, Sullivan PA, Martin CL, Shi H, Deravi LF, Yeo J. Probing the alignment-dependent mechanical behaviors and time-evolutional aligning process of collagen scaffolds. *J Mater Chem B*. 2022; 10(36): 7052–7061. https://doi.org/10.1039/D2TB01360F.

[194] Feldman D. Poly(Vinyl Alcohol) Recent Contributions to Engineering and Medicine. *Journal of Composites Science*. 2020; 4(4):175. https://doi.org/10.3390/jcs4040175.

[195] Sun H, Feng Y, Lei B, Yin X, Wu B. Molecular simulation of the effects of water on the interface of plant fiber/polyvinyl alcohol (PVA) composites prepared by dry preparation method (DPM). *J Mol Liq*. 2023; 391. https://doi.org/10.1016/j.molliq.2023.123174.

[196] Fu ZZ, Guo SJ, Li CX, Wang K, Zhang Q, Fu Q. Hydrogen-bond-dominated mechanical stretchability in PVA films: From phenomenological to numerical insights. *Physical Chemistry Chemical Physics*. 2022; 24(3): 1885–1895. https://doi.org/10.1039/D1CP03893A.

[197] Mazeauj K, Winter WT, Chanzy H. Molecular and Crystal Structure of a High-Temperature Polymorph of Chitosan from Electron Diffraction Data. *Macromolecules.* 1994; 27(26). https://doi.org/10.1021/ma00104a015.

[198] Hu K, Kong M, Qin M, Zeng J, Ai B, Zhang J, Zhang H, Zhong F, Wang G, Zhuang L. Experimental and theoretical studies of chitosan dissolution in ionic liquids: Contribution ratio effect of cations and anions. *J Mol Liq*. 2021; 331. https://doi.org/10.1016/j.molliq.2021.115762.

[199] Ogawa Y, Naito PK, Nishiyama Y. Hydrogen-bonding network in anhydrous chitosan from neutron crystallography and periodic density functional theory calculations. *Carbohydr Polym*. 2019; 207: 211–217. https://doi.org/10.1016/j.carbpol.2018.11.042.

[200] Ramachandran GN, Chandrasekharan R. Interchain Hydrogen Bonds via Bound Water Molecules in the Collagen Triple Helix. *Biopolymers*. 1968; 6(11): 1649–1658. https://doi.org/10.1002/bip.1968.360061109.

[201] Balupuri A, Son DH, Sook Kang N. Investigating the effect of water on collagen triple helix stability. *J Mol Liq*. 2024; 415. https://doi.org/10.1016/j.molliq.2024.126325.

[202] Haugstad KE, Håti AG, Nordgård CT, Adl PS, Maurstad G, Sletmoen M, Draget KI, Dias RS, Stokke BT. Direct Determination of Chitosan–Mucin Interactions Using a Single-Molecule Strategy: Comparison to Alginate–Mucin Interactions. *Polymers*. 2015; 7(2): 161-185.https://doi.org/10.3390/polym7020161.

[203] Liu S, Li Q, Li G. Investigation of the solubility and dispersion degree of calf skin collagen in ionic liquids. *Journal of Leather Science and Engineering*. 2019; 1(1). https://doi.org/10.1186/s42825-019-0013-9.

[204] Christ HA, Menzel H. Electrospinning and Photocrosslinking of Highly Modified Fungal Chitosan. *Macromolecular Materials and Engineering*, 2022; 308(1), 2200430. https://doi.org/10.1002/mame.202200430.

[205] Mata GCd, Morais MS, Oliveira WPd, Aguiar ML. Composition Effects on the Morphology of PVA/Chitosan Electrospun Nanofibers. *Polymers*. 2022; 14(22):4856. https://doi.org/10.3390/polym14224856.

[206] Koosha M, Mirzadeh H. Electrospinning, mechanical properties, and cell behavior study of chitosan/PVA nanofibers. *J Biomed Mater Res A*. 2015;103(9):3081-3093. https://doi.org/10.1002/jbm.a.35443.

[207] Kan Y, Salimon AI, Korsunsky AM. On the electrospinning of nanostructured collagen-PVA fiber mats. *Materials Today: Proceedings*. 2020; 33(4): 2013-2019. https://doi.org/10.1016/j.matpr.2020.07.621.

[208] Syed MH, Khan MMR, Zahari MAKM, Beg MDH, Abdullah N. Current issues and potential solutions for the electrospinning of major polysaccharides and proteins: A review. *Int J Biol Macromol*. 2023;253(Pt 2):126735. https://doi.org/10.1016/j.ijbiomac.2023.126735.

[209] Arinstein A. Supermolecular Structure Formation During Electrospinning, and Its Effect on Electrospun Polymer Nanofiber Unique Features. 2019. In: Andrianov I, Manevich A, Mikhlin Y, Gendelman O. (eds) Problems of Nonlinear Mechanics and Physics of Materials. Advanced Structured Materials, vol 94. Springer, Cham. https://doi.org/10.1007/978-3-319-92234-8_11.

[210] Okuyama K, Noguchi K, Miyazawa T, Yui T, Ogawa K. Molecular and Crystal Structure of Hydrated Chitosan. *Macromolecules.* 1997; 30, 5849-5855. https://doi.org/10.1021/MA970509N.

[211] Coumoulos GD. The electron diffraction by amorphous polymers. *Proc.* 1943; 182 (989): 166–179. https://doi.org/10.1098/rspa.1943.0029

[212] Nikonovich GV, Burkhanova ND, Yunusov MY, Yugai SM, Milusheva RY, Voropaeva NL, Rashidova SS. Structural and physicochemical study of chitosan and polyvinylpyrrolidone blends. *Chem Nat Compd.* 2000; 36, 258–262. https://doi.org/10.1007/BF02238329.

[213] Baranauskas V, Vidal BC, Parizotto NA. Observation of geometric structure of collagen molecules by atomic force microscopy. *Appl Biochem Biotechnol. 1998;* 69, 91–97. https://doi.org/10.1007/BF02919391.

[214] Lan W, Xu M, Zhang X, Zhao L, Huang D, Wei, X, Chen W. Biomimetic polyvinyl alcohol/type II collagen hydrogels for cartilage tissue engineering. *J Biomater Sci Polym Ed*. 2020; 31(9):1179-1198. https://doi.org/10.1080/09205063.2020.1747184.

[215] Perumal S, Antipova O, Orgel JP. Collagen fibril architecture, domain organization, and triple-helical conformation govern its proteolysis. *Proc Natl Acad Sci U S A*. 2008; 105(8):2824-2829. https://doi.org/10.1073/pnas.0710588105.

[216] Tesei G, Paradossi G, Chiessi E. Influence of surface concentration on poly(vinyl alcohol) behavior at the water-vacuum interface: a molecular dynamics simulation study. *J Phys Chem B*. 2014; 118(24):6946-6955. https://doi.org/10.1021/jp502486a.

[217] Murali A, Sunil Kumar PB, Satapathy DK. Water vapor responsiveness of chitosan: An experimental and simulation analysis. *J. Chem. Phys.* 2024; 161, 144901. https://doi.org/10.1063/5.0226807.

[218] Malpani D, Majumder A, Samanta P, Srivastava RK, Nandan B. Supramolecular Route for Enhancing Polymer Electrospinnability. *ACS Omega*. 2018; 3(11):15666-15678. https://doi.org/10.1021/acsomega.8b02029.

[219] Anand BG, Dubey K, Shekhawat DS, Prajapati KP, Kar K. Strategically Designed Antifibrotic Gold Nanoparticles to Prevent Collagen Fibril Formation. *Langmuir*. 2017; 33(46):13252-13261. https://doi.org/10.1021/acs.langmuir.7b01504.

[220] Buslov DK, Sushko NI, Tretinnikov ON. IR investigation of hydrogen bonds in weakly hydrated films of poly(vinyl alcohol). *Polym. Sci. Ser. A.* 2011; 53, 1121–1127. https://doi.org/10.1134/S0965545X11120030.

[221] Gough CA, Anderson RW, Bhatnagar RS. The Role of Bound Water in the Stability of the Triple-Helical Conformation of $(Pro\text{-}Pro\text{-}Gly)_{10}$. *Journal of Biomolecular Structure and Dynamics*. 1998; *15*(6):1029–1037. https://doi.org/10.1080/07391102.1998.10508998.

[222] Krzeminski J, Molisak-tolwinska, H. The Structure of Water-Swollen Poly(Vinyl Alcohol) and the Swelling Mechanism. *Journal of Macromolecular Science: Part A – Chemistry*. 1991; *28*(3–4): 413–429. https://doi.org/10.1080/00222339108052151.

[223] Aliev AE, Courtier-Murias D. Water scaffolding in collagen: Implications on protein dynamics as revealed by solid-state NMR. *Biopolymers*. 2014; 101(3):246-256. https://doi.org/10.1002/bip.22330.

[224] Pálfi VK, Perczel A. Stability of the hydration layer of tropocollagen: A QM study. *Journal of Computational Chemistry*. 2010; 31(4):764-777. https://doi.org/10.1002/jcc.21361.

[225] Yu X, Huang J, Wu C, Zhang W. Biocompatible autonomous self-healing PVA-CS/TA hydrogels based on hydrogen bonding and electrostatic interaction. *Sci Rep*. 2025; **15**, 1893. https://doi.org/10.1038/s41598-025-85298-3.

[226] Przybyłek M, Bełdowski P, Wieland F, Cysewski P, Sionkowska A. Collagen Type II—Chitosan Interactions as Dependent on Hydroxylation and Acetylation Inferred from Molecular Dynamics Simulations. *Molecules*. 2023; 28(1):154. https://doi.org/10.3390/molecules28010154.

[227] Cutini M, Pantaleone S, Ugliengo P. Elucidating the Nature of Interactions in Collagen Triple-Helix Wrapping. *J Phys Chem Lett*. 2019;10(24):7644-7649. https://doi.org/10.1021/acs.jpclett.9b03125.